THE ASTROPHYSICAL JOURNAL SUPPLEMENT SERIES, 90:31–82, 1994 January

YOUNG OPEN CLUSTERS AS PROBES OF THE STAR FORMATION PROCESS. I. AN ATLAS OF OPEN CLUSTER PHOTOMETRY

RANDY L. PHELPS[1,2]
Phillips Laboratory, Optical Environment Division, Backgrounds Branch (GPOB), 29 Randolph Road, Hanscom AFB, MA 01731-3010

AND

KENNETH A. JANES
Department of Astronomy, Boston University, Boston, MA 02215
Received 1993 February 16; accepted 1993 June 30

ABSTRACT

We have obtained CCD photometry, in the *UBV* system, for 23 open clusters in order to explore the star formation history of the Cassiopeia region of the Perseus spiral arm of our Galaxy. Magnitudes and colors of 35,788 stars were measured, making this the most comprehensive, homogeneous single study of open cluster properties in one part of the Galaxy.

This paper presents an atlas of open cluster photometry that serves as the database for an investigation of cluster properties such as their ages, distances, reddenings, sizes, and richnesses. This information provides insight into the spatial and temporal formation sequence of the clusters and allows an investigation of the stellar content of the clusters to be undertaken.

Subject headings: atlases — open clusters and associations: general — stars: evolution — techniques: photometric

1. INTRODUCTION

An important class of objects, the optically revealed or post-embedded open clusters, have generally been neglected in star formation studies. The development of infrared array cameras and millimeter and submillimeter telescopes allows the dusty environments where open clusters form to be explored in detail never before possible, resulting in a concentration of research efforts on the embedded open clusters rather than their more evolved counterparts. The advent of CCDs, however, makes it possible to exploit more fully the information that optically revealed open clusters can provide. The ability to obtain improved photometry of tens of thousands of stars means that large-scale studies of open clusters can now be conducted on unprecedented scales. The precision of CCD photometry is also significantly higher than that obtained by the photographic photometry which has traditionally been used for large-scale cluster studies. With CCD photometry, greatly improved information on cluster distances and ages as well as stellar content can be obtained. Without such information, our knowledge of the star formation process will remain incomplete. How can one understand the star formation process itself without an understanding of its end result?

We have undertaken a CCD photometric study of open clusters in the Cassiopeia region of the sky to explore the star formation history in this part of the Galaxy. In the Cassiopeia region, in the range $105° < l < 140°$, near the Galactic plane, the Lund Catalog of Open Cluster Data (Lyngå 1987) lists no fewer than 80 clusters, most with little known about them. In particular, the Palomar Observatory Sky Survey (POSS) print centered on $\alpha = 01^h35^m22^s$, $\delta = 60°29'08''$ ($l \sim 128\overset{\circ}{.}8$, $b \sim -1\overset{\circ}{.}4$) reveals 12 rich to moderately rich clusters, most of which are quite young, based on previous studies. The two POSS prints proceeding westward show an equally large number of clusters, although they are generally less rich and less well defined. To the east lies the active star formation regions associated with the young open clusters IC 1795 (W3), IC 1805 (W4), and IC 1848 (W5), as well as the famous Double Cluster consisting of h and χ Persei. Many of these clusters have been studied in the past with photographic and/or photoelectric photometry, indicating that the majority of them are relatively young and are a part of the Perseus spiral arm of our Galaxy.

We have obtained CCD *UBV* photometry for 23 of the clusters in the region $116° < l < 131°$ (see Table 1). The clusters in the region were chosen for several reasons. The large number of relatively young clusters suggests that some sort of triggering mechanism may be responsible for cluster formation. With modern CCD photometry of numerous clusters in a relatively small region of space, the sequence of cluster formation can be determined, thus shedding light on the triggering mechanism. Also, the apparent angular sizes of these clusters (Table 1) are ideally suited to the field of view obtainable with small telescopes and CCDs. For instance, the KPNO 0.9 m telescope, operated at f/7.5 with a TEK 512 × 512 CCD gives a field of view of 6′.6. With the addition of photometry for nearby field regions it is possible to construct meaningful statistical luminosity functions for these clusters. An added advantage is that older photometry can be used for the brightest stars, since they saturate quickly in the CCD images, even with the shortest exposures. Additionally, the distribution of CO around several of these clusters has been mapped (Leisawitz, Bash, & Thaddeus 1989; Liu et al. 1988), and a large portion of the region

[1] Visiting Astronomer, Kitt Peak National Observatory, National Optical Astronomy Observatories, which are operated by the Association of Universities for Research in Astronomy, Inc., under contract with the National Science Foundation.
[2] National Research Council Associate.

TABLE 1

OBSERVED CLUSTERS

Name	l	b	α(1950)	δ(1950)	Diameter	Trumpler Class
Be 7	130°13	+0°37	01^h50^m6	62°07′	4′	II 2 p
NGC 663	129.46	−0.94	01 42.6	61 00	14	II 3 r
NGC 659	129.34	−1.51	01 40.8	60 27	5	I 2 m
NGC 654	129.09	−0.35	01 40.6	61 38	5	II 2 r
NGC 637	128.55	+1.70	01 39.4	63 45	3	I 2 m
Tr 1	128.22	−1.14	01 32.3	61 02	3	II 2 p
NGC 581	128.02	−1.76	01 29.9	60 27	5	II 2 m
NGC 457	126.56	−4.35	01 15.9	58 04	20	II 3 r
NGC 436	126.07	−3.91	01 12.5	58 33	5	I 2 m
NGC 433	125.90	−2.60	01 12.1	59 52	4	III 2 p
NGC 381	124.94	−1.22	01 05.2	61 19	6	III 1 m
NGC 366	124.68	−0.59	01 03.3	61 58	4	II 3 m
Be 62	123.99	+1.10	00 57.9	63 41	5	III 2 m
Cz 2	121.97	−2.70	00 40.8	59 53	10	IV 2 m
St 24	121.55	−0.88	00 36.8	61 41	5	III 1 p
NGC 146	120.87	+0.49	00 30.2	63 01	5	II 2 p
King 15	120.75	−0.95	00 30.1	61 35	3	IV 2 p
NGC 129	120.25	−2.54	00 27.1	59 57	12	III 2 m
NGC 103	119.80	−1.38	00 22.5	61 04	5	II 1 m
Be 60	118.85	−1.64	00 15.0	60 41	3	III 1 p
Be 1	117.79	−2.03	00 07.0	60 09	5	III 1 p
Be 58	116.75	−1.29	23 57.6	60 41	5	II 1 m
NGC 7790	116.69	−1.01	23 55.9	60 56	5	II 2 m

has been mapped in H I (Leisawitz & de Geus 1991). This provides additional data for interpreting the formation history of the clusters.

This first paper in the series presents the photometric data for the 23 observed open clusters. In particular, a detailed discussion of the reddenings, distances, and ages of the clusters, along with their uncertainties, is presented. Additional discussions cover the determination of the cluster sizes and the number of cluster members, along with their associated uncertainties.

2. OBSERVATIONS

Data for this program were collected over a 3 year period at Kitt Peak National Observatory. The 1988 and 1989 observations were made with the KPNO No. 1 0.9 m telescope, operating at f/7.5 and using the TEK 1 512 × 512 CCD. The TEK 1 CCD has pixel sizes of 27 μm on a side, resulting in a scale of 0.″77 pixel^{-1} and a field of view of 6.′6. The CCD gain was set at 3.5 e^- ADU^{-1}. The KPNO Harris B and V filters and a standard KPNO $CuSO_4$ + UG2 U filter were used.

The 1990 observations were made with the relocated KPNO 0.9 m telescope, again operating at f/7.5 but with the TEK 1024 × 1024 CCD. This larger format chip, with 24 μm pixels, gives a scale of 0.″68 pixel^{-1} and an 11.′68 field of view. For this run the CCD gain was set at 9.6 e^-/ADU^{-1}. The same set of filters used in the 1988 and 1989 observing runs was used for the fall 1990 observing run.

Because of the relatively young age of the clusters, there typically was at least one bright ($V \sim 8$–9) B-type star in the field of view. Multiple short exposures (20–300 s), with exposure times depending upon the presence of brighter stars and the filter being used, were co-added in order to achieve a total integration time of 10 minutes for the B and V filters, and 15 minutes for the U filter when possible. The autoguider was used during the observations. The tracking of the telescope was good enough (to within ~1″) to permit a straight co-adding of the images without resorting to coordinate transformations. For the V and B filters, where 10 or more individual frames were obtained for each field, co-adding of the images was performed using the average-sigma-clipping algorithm in the IMRED package of IRAF.[3] This algorithm rejects a pixel if its value deviates significantly from the average value for that pixel. A 3 σ threshold for rejection of spurious data points, such as cosmic rays, was used. Generally only a few U frames, with longer integration times, were obtained for each field. For these frames, a straight averaging of the frames was performed.

When possible, the observations were undertaken when the clusters were near the zenith. The maximum air mass, X, at the time of observations was $X = 1.78$, with the vast majority of the observations being undertaken with $X < 1.40$. Landolt (1973, 1983) standard stars and the so-called "Dipper Asterism" stars in M67, observed over the same range in air mass as were the clusters, were observed for calibration of the final photometric data.

3. DATA REDUCTION

Regions of the sky relatively devoid of stars (Schoening 1988) were imaged during twilight to construct flat-field images. Approximately 10 exposures, each a few thousand ADU above bias, were obtained with the telescope position randomly moved several tens of arcseconds between exposures. The images were subsequently co-added using the

[3] IRAF is distributed by the National Optical Astronomy Observatories, which are operated by the Association of Universities for Research in Astronomy, Inc., under contract with the National Science Foundation.

sigma-clipping algorithm in IRAF to remove stellar images from the sky images.

Sky images were used exclusively to construct the U and B flat fields. Dome flats were occasionally used for the V filter, since it was not always possible to obtain enough sky images. Bias subtraction and flat-fielding were performed by standard techniques with the NOAO IRAF package.

Instrumental magnitudes were obtained with the stellar photometry software (SPS) point-spread function (PSF) photometry package (Janes & Heasley 1993). The package is similar to DAOPHOT (Stetson 1987), with the primary differences being the method of finding stars and the solution for overlapping stellar images. The details of the package can be found in Janes & Heasley (1993).

The instrumental magnitudes were transformed into standard UBV colors using a variation of the algorithm discussed by Harris, FitzGerald, & Reed (1981). As they pointed out, one should fit the standard colors and magnitudes to the observed instrumental magnitudes, rather than the other way around as is frequently done. We have, therefore, chosen to transform the photometry with the following relations:

$$v_{i,n} = V + a1 + b1X_{i,n} + c1(B - V)\,, \quad (1)$$

$$b_{j,n} = V + a2 + b2X_{j,n} + c2(B - V) - 0.03X_{j,n}(B - V)\,, \quad (2)$$

$$u_{k,n} = B + a3 + b3X_{k,n} + c3(U - B)\,, \quad (3)$$

where v, b, and u are the instrumental magnitudes for the star in question on frames i, j, and k of night n, respectively; the a's, b's, and c's are the transformation coefficients; X is the air mass for a given frame; and V, $(B - V)$, and $(U - B)$ are the corresponding standard magnitude and color indices of the star. Note that for each night n there may be more than one frame in some colors, so the equations are solved by least squares as two sets of simultaneous equations. The first set of equations consists of the first two of the above equations, which are solved simultaneously for all v and b frames on all nights to get the standard V and $(B - V)$. The second set of equations consists of all of the u frames on all nights, which are also solved by least squares for the standard $(U - B)$. The error estimates consist of the standard errors from the least-squares solutions, which depend entirely on the internal consistency among the frames making up the solution. No separate error estimates are computed for measurements on different nights.

The instrumental magnitudes were tied to the Landolt standard star observations (Landolt 1973, 1983). For the 1988 and 1990 observations, stars in M67 (Schild 1983) were also observed and used as standards. For the M67 stars, corrections to the Schild (1983) data of 0.04 mag have been reported by Joner & Taylor (1990) and Montgomery, Marschall, & Janes (1993). The final values chosen for the M67 stars are those of Montgomery, Marschall, & Janes (1993).

The standard stars were observed at an air mass less than $X \sim 1.8$. Because of the relatively small number of standard stars which were typically observed in the course of the night, and because our observations indicate that the extinction at Kitt Peak was quite stable over the period of our observations, mean extinction coefficients were used for the photometric reductions. The eruption of Mount Pinatubo in 1991 has significantly altered extinction coefficients, but no such events occurred during the period of our observations. The extinction coefficients $b1$, $b2$, and $b3$ are the mean extinction coefficients for Kitt Peak (cf. Pilachowski et al. 1991) and are listed in Table 2.

The standard star observations for each observing run were combined to solve for the mean scale factors ($c1$, $c2$, and $c3$) for the entire run. The zero points ($a1$, $a2$, and $a3$) were determined separately for each night. The derived coefficients for each night of the three observing runs, and the clusters for which those coefficients apply, are listed in Table 2. The residuals of the fit to the standard stars for the various observing runs are shown in Figures 1–3. The transformation to the standard system resulted in typical rms residuals of 0.02 in V, 0.02 in $(B - V)$, and 0.03 in $(U - B)$. The residuals tend to be larger, especially for the U transformations, for the 1989 data. The 1989 run was especially affected by occasional cloud cover during the evenings, making observations of standard stars during photometric conditions difficult. This is likely to be the explanation for the larger than normal residuals.

An estimate of the external error, as a function of magnitude, is illustrated in Figure 4, which shows differences in the magnitudes derived in overlapping frames for the cluster NGC 663. The errors in the V and $(B - V)$ photometry are ~0.02

TABLE 2

TRANSFORMATION COEFFICIENTS

Run	Night	a_1	b_1	c_1	a_2	b_2	c_2	a_3	b_3	c_3	Transformed Clusters
1988	Nov 4/5	3.4212	0.15	0.0525	3.5689	0.27	0.9321	5.3002	0.57	0.9232	NGC 457
	Nov 6/7	3.4301	0.15	0.0525	3.5792	0.27	0.9321	5.3658	0.57	0.9232	NGC 637
1989	Sep 22/23	3.2109	0.15	0.0506	3.3758	0.27	0.9258	5.5687	0.57	0.8530	
	Sep 23/24	3.2705	0.15	0.0506	3.4337	0.27	0.9258	5.6557	0.57	0.8530	
	Sep 24/25	3.2190	0.15	0.0506	3.3707	0.27	0.9258	5.5406	0.57	0.8530	NGC 436, Be 7
	Sep 26/27	3.1993	0.15	0.0506	3.3363	0.27	0.9258	5.5325	0.57	0.8530	NGC 581, Tr 1
	Sep 27/28	3.1804	0.15	0.0506	3.3185	0.27	0.9258	5.4939	0.57	0.8530	NGC 663, NGC 654
	Sep 28/29	3.1743	0.15	0.0506	3.3132	0.27	0.9258	5.4394	0.57	0.8530	NGC 659
1990	Nov 21/22	4.0631	0.15	0.0198	4.2102	0.27	0.9311	5.9796	0.57	0.9744	NGC 103
	Nov 22/23	4.0708	0.15	0.0198	4.2105	0.27	0.9311	5.9947	0.57	0.9744	NGC 381, NGC 433, NGC 366, Be 62
	Nov 23/24	4.0406	0.15	0.0198	4.1742	0.27	0.9311	6.1229	0.57	0.9744	Cz 2, St 24, King 15
	Nov 26/27	4.0973	0.15	0.0198	4.2682	0.27	0.9311	6.1243	0.57	0.9744	Be 60, Be 58, Be 1, NGC 146

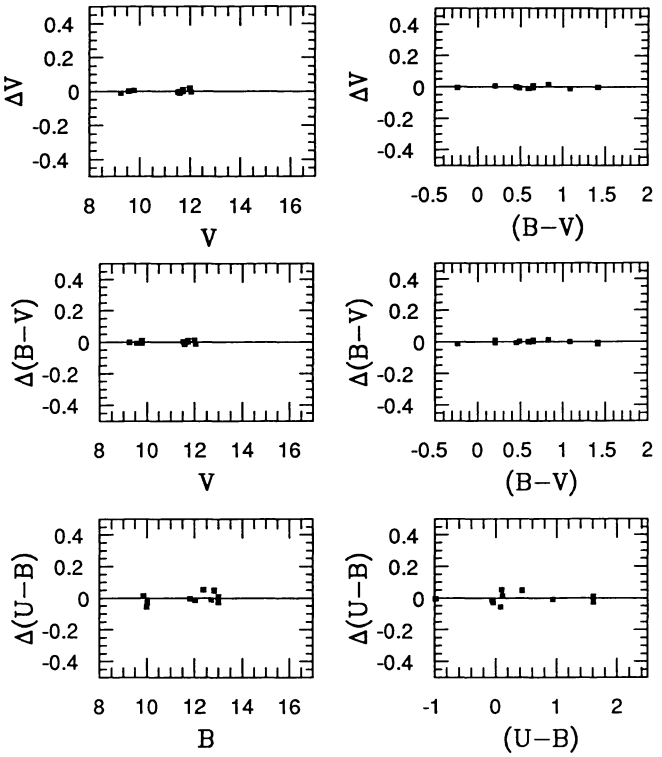

FIG. 1.—Residuals of the fit to the standard stars for the 1988 observing run.

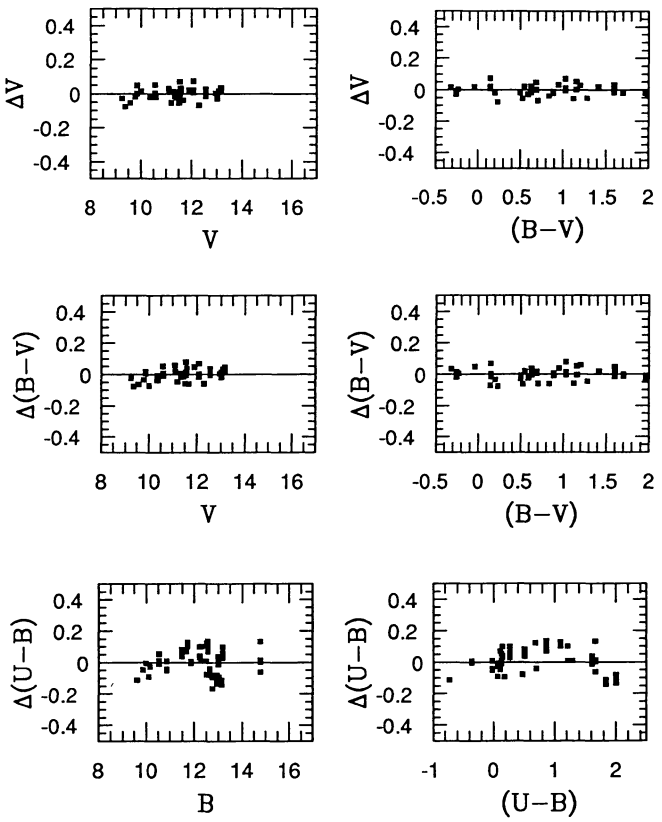

FIG. 2.—Residuals of the fit to the standard stars for the 1989 observing run.

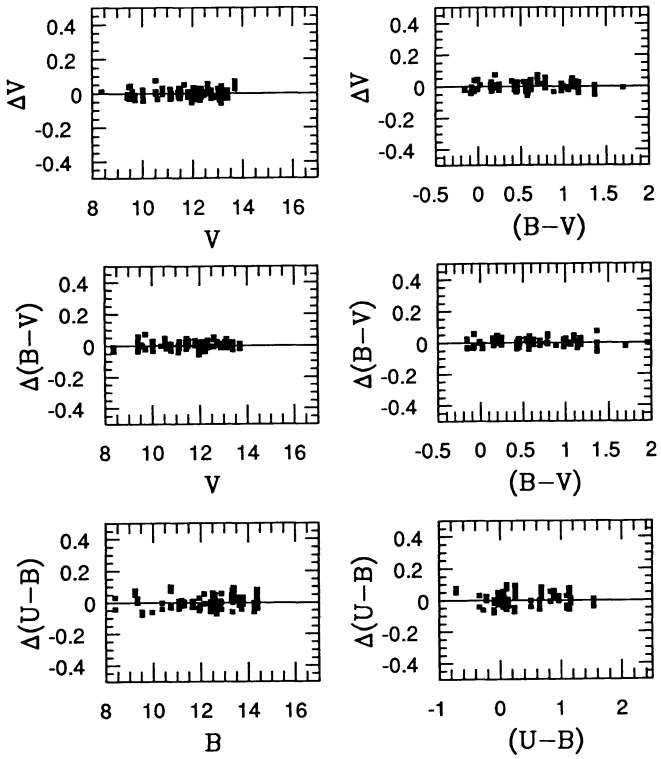

FIG. 3.—Residuals of the fit to the standard stars for the 1990 observing run.

and ~0.03, respectively, to a V-magnitude of ~18. The errors in $(U-B)$ are ~0.03 to a V-magnitude of ~17, after which they increase substantially to the limiting magnitude of $V \sim$ 18.5–19.0. The two-color diagrams for $V > 16$, corresponding to $U > 17$, begin to deviate from the standard sequence because the stars are near the limiting magnitude of the photometry, and interpretations of the two-color diagrams for the later type stars should be made with caution. The deviations of the later type stars from the standard sequence do not severely affect the reddening estimates, since the reddening is determined from the early-type stars.

Several of the clusters were observed on multiple nights to cover larger areas of the cluster than a single CCD frame would allow. Some of these frames, as well as several entire clusters, were observed on nonphotometric nights and calibrated using short-exposure frames taken on other, photometric nights, or by the overlap in the mosaicked cluster frames which were obtained on other, photometric nights. Generally "nonphotometric" refers to nights which were clear for part of the time but on which occasional cloud cover prevented the observation of a sufficient number of standard stars. During observations of two clusters, NGC 129 and NGC 7790, there was a thin layer of cirrus clouds during the observations; calibration was obtained through previous *UBV* photometric studies of them.

4. ANALYSIS

4.1. *Ratio of Total to Selective Absorption*

Johnson (1965) performed an extinction curve analysis of the Double Cluster, h and χ Persei, located in the vicinity of

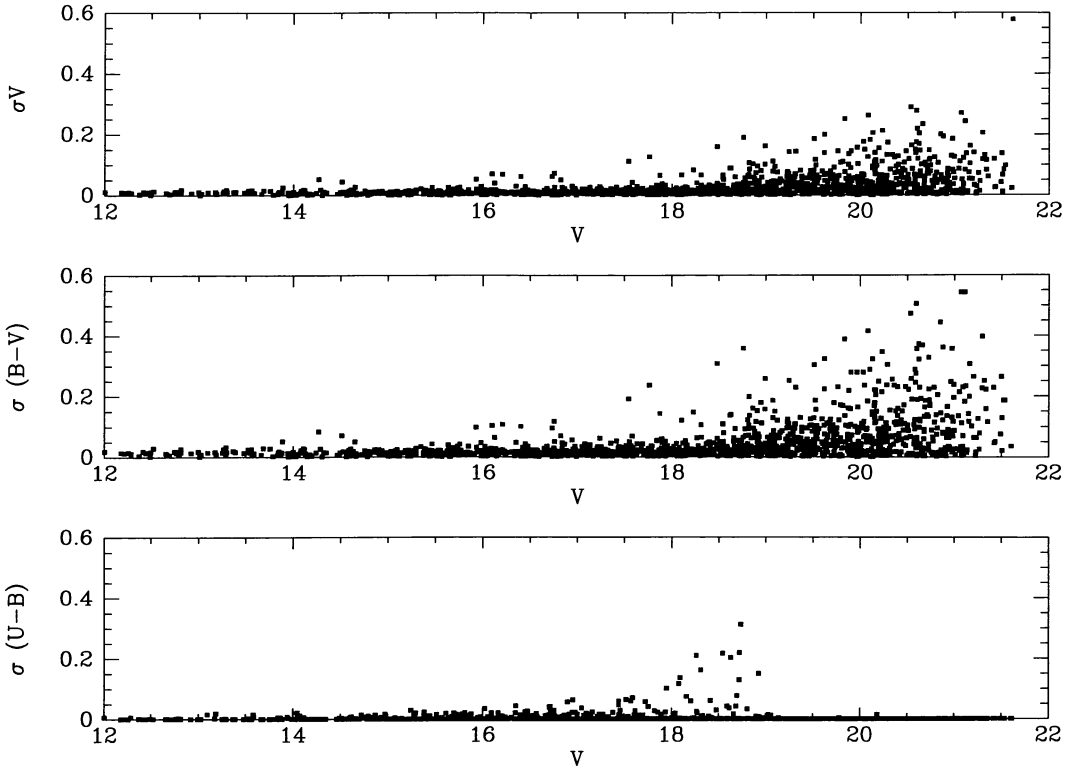

FIG. 4.—Typical errors in the photometry as a function of V-magnitude. Errors are for stars with measured magnitudes within overlapping CCD images of the cluster NGC 663. The values of $\sigma(U-B) = 0.0$ for $V > 18$ are an artifact of the transformation routine; the U photometry reaches only to $V \sim 18$–18.5.

our program clusters, and determined a ratio of total to selective absorption, R_v, of 3.0. His analysis in another region in Perseus also gives a value of $R_v = 3.0$, although inspection of his extinction curve suggests that $R_v = 3.1$–3.2 is more appropriate. The cluster method for determining R_v (Mihalas & Binney 1981, p. 191) was used for several of our program clusters (NGC 581, NGC 663, and NGC 654) with $R_v = 3.1$, 3.1, and 3.2, respectively, although the dispersion in these values is quite large (± 0.4) due to the small range in reddening toward these clusters. A value of $R_v = 3.1$ was therefore chosen for all of the clusters, with an assumed uncertainty of $\sigma_{R_v} = 0.1$.

4.2. *Interstellar Reddening*

To determine the reddening to the clusters, stars along the Schmidt-Kaler (1982, hereafter SK82) main-sequence two-color curve (MSTCC) were shifted in the two-color diagram along an appropriate reddening line until a match between the MSTCC and the stellar distribution was found. The coefficients of the reddening line, as a function of the intrinsic color of a star, were extensively tabulated by Crawford & Mandwewala (1976) and are the coefficients used in this study. This standard method was used for most of the clusters in this study. Several clusters, however, showed evidence of variable reddening in the color-magnitude diagram (CMD) and/or two-color diagrams, and an individual dereddening analysis was performed for them. Details of the individual dereddening analysis can be found in Phelps (1992).

Stars were chosen for the reddening analysis only if their position in the two-color diagram indicated that they were spectral type A or earlier, regardless of whether the individual dereddening or standard technique was used. This choice was dictated by several factors:

1. *Metallicity.*—The effect of metallicity on the colors of the later type stars is large, with lower metallicity resulting in substantial UV excesses (Cameron 1985a, b, c). The use of stars with spectral type A0 and earlier minimizes the uncertainty in $E(B-V)$ as a result of unknown metallicities.

2. *Binaries.*—Unresolved binary stars have colors which may be different from those of single stars (Golay 1974). In the two-color diagram, increasing the mass ratio of an early-type binary star moves the system nearly parallel to the two-color line, but moves A–F systems nearly perpendicular, toward lower $(U-B)$ (Golay 1974, p. 92). The use of earlier type stars minimizes reddening errors resulting from the presence of unresolved binary stars.

3. *Rotation.*—The $(B-V)$ index is primarily an indicator of temperature, while the $(U-B)$ index includes temperature and luminosity effects. Rotation reduces the effective temperature and luminosity of a star (Sweet & Roy 1953) and thus will also change its color. Maeder & Peytremann (1970) modeled the effects of rotation and orientation on the observed colors of stars and found that changes in $(U-B)$ can be as great as 0.14 mag. For higher mass stars ($5\ M_\odot$) this maximum color change occurs for an inclination of 0°, resulting in an increase in $(U-B)$ with little contribution to $(B-V)$. As the inclination approaches 90°, their models show that the effect of rotation is

along the reddening line, so that rotation effects do not significantly affect the reddening determination for an early-type star.

4. *Pre-main-sequence (PMS) stars.*—In clusters with ages such as those we are studying (mostly in the 1–30 Myr range), the higher mass stars will have already reached the main sequence or evolved away from it, while the lower mass stars, with evolutionary timescales longer than this, will not have reached the main sequence and will be PMS objects (Stahler 1983). Lower mass, classical T Tauri stars (CTTSs) have been found to have significant UV excesses (Bertout 1988; Bertout & Basri 1991), which are thought to arise in the transition region between the protostellar disk and the stellar surface. Reddening determinations for the higher mass main-sequence stars are more reliable, since they are not PMS objects, although many B-type stars in these clusters may be Be stars, with circumstellar material that affects the reddening of the star. When Be stars are present (e.g., in NGC 663), a great deal of scatter is seen in the CMD and two-color diagram, and it is possible to deal with these stars by an individual dereddening analysis when appropriate.

5. *Errors in photometry.*—As discussed in § 3, the errors in the U photometry become large for $V > 16$ ($U > 17$), which, for typical clusters in this survey, corresponds to observed main-sequence colors of ~ 1. For most of the observed clusters this corresponds to A-type stars.

An estimate of the uncertainty in the value of the $E(B-V)$ is difficult, and errors quoted in the literature are rarely if ever the result of a quantitative analysis. Since variations in individual clusters are difficult to quantify, the following analysis is intended to establish a typical uncertainty in reddening estimates rather than uncertainties for individual cases.

Systematic errors in reddening determinations arise from uncertainties in the intrinsic colors of the stars which make up the MSTCC itself, and uncertainties in the slope of the reddening vector ($\sigma_{\rm vector}$) along which a star moves in the two-color diagram as reddening increases. The uncertainties $\sigma_{(B-V)_0}$ and $\sigma_{(U-B)_0}$ are the uncertainties associated with the MSTCC and are taken to be Gaussian-distributed. The systematic uncertainty is taken to be of the form

$$\sigma^2_{E(B-V)_{\rm sys}} \sim \sigma^2_{(U-B)_0} + \sigma^2_{(B-V)_0} + \sigma^2_{\rm vector}\,, \qquad (4)$$

where $\sigma_{\rm vector}$ is the uncertainty in the reddening line. SK82 has estimated that $\sigma_{(B-V)_0} \sim 0.04$ and $\sigma_{(U-B)_0} \sim 0.03$ on the upper main sequence, where these values represent intrinsic scatter about the mean colors at a given spectral type. For stars with spectral type O V to B8 (the spectral range used to determine the reddening), the Crawford & Mandwewala (1976) reddening vector slope is 0.69 ± 0.01, neglecting the higher order terms in the reddening vector. Using $\sigma_{\rm vector} \sim 0.01$, and the values of $\sigma_{(B-V)_0}$ and $\sigma_{(U-B)_0}$ as above reduces equation (4) to $\sigma_{E(B-V)_{\rm sys}} \sim 0.05$.

The random uncertainty is assumed to be of the form

$$\sigma^2_{E(B-V)_{\rm ran}} \sim \sigma^2_{(U-B)} + \sigma^2_{(B-V)} + \sigma^2_{\rm fit}\,, \qquad (5)$$

where $\sigma_{(B-V)}$ and $\sigma_{(U-B)}$ are associated with the photometry, and $\sigma_{\rm fit}$ is associated with the visual fit of the MSTCC to the two-color diagram.

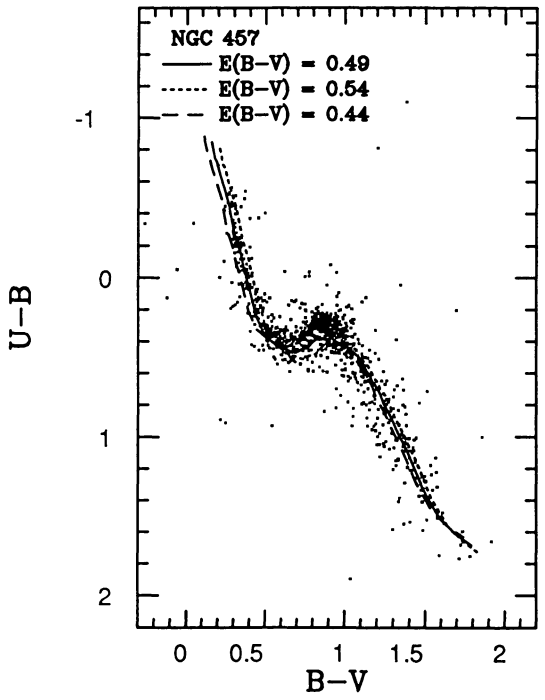

FIG. 5.—Comparison of the fit of the Schmidt-Kaler (1982) main-sequence two-color curve, reddened by $E(B-V) = 0.44$, 0.49, and 0.54, to the observed two-color diagram of NGC 457.

Typical formal uncertainties in transforming the instrumental magnitudes to the standard system are 0.02–0.03 mag in $(U-B)$ and 0.01–0.02 mag in $(B-V)$. Based upon experience in fitting the SK82 main-sequence two-color line to the observed two-color diagrams of our clusters, and the constraints on the reddening determination imposed by the fit in the CMD of the SK82 ZAMS to the bend in the main sequence of clusters (see below), the uncertainties in the reddening determinations are estimated to be typically ± 0.03 mag (see Fig. 5). This results in a random uncertainty of $\sigma_{E(B-V)_{\rm ran}} \sim 0.05$.

The typical total uncertainty in the reddenings is likely to be $\sigma_{E(B-V)} \sim 0.07$, including random and systematic effects, a more conservative estimate than is usually expressed in such studies (e.g., Tapia et al. 1984), where the random uncertainty is frequently quoted instead of total uncertainty.

4.3. *Distances*

We have elected to estimate the apparent distance moduli of the clusters by the traditional method of shifting a fiducial zero-age main sequence (ZAMS) to match the observed stellar distribution in the V–$(B-V)$ CMD, once the reddening has been fixed. The ZAMS of SK82, based on an assumed distance modulus to the Hyades of $(m-M)_0 = 3.28$, is used in this study.

The fainter photometry of this program, compared with most previous studies of these clusters, reaches the bend in the main sequence at $M_v \sim 2$ and allows a match of the ZAMS to the stellar distribution in the CMD to be more tightly constrained than is possible when only the upper, more vertical, and often evolved portion of the main sequence is fitted. The

degree of the problem is illustrated for NGC 436 (Fig. 6), where ZAMS fits for $(m - M)_0 = 12.55$ (3200 pc) and $(m - M)_0 = 11.67$ (2150 pc) are shown. The former distance modulus is that determined for the cluster in § 5.9, while the latter is that determined by Becker (1971) using the data of Becker & Stock (1958).

In this study, the ZAMS has been fitted to the lower envelope of the main sequence, in the region where the bend occurs in the main sequence. This choice was dictated by several factors:

1. *Binary stars.*—It is well known that the effect of binary stars in the CMD results in a spread of the main sequence toward brighter magnitudes (cf. Golay 1974, p. 91). A fit to the mean location of the main sequence tends to underestimate the distance of the cluster, since the ZAMS is fitted toward brighter magnitudes.

2. *Rotation.*—Maeder & Peytremann (1970) have shown that rotation and axial inclinations of stars have the effect of spreading the main sequence toward brighter magnitudes and redder colors. Since most stars on the upper main sequence are rapidly rotating, this could significantly affect the observed width of the main sequence.

3. *Evolutionary effects.*—In the clusters under study, with typical ages of 1–30 Myr, the low-mass stars will be PMS objects and will be located in the region of the CMD where severe contamination by field stars is present, while the higher mass stars will have evolved off the main sequence. The stars with $M_v \sim 2$ have main-sequence lifetimes of more than 1 Gyr (Maeder & Meynet 1991, hereafter MM91) and PMS timescales of ~3 Myr (Stahler 1983), so that stars with $M_v \sim 2$ will likely be main-sequence stars.

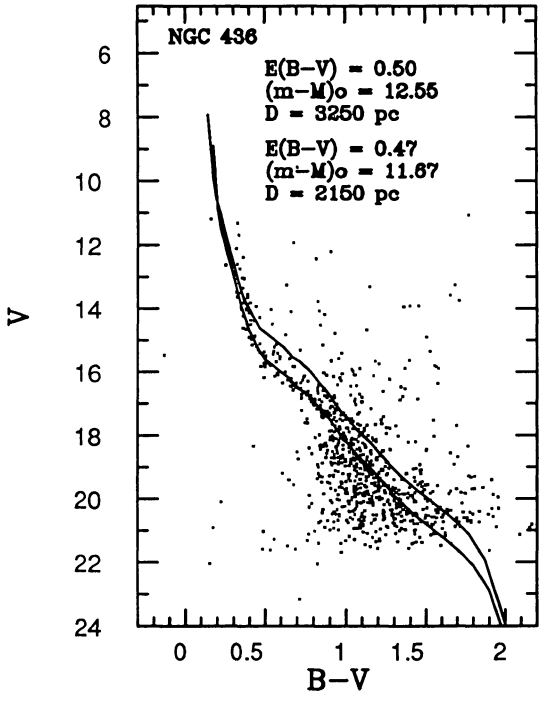

FIG. 6.—ZAMS fits to NGC 436 using $(m - M)_0$ and $E(B - V)$ values from this study (*lower curve*) and from Becker (1971) (*upper curve*).

All three of these effects would tend to produce an underestimate of the distance modulus. However, by fitting to the lower envelope of the main sequence, the existence of observational errors could lead to an overestimate of the distance modulus. Fortunately, since the random photometric errors in the present study are of the order of a few hundredths of a magnitude, this is not a serious issue.

The standard visual match of the ZAMS to the cluster sequences as described here does not easily lend itself to a quantitative determination of the uncertainty in the derived distances. A simple expression for the uncertainty in the distance modulus was given by Clariá & Rosenzweig (1978), but is more appropriate to evaluating the errors in the determination of the distance modulus of a single star rather than an entire cluster. The problem of fitting a fiducial ZAMS to an observed CMD is a subtle pattern-matching process, involving a comparison of a solid curve to a pattern of dots. While the human brain is remarkably good at this, it remains an inherently nonquantitative process.

Nevertheless, it is possible to quantify many aspects of the problem. The determination of the true distance modulus, $(m - M)_0$, requires a knowledge of the terms in the familiar equation

$$(m - M)_0 = (m - M)_v - R_v E(B - V)\,, \qquad (6)$$

The uncertainty in the true distance modulus, $\sigma^2_{(m-M)_0}$, is composed of uncertainties in the apparent distance modulus, $\sigma^2_{(m-M)_v}$, as well as uncertainties associated with the second term in equation (6), which can be written as $R_v^2\sigma^2_{E(B-V)} + \sigma^2_{R_v}E^2(B - V)$.

The uncertainty in the apparent distance modulus, $\sigma^2_{(m-M)_v}$, is itself made up of uncertainties in the fit to the luminosity width of the main sequence, σ_v^2, the ZAMS used in the fitting, σ^2_{ZAMS}, and the uncertainty in the fit due to reddening, which is given by the reddening times some typical slope (S) in the region used in the fitting, $S^2\sigma^2_{E(B-V)}$.

The uncertainty in the reddening, $R_v^2\sigma^2_{E(B-V)}$, and the uncertainty in the fitting of the ZAMS, $S^2\sigma^2_{E(B-V)}$, are correlated, however. If the reddening is overestimated, the fit of the ZAMS is forced to fainter magnitudes, thus compensating, to some degree, for the overestimation of the reddening. Similarly, if the reddening is underestimated, the fit of the ZAMS is forced to brighter magnitudes, again compensating for the error in the reddening determination. The total contribution of the uncertainty in the reddening to the true distance modulus is, therefore, of the form $(S - R_v)^2\sigma^2_{E(B-V)}$, assuming the effects of S and R_v to be equal.

The term $\sigma^2_{E(B-V)}$ itself is made up of a random error due to the observations, $\sigma^2_{E(B-V)_{\text{obs}}}$, and a systematic error due to uncertainties in the two-color line itself, $\sigma^2_{E(B-V)_{\text{MSTCC}}}$. The terms σ^2_{ZAMS} and $\sigma^2_{R_v}E^2(B - V)$ are also systematic errors which affect the calibration of the data, while the term σ_v^2 is a random error.

The systematic uncertainty in the true distance modulus can thus be written as

$$\sigma^2_{(m-M)_{0_{\text{sys}}}} = \sigma^2_{\text{ZAMS}} + \sigma^2_{R_v}E^2(B - V) + (S - R_v)^2\sigma^2_{E(B-V)_{\text{MSTCC}}}\,, \qquad (7)$$

while the random uncertainty in the true distance modulus can be written as

$$\sigma^2_{(m-M)_{0_{\rm ran}}} = \sigma^2_v + (S - R_v)^2 \sigma^2_{E(B-V)_{\rm obs}} . \quad (8)$$

As discussed in § 3, the transformation of our instrumental magnitudes to the Landolt standard system results in typical rms residuals of 0.02 mag in V. The uncertainty σ^2_v, however, is the uncertainty due to the luminosity width of the main sequence in the cluster, of which the errors in the photometry are but one part. Other uncertainties include the effects of binary stars, stellar rotation, and effects of stellar evolution and are discussed above. Fitting the ZAMS to the lower portion of the main sequence reduces these errors but does not eliminate them. The intrinsic luminosity width of the main sequence of a typical cluster, such as NGC 457, is ~0.1 mag. The uncertainty σ^2_v in the fit of the ZAMS in luminosity is much better than this but can be no better than 0.02 mag, which is the photometric error. We therefore assume that σ_v is 0.05 mag. In § 4.2, $\sigma_{E(B-V)_{\rm obs}}$ was estimated to be 0.05 mag. In the region of the bend in the main sequence at $M_v \sim 2$, the slope of the main sequence, S, with the chosen 5-to-1 scaling of the $(B-V)$-axis relative to the V-axis, is ~4.7 over $12.5 < V < 14$. Using $R_v = 3.1$ reduces equation (8) to

$$\sigma^2_{(m-M)_{0_{\rm ran}}} = 0.007 , \quad (9)$$

or $\sigma_{(m-M)_{0_{\rm ran}}} = 0.08$.

As discussed in § 4.1, our estimate for $\sigma^2_{R_v}$ is 0.1. The uncertainties $\sigma^2_{\rm ZAMS}$, and $\sigma^2_{E(B-V)_{\rm MSTCC}}$ are calibration errors associated with the SK82 ZAMS and MSTCC. SK82 estimates that σ_{M_v}, on the main sequence, is ~0.3 mag, while $\sigma_{(B-V)}$ is ~0.04 and $\sigma_{(U-B)}$ on the upper main sequence is ~0.03, where these values are typical intrinsic scatter in stars of a given spectral type. For the ZAMS the uncertainty is dominated by σ_{M_v}. We therefore assume $\sigma_{\rm ZAMS} = \sigma_{M_v} = 0.3$ mag, with $\sigma_{E(B-V)_{\rm MSTCC}} \sim 0.05$ mag (see § 4.2). Equation (7) therefore reduces to

$$\sigma^2_{(m-M)_{0_{\rm sys}}} = 0.10 + 0.01 E^2(B-V) , \quad (10)$$

Using a value of $E(B-V) = 0.60$, which is typical of clusters in this study, a total uncertainty of $\sigma_{(m-M)_0} \sim 0.32$ results. This large zero-point uncertainty in the distance modulus of a cluster is dominated by the intrinsic uncertainty in the ZAMS and the MSTCC. The uncertainty in the zero point of the cluster distance scale is, therefore, quite large. The uncertainty in the relative distances, however, is much less if the same ZAMS and MSTCC are used for all clusters in the sample. In this case the systematic error reduces to

$$\sigma^2_{(m-M)_{0_{\rm sys}}} = 0.01 E^2(B-V) , \quad (11)$$

where the remaining term is the uncertainty due to variations in R_v from cluster to cluster. Again using a typical value of $E(B-V) = 0.60$, the total relative uncertainty becomes $\sigma_{(m-M)_0} \sim 0.10$.

The uncertainty in the distance, σ_D, is directly related to the uncertainty in the distance modulus by

$$\sigma^2_D = \sigma^2_{(m-M)_0} \left(\frac{\partial D}{\partial (m-M)_0} \right)^2 \quad (12)$$

(see Bevington 1969). Using

$$D = 10^{[(m-M)_0+5]/5} \quad (13)$$

reduces equation (12) to

$$\sigma^2_D = 0.213 D^2 \sigma^2_{(m-M)_0} , \quad (14)$$

where D is in parsecs.

Using a typical distance of 2700 pc and $\sigma_{(m-M)_0} \sim 0.32$ results in $\sigma_D \sim 400$ pc. The uncertainty in the relative distances, however, is much less. Again using a typical distance of 2700 pc, but an uncertainty in the relative distance modulus of $\sigma_{(m-M)_0} \sim 0.10$, results in $\sigma_D \sim 125$ pc.

4.4. *Cluster Ages*

Cluster ages were obtained with the convective overshooting and mass-loss models of Maeder & Meynet (1988, 1989, 1991) and Maeder (1990). The program to compute isochrones from the evolutionary models was kindly provided by A. Maeder and G. Meynet. Details of the conversion between evolutionary models and isochrones are given in MM91.

The models are for Population I stars with $(X, Y, Z) = (0.70, 0.28, 0.02)$ and masses between 120 and 0.85 $M_\odot$. The Los Alamos opacities (Huebner et al. 1977) were used. For stars with $M > 1.0\ M_\odot$, the distance of overshooting from the convective core is given by $d_{\rm over} = 0.25 H_p$, where H_p is the pressure scale height at the edge of the classically defined core. Empirical mass-loss rates as parameterized by de Jager, Nieuwenhuijzen, & van der Hucht (1988) were used. Details of the transformation from $\log T_{\rm eff}$ to $(B-V)$ and from $L/L_\odot$ to M_v can be found in MM91.

For stars with masses less than 1.2–1.6 $M_\odot$ there is no evidence for convective overshooting, so it is not used in the models. The shapes of the isochrones are uncertain in this region, which is precisely the region that is used to determine the distances of the clusters. For this reason the reddenings and distances have been determined, as described in §§ 4.2 and 4.3, with the SK82 ZAMS and MSTCC, while the ages have been determined with the MM91 isochrones, with the reddenings and distances fixed.

Variable reddening in clusters results in scatter in the CMD, making isochrone fits difficult. Clusters with tight main sequences, indicating that variable reddening is not important, may also have high-mass stars that cannot be fitted by a single isochrone, suggesting that star formation occurred over an interval of time corresponding to the difference in ages between the isochrones needed to fit the stars. Several clusters in this survey, with no evidence of variable reddening, require isochrones separated in age by ~10 Myr in order to fit the evolved stars.

A typical example of an isochrone fit is shown in Figure 7. The isochrones are those for 37, 42, and 47 Myr. The accuracy of the age determination depends critically on the presence of evolved stars in the cluster. The fit near the turnoff is satisfactory for all isochrones, but it is only the fit to the single star with $V = 9.6$ and $(B-V) = 0.7$ that results in the adopted age of 42 Myr.

The fit of the isochrones often is constrained by the brighter blue stars (blue supergiants). As pointed out by the referee,

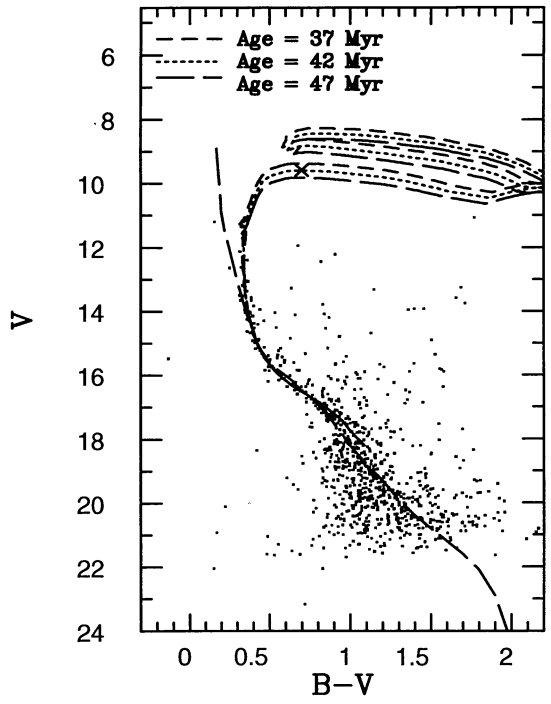

FIG. 7.—Comparison of the fit of several Maeder & Meynet (1991) isochrones to the CMD of NGC 436.

these stars spend most of their time on the blue end of the blue loop in their evolutionary track. The length of the loop depends on the chemical composition (here assumed to be solar) and mass loss. In many cases, an older isochrone will give the right magnitude for the blue supergiants, even if the models do not correctly predict the color, meaning that the inference of a younger age may not be required.

A minimum uncertainty in the age is estimated to be 5 Myr. Clusters that have luminous evolved stars can be fitted with a more limited range in ages and thus have lower uncertainties than clusters without evolved stars. This discussion of the uncertainties in the ages, however, ignores the controversy over the need for convective overshooting and the degree of mass loss in determining stellar ages (cf., Chiosi, Bartelli, & Bressan 1992) as well as the fact that the observed clusters may not be of solar metallicity, as is assumed with the isochrone fits.

4.5. *Cluster Radii*

In order to determine the radius of a cluster, its center must first be found. Since there are few young blue stars in the field, but many in young clusters, luminous blue stars were used to define the cluster center by constructing marginal distributions in x and y (pixels), at 30 pixel intervals (23″ for clusters observed with the 512 × 512 CCD, and 20″ for clusters observed with the 1024 × 1024 CCD). The cluster centers, therefore, are defined by the higher mass end of the main sequences. The marginal distribution for NGC 436 is shown in Figure 8 as an example. A Gaussian fit to each of the distributions was used to obtain an estimate of the x and y center, in pixels, of the cluster.

Cumulative distributions were then used to determine the radii of the clusters. A cumulative distribution is shown in Figure 9*a* for a field region where no cluster is present. The distribution of stars is well represented by a straight line, indicating that no localized enhancement of stars, representing a cluster, is present. The background line is determined by a least-squares fit to the data.

Figure 9*b* shows the cumulative distribution for NGC 436. The straight line represents the stellar background and is determined from a least-squares fit to the region, which appears, from a visual inspection, to be a straight line. Because of incomplete coverage of some clusters in the CCD images, the cluster "edge" may not have been reached and the derived slope of the line is therefore a maximum value.

The outer cluster radius, $R_{\rm full}$, is found by subtracting the background line from the cumulative distribution, and is taken to be the radius at which the net number of stars first reaches zero, moving outward from the cluster center. An example of the resulting distribution for NGC 436 is shown in Figure 10. A half-width at half-maximum radius, $R_{\rm HWHM}$, is also calculated for each of the clusters and is found from the same distribution as is $R_{\rm full}$. The radii of the clusters are lower limits, since the stellar background is often poorly defined.

4.6. *Number of Stars*

The cumulative distribution plots, with the background level subtracted, can also be used to estimate the minimum

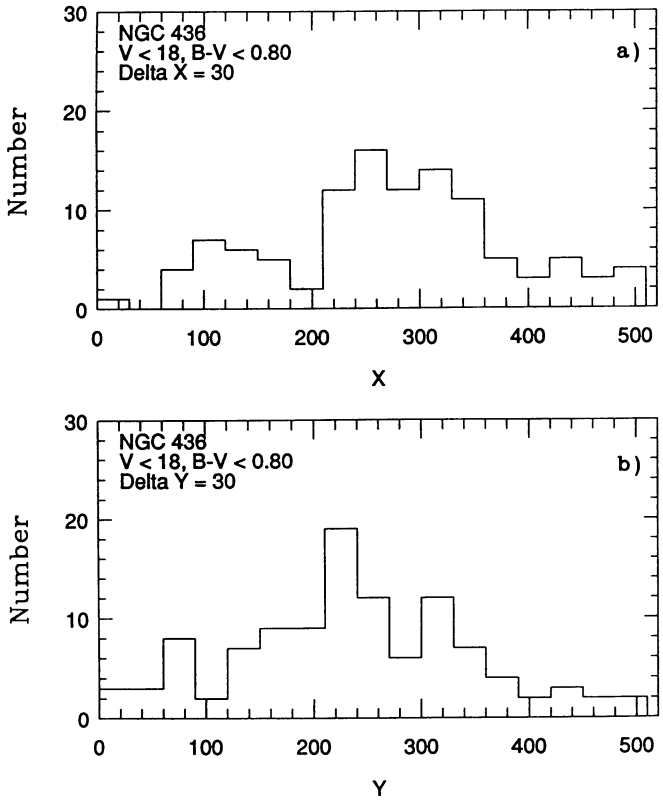

FIG. 8.—(*a*) Marginal distribution, at 30 pixel intervals, in the x-direction of the CCD image, for the cluster NGC 436. (*b*) Same as (*a*), but in the y-direction.

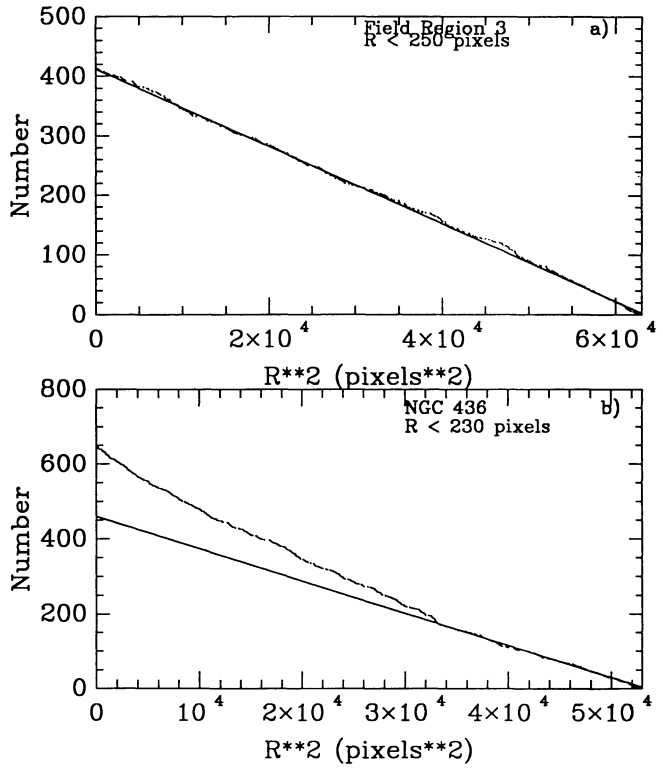

FIG. 9.—(*a*) Cumulative distribution for a field region. (*b*) Cumulative distribution for the cluster NGC 436. See text for details.

number of stars in clusters, to the limiting magnitude of the photometry. The net number of stars is simply the number of stars at zero radius in figures such as Figure 10. This represents a lower limit because of incompleteness of the photometry at fainter magnitudes, as well as uncertainties in the derived slope of the background.

5. RESULTS

This section presents an atlas of photometric data for the 23 clusters which were surveyed in Cassiopeia. The CMDs which appear in the following pages include 35,788 stars, representing the most comprehensive single study of open clusters in a specific region of the sky ever undertaken. The majority of these clusters are located in the Perseus spiral arm, although several clusters have distances which place them outside the arm.

Because of the large number of stars observed during the survey, it is impractical to publish tables of the photometry. It is anticipated that the photometry will become available through a suitable electronic database in the near future.

For some clusters, photometry from other studies has been added, since the brightest stars were often saturated on the CCD images. Some stars were included in the CMDs even though they were outside the observed field, such as in NGC 457, where the presence of the 5th magnitude cluster member ϕ Cas required that a portion of the cluster field be avoided. The star ϕ Cas was included in the CMD but is not represented in the photometric maps.

In most of the CMDs, a characteristic wedge-shaped grouping of stars can be seen. This distribution is a result of foreground and background field stars, which are not associated with the cluster. CMDs for two isolated field regions, located away from any cluster, are shown in Figure 11 and clearly show the wedge-shaped distribution. As the distance from the Sun increases, a given cone of space will contain stars with similar distance moduli, which results in a "cluster-like" CMD, with a characteristic age of ~8–10 Gyr, for that annulus. This age corresponds to the age of the Galactic disk (Janes & Phelps 1994). More distant annuli, with similar distributions of stars, will result in the smearing toward fainter magnitudes of this sequence of stars. The net result in the CMD is a distribution of dwarf stars with a sharp left edge, and a sloping redward edge, along with a nearly vertical distribution of giants.

The derived quantities from the analysis of each cluster are given in Tables 3 and 4. Table 5 contains a summary of previous studies for the clusters when available. For $E(B-V)$ the numbers in parentheses indicate values of $E(B-V)$ converted from the authors' values of $E(G-R)$, using equation (15). Table 6 contains a comparison of our photometry with that of previous studies, when available, with the Δ's indicating the difference between the two studies in the sense of our photometry minus that of the previous studies, with a dispersion in the mean of σ, and having $N_{\rm stars}$ available for comparison.

5.1. *Berkeley 7*

To our knowledge, no previous photometric studies of Berkeley 7 (Be 7) exist. A map of the observed cluster field is shown in Figure 12, while the CMD and two-color diagram (TCD) are shown in Figures 13*a* and 13*b*, respectively. The brighter portion of the main sequence is well defined and distinct from the field star distribution, and no obvious binary sequence is detected. Using the standard reddening analysis, the reddening toward the cluster is found to be $E(B-V) = 0.80$ (Fig. 14*b*), and the observed distance modulus is $(m-M)_v = 14.53$ (Fig. 14*a*), corresponding to a true distance modulus of $(m-M)_0 = 12.05$, or a distance of 2570 pc. The fit of

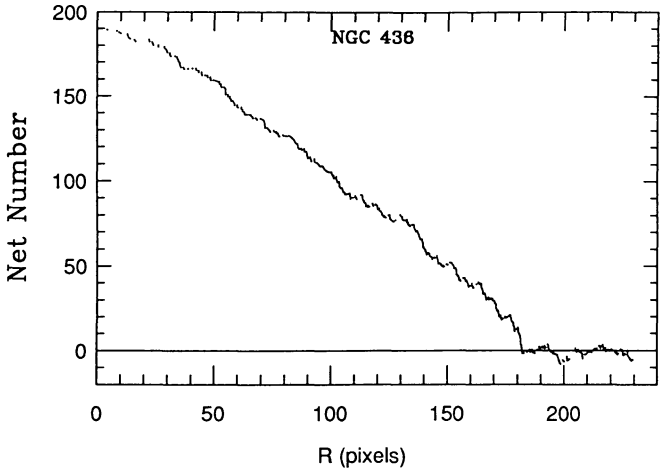

FIG. 10.—Cumulative distribution for NGC 436, with the apparent background line of Fig. 9*b* subtracted.

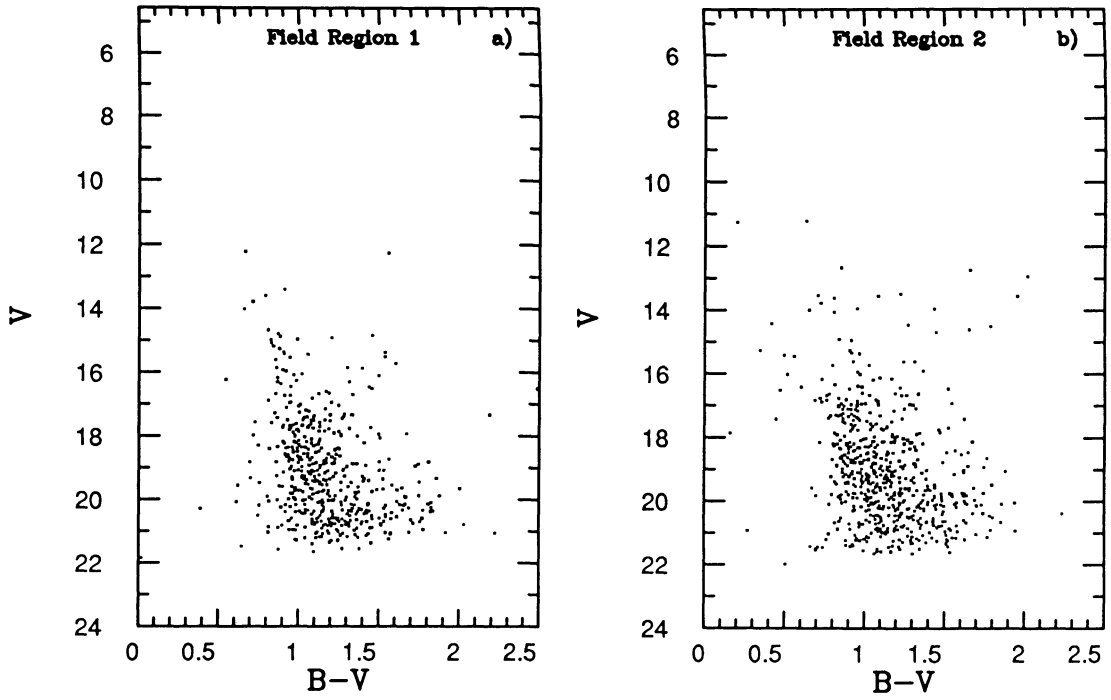

FIG. 11.—CMDs for two isolated field regions

the SK82 ZAMS in the CMD (Fig. 14*a*) shows that the stars in Be 7 show no significant evolution off the main sequence, although the exact age cannot be determined because of the lack of higher mass stars. A 4 Myr isochrone is also shown in Figure 14*a* for comparison, indicating that Be 7 is ~4 Myr old.

5.2. *NGC 663*

NGC 663 has been the subject of numerous studies. In addition to its location in the region under investigation, NGC 663 is of interest because it contains the largest number of Be stars

TABLE 3

OPEN CLUSTERS: DERIVED SPATIAL PROPERTIES

Cluster Number (1)	Name (2)	l (3)	b (4)	$E(B-V)$ (5)	$(m-M)_0$ (6)	D_{pc} (7)	X_{pc} (8)	Y_{pc} (9)	Z_{pc} (10)	Age (Myr) (11)
1	Be 7	130°.13	+0°.37	0.80	12.05	2570	1965	1656	17	0–4
2	NGC 663	129.46	−0.94	0.80	12.25	2818	2176	1791	−46	12–25
3	NGC 659	129.34	−1.51	0.63	12.70	3467	2681	2198	−91	22
4	NGC 654	129.09	−0.35	0.90	12.15	2692	2089	1697	−16	8–25
5	NGC 637	128.55	+1.70	0.65	12.30	2884	2255	1797	86	0–4
6	Tr 1	128.22	−1.14	0.61	12.10	2630	2066	1627	−52	27
7	NGC 581	128.02	−1.76	0.44	12.15	2692	2121	1658	−83	10–22
8	NGC 457	126.56	−4.35	0.49	12.40	3020	2426	1799	−229	7–19
9	NGC 436	126.07	−3.91	0.50	12.55	3236	2616	1905	−221	42
10	NGC 433	125.90	−2.60	0.86	11.83	2323	1882	1362	−105	79
11	NGC 381	124.94	−1.22	0.36	10.13	1062	871	608	−23	1100
12	NGC 366	124.68	−0.59	1.37	12.50	3163	2601	1800	−33	6
13	Be 62	123.99	+1.10	0.82	12.16	2704	2242	1512	52	10
14	Cz 2	121.97	−2.70	...	...	...	...	...	...	...
15	St 24	121.55	−0.88	0.50	12.25	2818	2401	1474	−43	120
16	NGC 146	120.87	+0.49	0.70	13.40	4786	4108	2456	41	10
17	King 15	120.75	−0.95	0.46	12.29	2871	2467	1468	−48	3000
18	NGC 129	120.25	−2.54	0.57	11.20	1738	1501	876	−77	50
19	NGC 103	119.80	−1.38	0.55	12.90	3802	3299	1889	−92	20
20	Be 60	118.85	−1.64	...	...	...	...	...	...	...
21	Be 1	117.79	−2.03	...	...	...	...	...	...	...
22	Be 58	116.75	−1.29	0.55	12.95	3715	3317	1672	−84	251
23	NGC 7790	116.69	−1.01	0.55	12.75	3548	3170	1594	−63	71

TABLE 4

OBSERVED CLUSTERS: DERIVED PROPERTIES

Cluster Number (1)	Name (2)	R_{full} (arcmin) (3)	R_{full} (pc) (4)	R_{HWHM} (arcmin) (5)	R_{HWHM} (pc) (6)	$N_{cluster}$ ($V < 20$–21) (7)	$N_{observed}$ ($V < 20$–21) (8)
1	Be 7	2.05	1.53	1.19	0.89	71	723
2	NGC 663	4.42	3.62	2.69	2.21	413	3012
3	NGC 659	2.25	2.27	1.44	1.45	56	637
4	NGC 654	3.34	2.62	1.39	1.09	330	582
5	NGC 637	1.16	0.97	0.94	0.79	55	629
6	Tr 1	2.57	1.97	1.28	0.98	104	670
7	NGC 581	4.62	3.62	...	...	...	4680
8	NGC 457	6.22	5.46	3.59	3.15	588	3503
9	NGC 436	2.31	2.17	1.40	1.32	189	891
10	NGC 433	3.29	2.22	2.40	1.62	82	2119
11	NGC 381	3.17	0.98	1.81	0.56	71	2254
12	NGC 366	2.38	2.19	1.05	0.97	101	1014
13	Be 62	3.46	2.72	2.46	1.93	98	1572
14	Cz 2	...	...	...	...	...	2337
15	St 24	3.40	2.79	2.07	1.70	102	2121
16	NGC 146	3.40	4.73	2.10	2.92	79	620
17	King 15	4.53	3.78	2.55	2.13	150	1936
18	NGC 129	3.00	1.52	2.04	1.03	59	1158
19	NGC 103	3.85	4.26	1.90	2.10	295	2807
20	Be 60	...	...	...	...	...	206
21	Be 1	...	...	...	...	...	182
22	Be 58	2.15	2.32	1.59	1.72	41	412
23	NGC 7790	3.57	3.68	1.64	1.69	160	1723

TABLE 5

SUMMARY OF PREVIOUS RESULTS

Cluster	A_v	R_v	$E(B-V)$	$(m-M)_0$	D (pc)	Age (Myr)	Reference
NGC 663	...	...	0.8–1.0	11.55	2000	...	van den Bergh & de Roux 1978
	...	...	0.84	12.0	2512	...	Hoag 1966
	1.98	2.73	0.73	12.03	2500	9	Tapia et al. 1991
NGC 659	...	...	0.54	11.80	2290	...	McCuskey & Houk 1964
	...	...	(0.63)	11.79	2280	...	Steppe 1974
	...	...	...	12.39	3000	...	Alter 1944
NGC 654	...	2.9	0.77–1.13	11.9	2400	17	Stone 1980
	...	...	0.79–1.18	12.3	2900	...	Pesch 1960
	...	...	0.74–1.16	11.85	2400	...	Joshi & Sagar 1983
NGC 637	...	...	(0.43)	11.95	2450	...	Grubissich 1975
	...	...	0.66	11.99	2500	15	Huestamendia et al. 1991
Tr 1	1.73	...	...	11.70	2190	...	McCuskey & Houk 1964
	...	...	(0.61)	12.37	2980	...	Steppe 1974
	...	...	0.52	11.6	2089	26	Joshi & Sagar 1977
NGC 581	1.15	...	...	11.61	2100	...	McCuskey & Houk 1964
	...	...	0.39	11.94	2440	...	Moffat 1972
	...	...	(0.44)	12.46	3110	...	Steppe 1974
	...	...	0.40	11.84	2334	31	Osman et al. 1984
NGC 457	...	...	0.50	12.3	2880	...	Pesch 1959
	...	...	0.45	12.50	3160	...	Moffat 1972
	...	...	0.45	12.59	3300	...	Baade 1983
NGC 436	...	...	0.48	12.06	2582	63	Huestamendia et al. 1991
NGC 433	...	...	0.82	11.61	2100	<170	Battinelli et al. 1992
	...	...	...	13.27	4500		Alter 1944
NGC 381	...	...	0.35	10.97	950	320	Crinklaw & Talbert 1988
Be 62	...	3.0	0.86	11.56	2050	10	Forbes 1981
NGC 146	...	...	...	12.64	3370	...	Kimeswenger & Weinberger 1989
NGC 129	...	...	0.53	11.0	1590	...	Arp et al. 1959
	...	...	...	11.11	1670	...	Turner et al. 1992
	...	...	...	10.93	1535	...	Schmidt 1980
NGC 7790	...	...	0.54	12.65	3388	50–100	Romeo et al. 1989
	...	...	0.52	12.8	3630	...	Sandage 1958
	...	...	0.64	12.3	2884	...	Pedreros, Madore, & Freeman 1984

TABLE 6

COMPARISON WITH PREVIOUS PHOTOMETRY

	V			$(B-V)$			$(U-B)$				
CLUSTER	ΔV	σ	N_{stars}	$\Delta(B-V)$	σ	N_{stars}	$\Delta(U-B)$	σ	N_{stars}	DATA	REFERENCES
NGC 663	0.09	0.03	12	−0.03	0.03	12	0.01	0.06	6	pe	Hoag et al. 1961
NGC 659	0.06	0.09	33	0.10	0.11	33	...	...	...	pg	McCuskey & Houk 1964
NGC 654	0.00	0.04	34	0.00	0.05	34	−0.11	0.06	34	pg	Stone 1980
	0.01	0.07	21	0.00	0.03	21	−0.09	0.05	21	pe	Pesch 1960
	0.10	0.03	7	−0.02	0.02	7	−0.11	0.04	7	pe	Hoag et al. 1961
	−0.02	0.10	36	−0.01	0.05	36	−0.13	0.10	36	pe	Joshi & Sagar 1983
NGC 637	0.01	0.04	17	−0.03	0.03	17	−0.11	0.03	16	pe	Huestamendia et al. 1991
Tr 1	−0.14	0.14	43	0.14	0.11	43	−0.03	0.24	43	pg	McCuskey & Houk 1964
	0.17	0.21	19	0.12	0.11	17	0.06	0.18	17	pe	Joshi & Sagar 1977
NGC 581	0.13	0.17	31	0.06	0.09	31	−0.10	0.20	31	pg	McCuskey & Houk 1964
	−0.02	0.05	14	0.02	0.05	14	−0.01	0.07	13	pe	Hoag et al. 1961
NGC 457	−0.01	0.04	20	0.01	0.05	20	−0.03	0.03	20	pe	Hoag et al. 1961
NGC 436	0.00	0.16	28	−0.01	0.14	20	0.02	0.09	20	pe	Huestamendia et al. 1991
NGC 381	0.01	0.36	31	0.02	0.12	31	−0.01	0.16	31	pe	Crinklaw & Talbert 1988
Be 62	−0.01	0.14	13	−0.02	0.15	13	−0.03	0.07	13	pe	Forbes 1981

in any open cluster (Sanduleak 1990). Among the photometric studies (Table 5) are *UBV* investigations by van den Bergh & de Roux (1978), Hoag (1966), McCuskey & Houk (1964), and Hoag et al. (1961), as well as near-IR and Strömgren photometry by Tapia et al. (1991). Van den Bergh & de Roux (1978) find variable reddening across the face of NGC 663. Tapia et al. (1991) observed the brighter stars in NGC 663 with near-IR and Strömgren photometry and determined that the ratio of total to selective absorption, R_v, toward NGC 663 is 2.73 ± 0.20, below the average Galactic value of 3.1 (Whittet 1989). As they point out, however, the scatter in their $E(V-K)$ versus $E(B-V)$ diagram, which they used to determine R_v, is too large to conclude that R is definitely anomalous.

Our preliminary results for NGC 663 have been reported in Phelps & Janes (1991a). A map of the observed cluster field, based on the photometry from three mosaicked 1024×1024 pixel CCD images, is shown in Figure 15. The CMD and TCD for NGC 663 are shown in Figures 16*a* and 16*b*. The variable reddening in the cluster makes it difficult to determine whether a binary sequence is present. The characteristic wedge in the CMD, caused by field stars, is much less pronounced in the CMD of NGC 663 compared with other clusters in this region. The lack of field stars is consistent with the CO observations of this region (see Fig. 28 of Leisawitz et al. 1989), and suggests that NGC 663 is in front of a molecular cloud, quite possibly having emerged from it in the recent past. Because of the deficiency of field stars in the CMD, it is possible to trace the main sequence to faint magnitudes, indicating that NGC 663 contains a substantial number of low-mass stars.

Because of possible cloud cover during the portion of the evening when the cluster was observed, and the close agreement of the Hoag et al. (1961) photometry for other program clusters (see NGC 457 and NGC 581), our photometry was brought onto the system of Hoag et al. (1961) after applying the corrections listed in Table 6. Even with the shortest exposures, the brightest stars in the cluster were saturated on the CCD images, so values from Hoag et al. (1961) were used for these stars.

A fit of the SK82 MSTCC, using the standard reddening analysis, yields $E(B-V) = 0.80$ (Fig. 17*b*). The value of $E(B-V) = 0.80$ is consistent with the ZAMS fit in the CMD (Fig. 17*a*) between $16 < V < 19$, where the main sequence is tight and the fit is well constrained. A fit of the SK82 ZAMS gives an observed distance modulus of $(m-M)_v = 14.73$, corresponding to a true distance modulus of $(m-M)_0 = 12.25$, or a distance of 2818 pc (Fig. 17*a*).

Because variable reddening is indicated in the cluster, an individual dereddening analysis of the stars with $(B-V) < 0.7$ was also performed. The seven brightest stars, which deviate from the ZAMS in Figure 17*a*, were assumed to be of luminos-

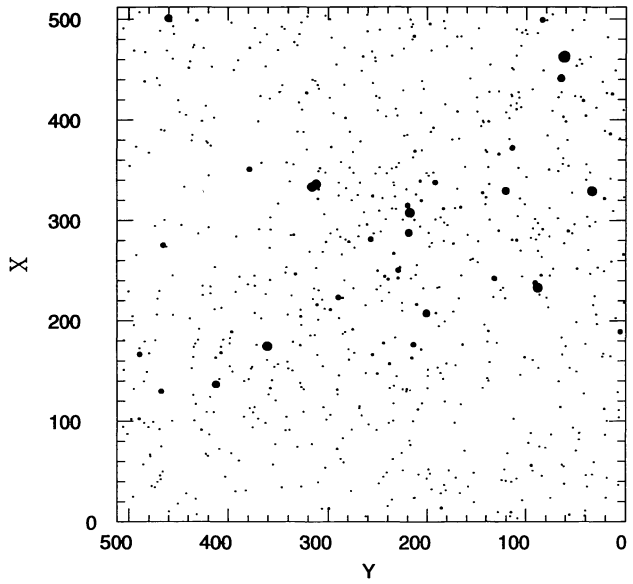

FIG. 12.—Map of Be 7 generated from the list of stars appearing in the color-magnitude diagram (CMD). The scale is $0\farcs77$ pixel^{-1}, giving a field of view of $6\farcm6$. North is up, and east is to the left.

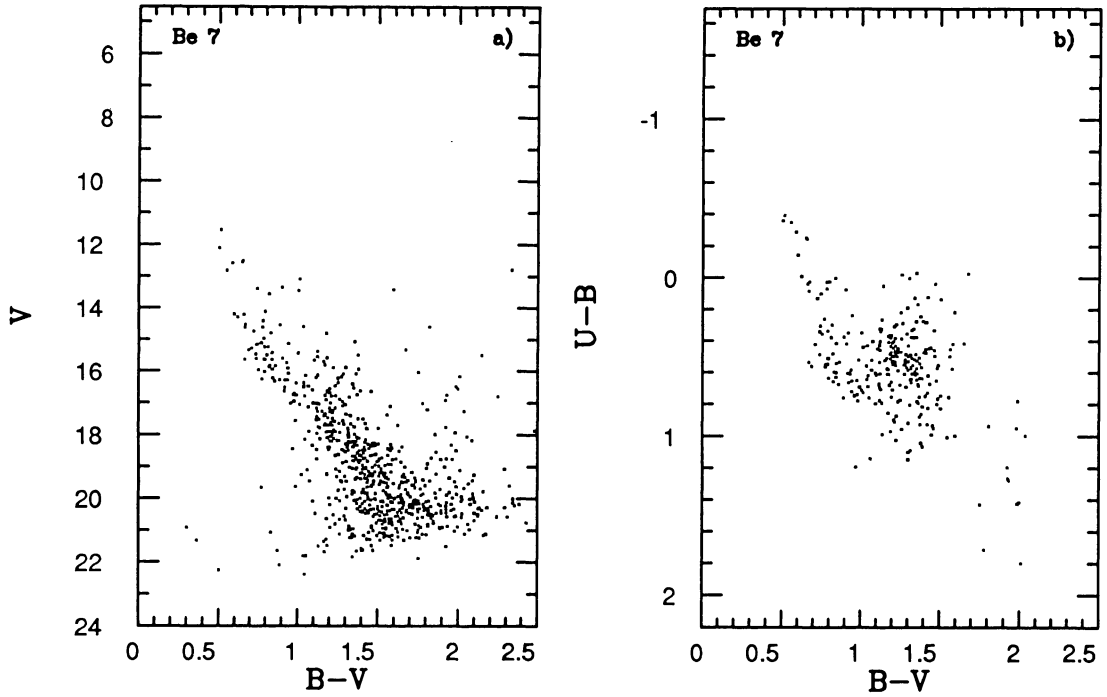

FIG. 13.—(*a*) Color-magnitude diagram for Be 7. (*b*) Two-color diagram for Be 7.

ity class Ib for the individual dereddening analysis, and the rest were assumed to be of luminosity class V. A range in color excess of $0.7 < E(B-V) < 1.0$, with a strong peak at $E(B-V) = 0.80$, is found. The reddening-corrected CMD is shown in Figure 18*a*. A narrow lower main sequence is observed with a substantial flaring at the high-mass end, so that a single isochrone cannot be fitted to the data. The data can be fitted reasonably well if it is assumed that there was an age spread in star formation of ~13–15 Myr, with some stars having been formed as recently as ~10–12 Myr ago (Fig. 18*b*). Data com-

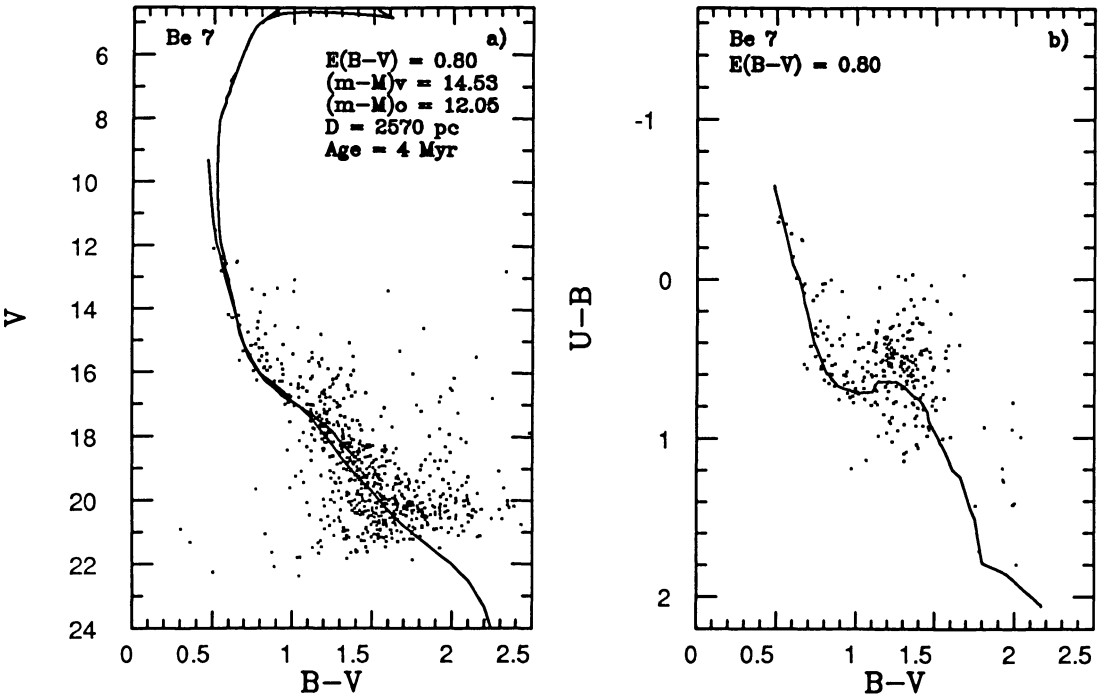

FIG. 14.—(*a*) Fit of the Schmidt-Kaler (1982) ZAMS and 4 Myr isochrone of Maeder & Meynet (1991) to Be 7. (*b*) Fit of the Schmidt-Kaler (1982) main-sequence two-color curve to Be 7.

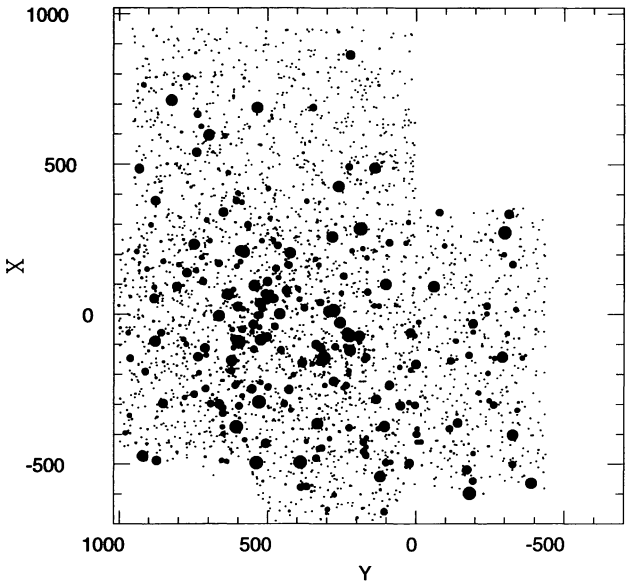

FIG. 15.—Map of NGC 663 generated from the list of stars appearing in the CMD. The scale is 0.″68 pixel^{-1}, giving a field of view of 19.′5. North is up, and east is to the left.

piled by Leisawitz (1988) from various studies of young clusters gives a median age of 21–22 Myr for NGC 663. The distance determined from the visual fit of the ZAMS in Figure 17*a* was used in the isochrone fitting in the dereddened CMD of Figure 18*b* and supports the distance derived from the full CMD of Figure 17*a*.

A noticeable deviation of stars from the ZAMS occurs for $V > 18$ (Fig. 17*a*), corresponding to $M_v \sim 3$. While the errors in the photometry begin to get large for the fainter magnitudes (Fig. 4), this deviation of stars above the main sequence is consistent with a PMS population of stars, assuming the younger 12 Myr age for the cluster (Stahler 1983). The lack of a substantial number of field stars in this direction, and the indications of a PMS population, make this cluster an ideal target for future studies of low-mass PMS stars.

5.3. *NGC 659*

Published photometry of NGC 659 includes a photographic *UBV* study by McCuskey & Houk (1964) and *RGU* photometry from Steppe (1974) (Table 5). The cluster was also cataloged by Alter (1944), who determined a distance of 3000 ± 250 pc.

Derived diagrams for NGC 659 are shown in Figures 19 and 20. For stars which were saturated in the images, the values of McCuskey & Houk (1964) were used, after adding offsets listed in Table 6, since the night of our observations was deemed to be photometric. The cluster exhibits no obvious binary sequence, although the scatter in the CMD makes an assessment of the binary content difficult.

Because of telescope problems, no *U*-band observations were obtained, so the reddening toward the cluster is uncertain. The McCuskey & Houk (1964) determination of $E(B - V)$ (Table 5) is most certainly incorrect, since no satisfactory fit of the SK82 ZAMS can be made in the CMD using this value. An estimate of $E(B - V)$ can be made using the *RGU* photometry of Steppe (1974). Using the relation in Alfaro & Garcia-Pelayo (1984) for the conversion of $E(G - R)$ to

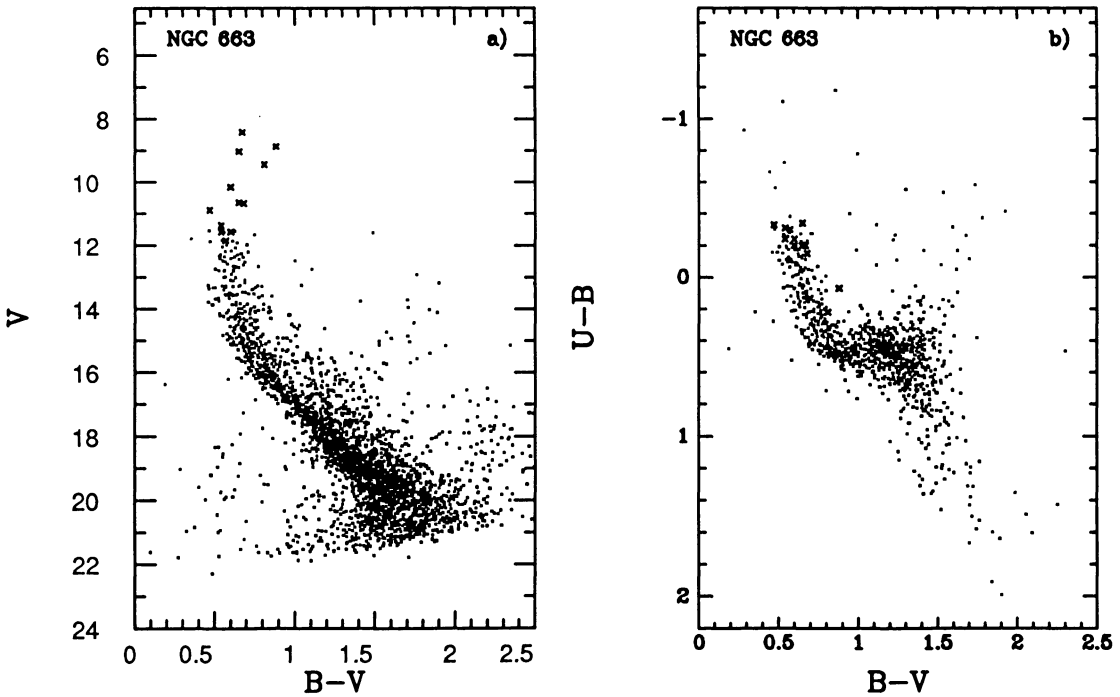

FIG. 16.—(*a*) Color-magnitude diagram for NGC 663. (*b*) Two-color diagram for NGC 663. Crosses represent stars whose photometry is taken from Hoag et al. (1961).

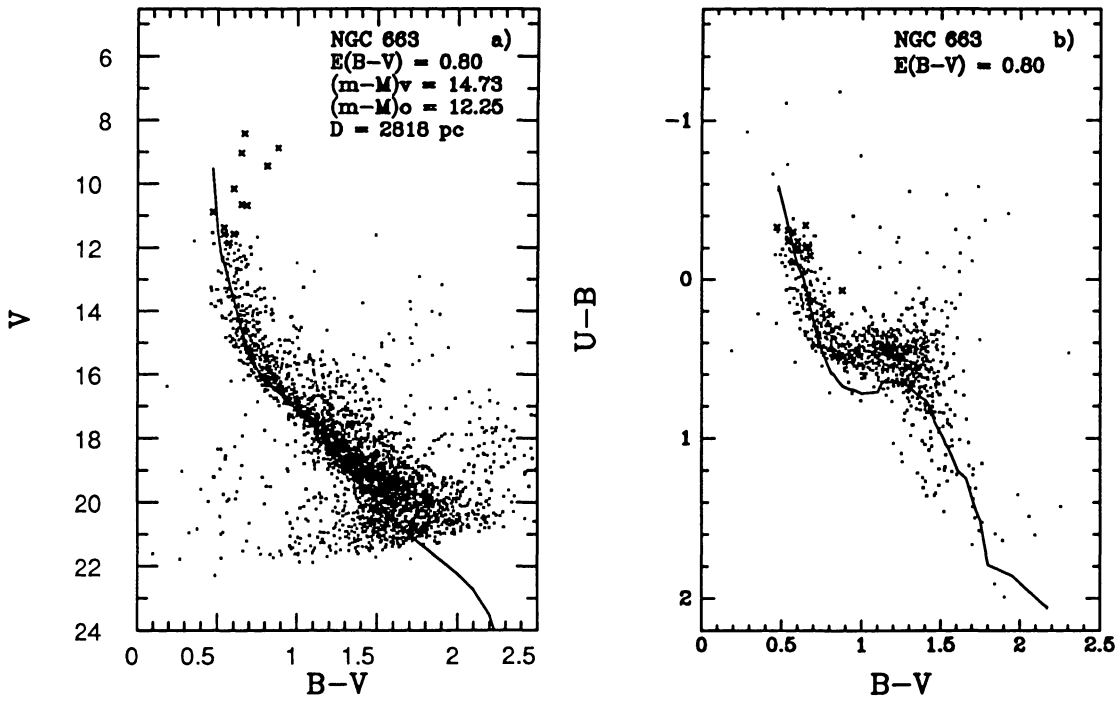

FIG. 17.—(*a*) Fit of the Schmidt-Kaler (1982) ZAMS to NGC 663. (*b*) Fit of the Schmidt-Kaler (1982) main-sequence two-color curve to NGC 663. Crosses represent stars whose photometry is taken from Hoag et al. (1961).

$E(B-V)$,

$$E(B-V) = 0.72E(G-R) - 0.006E^2(G-R)\,, \quad (15)$$

gives $E(B-V) = 0.63$. With this value a fit of the SK82 ZAMS gives $(m-M)_v = 14.65$, which corresponds to $(m-M)_0 = 12.70$, or a distance of 3467 pc (Fig. 20*b*). This distance is considerably greater than that found by McCuskey & Houk (1964) and Steppe (1974), but is in general agreement with that found by Alter (1944). The age of NGC 659 is inferred to be 12 Myr (Fig. 20*b*).

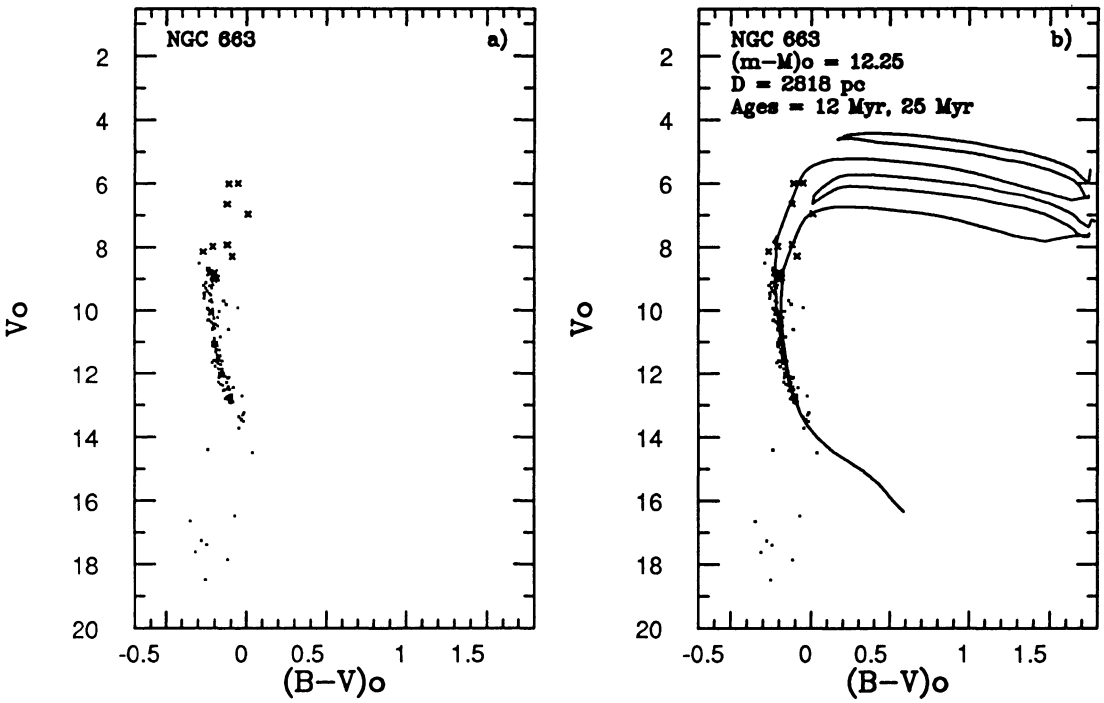

FIG. 18.—(*a*) Reddening-corrected CMD for stars with $(B-V) < 0.70$. (*b*) Fit of the 12 and 25 Myr isochrones of Maeder & Meynet (1991) to the reddening-corrected CMD of NGC 663. Crosses represent stars whose photometry is taken from Hoag et al. (1961).

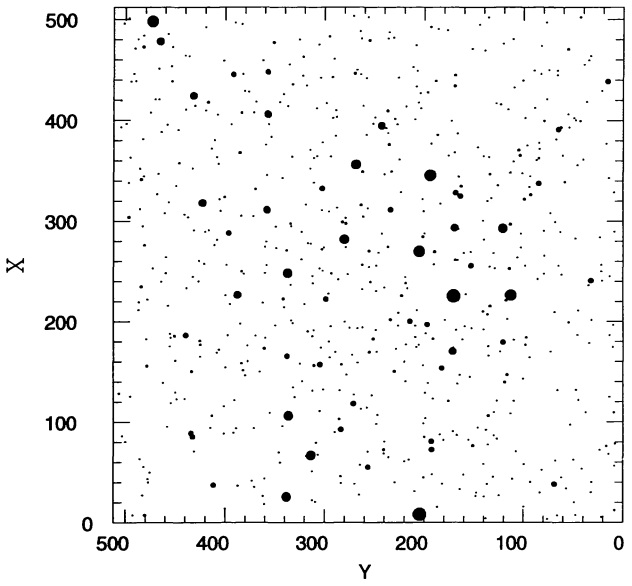

FIG. 19.—Map of NGC 659 generated from the list of stars appearing in the CMD. The scale is 0".77 pixel^{-1}, giving a field of view of 6'.6. North is up, and east is to the left.

5.4. *NGC 654*

NGC 654 has been observed by Pesch (1960), Hoag et al. (1961), McCuskey & Houk (1964), Moffat (1972), Samson (1975), Stone (1980), Joshi & Sagar (1983), and Sagar & Yu (1989) (Table 5), but none of these investigations were based on CCD photometry, nor did they reach the fainter magnitudes of this study. The reddening across the cluster is highly variable and has been interpreted as being due to residual material from the cluster's formation (Samson 1975) or as a local cloud in the direction of the cluster (Stone 1977; McCuskey & Houk 1964).

Because of bright stars in the cluster field, our CCD images were restricted to a single field covering only a portion of the cluster. The resulting diagrams for NGC 654 are shown in Figures 21–24. A comparison of 36 stars in common with Joshi & Sagar (1983) shows good agreement in V and $(B - V)$, but the Joshi & Sagar data are systematically offset in $(U - B)$ by −0.126 mag (Table 6). Comparisons between our photometry and that of Pesch (1960) and Stone (1980) give similar results, but the Joshi & Sagar (1983) and Stone (1980) studies used the Pesch (1960) values as local standards, so the agreement is not surprising. A comparison of seven stars we observed in common with Hoag et al. (1961) shows good agreement in $(B - V)$, but poorer agreement in V and $(U - B)$ (Table 6). In a detailed comparison of their photometry of NGC 654 with that of Pesch (1960), McCuskey & Houk found significant zero-point differences, with the Pesch values being nearly 0.1 mag fainter in V and ~0.03 mag bluer in $(B - V)$ (both in agreement with Hoag et al.), and ~0.06 mag redder in $(U - B)$ (in agreement with this study). There is no trend in the comparisons to establish which set or sets of data is closest to the *UBV* system. Based upon this comparison, and the likely photometric nature of the sky during our observations, there is no compelling reason to make corrections to our data set to bring it onto one of the other systems, although the difference in $(U - B)$ remains unexplained. The brighter stars from Joshi & Sagar (1983), which were not included in the present photometry either because of saturation on the CCD

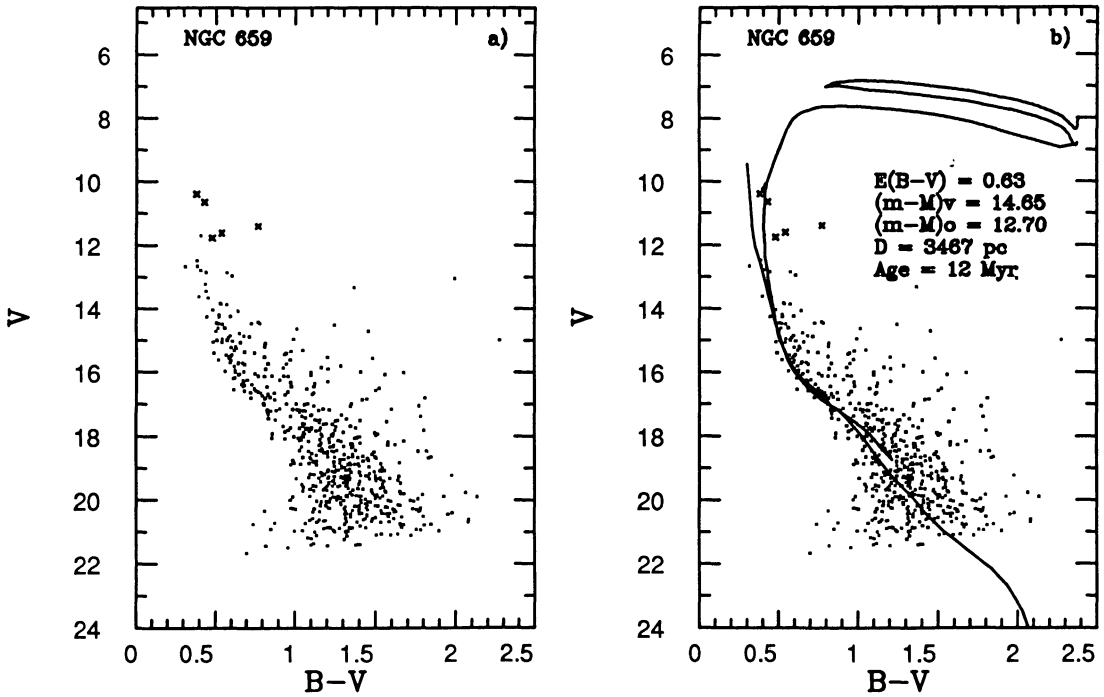

FIG. 20.—(*a*) Color-magnitude diagram for NGC 659. (*b*) Fit of the Schmidt-Kaler (1982) ZAMS and 12 Myr isochrone of Maeder & Meynet (1991) to NGC 659. Crosses represent stars taken from McCuskey & Houk (1964).

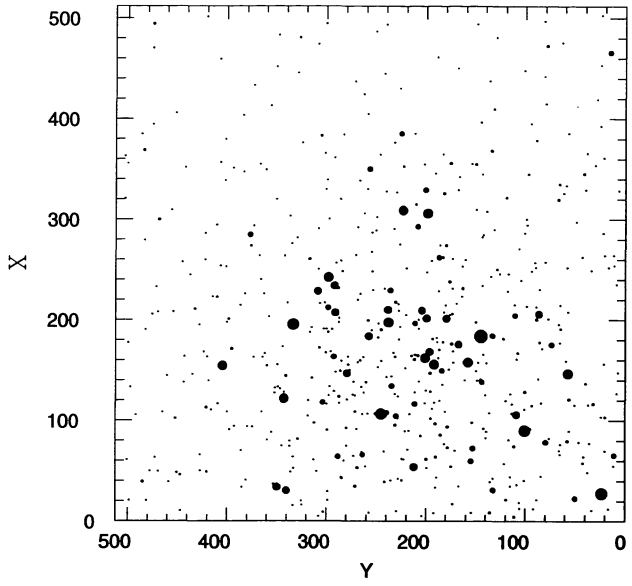

FIG. 21.—Map of NGC 654 generated from the list of stars appearing in the CMD. The scale is 0.″77 pixel^{-1}, giving a field of view of 6.′6. North is up, and east is to the left.

or because they were outside the observed field, were transformed onto the system of the present study. Stars in the Joshi & Sagar list which are outside the field observed in this study were included only if they have membership probabilities (Stone 1977) greater than 0.80.

The striking aspect of the CMD (Fig. 22*a*) is the lack of the characteristic wedge-shaped distribution of field stars that is seen in most of the other CMDs. This allows the main sequence to be seen to faint magnitudes and indicates that NGC 654 contains a substantial number of low-mass stars. The main sequence is quite wide, but the lower edge is sharply defined, indicating that a substantial number of binaries may be present in the cluster, although the high and variable nature of the reddening makes the binary content difficult to ascertain. Presumably, NGC 654 lies front of a molecular cloud, reducing the visibility of background field stars. This conclusion is consistent with radio observations (Leisawitz et al. 1989) which show a great deal of CO toward the cluster.

A visual fit of the SK82 MSTCC gives a mean reddening of 0.90 (Fig. 23*b*). A fit of the SK82 ZAMS gives $(m - M)_v$ = 14.94, corresponding to $(m - M)_0$ = 12.15, or a distance of 2692 pc (Fig. 23*a*). The substantial scatter in the upper end of the CMD and two-color diagrams indicates that the reddening is variable, but the well-defined lower edge to its main sequence suggests that the variations are intrinsic to the individual stars rather than being caused by a patchy distribution of dust in or around the cluster. An individual dereddening analysis of the stars in NGC 654 was therefore performed. The majority of the stars were dereddened as luminosity class V stars, but since the brightest star (star 111 in the list of Joshi & Sagar 1983) is classified as an F5 Ia star (Stone 1977), and star 68 [V = 9.56, $(B - V)$ = 0.88] in Joshi & Sagar's (1983) list is classified as an A0 Ib star, intrinsic colors for the appropriate luminosity classes were taken from SK82 to obtain the reddening.

A range in reddening of $0.75 < E(B - V) < 1.1$ was found, in good agreement with previous studies. The reddening-

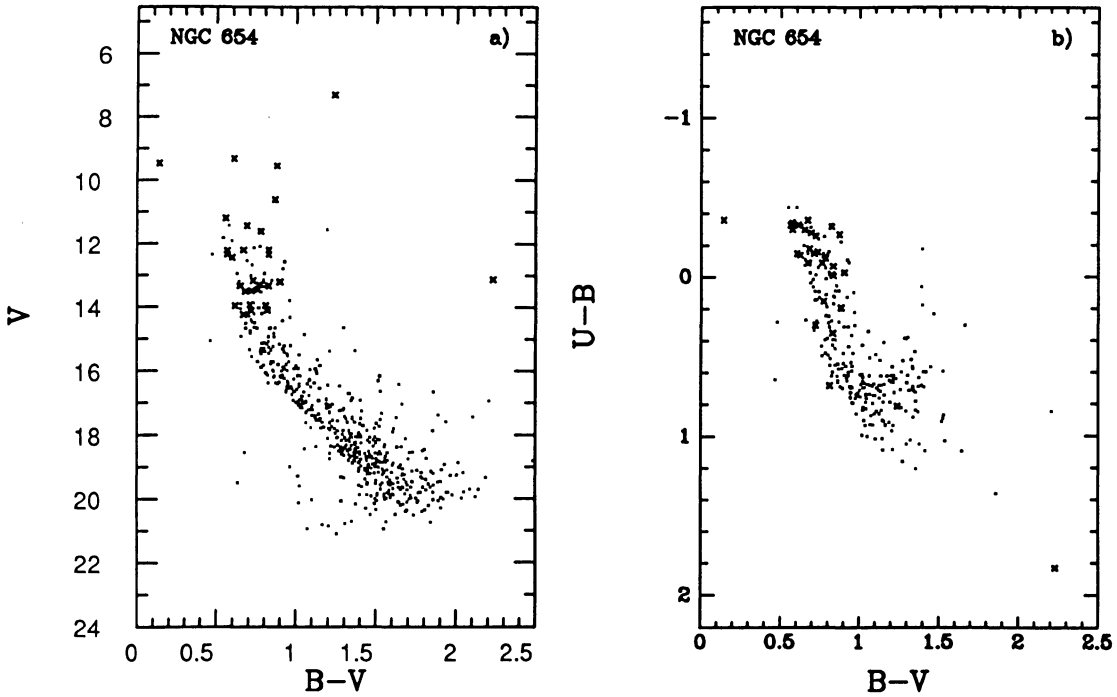

FIG. 22.—(*a*) Color-magnitude diagram for NGC 654. (*b*) Two-color diagram for NGC 654. Crosses represent stars whose photometry is taken from Joshi & Sagar (1983).

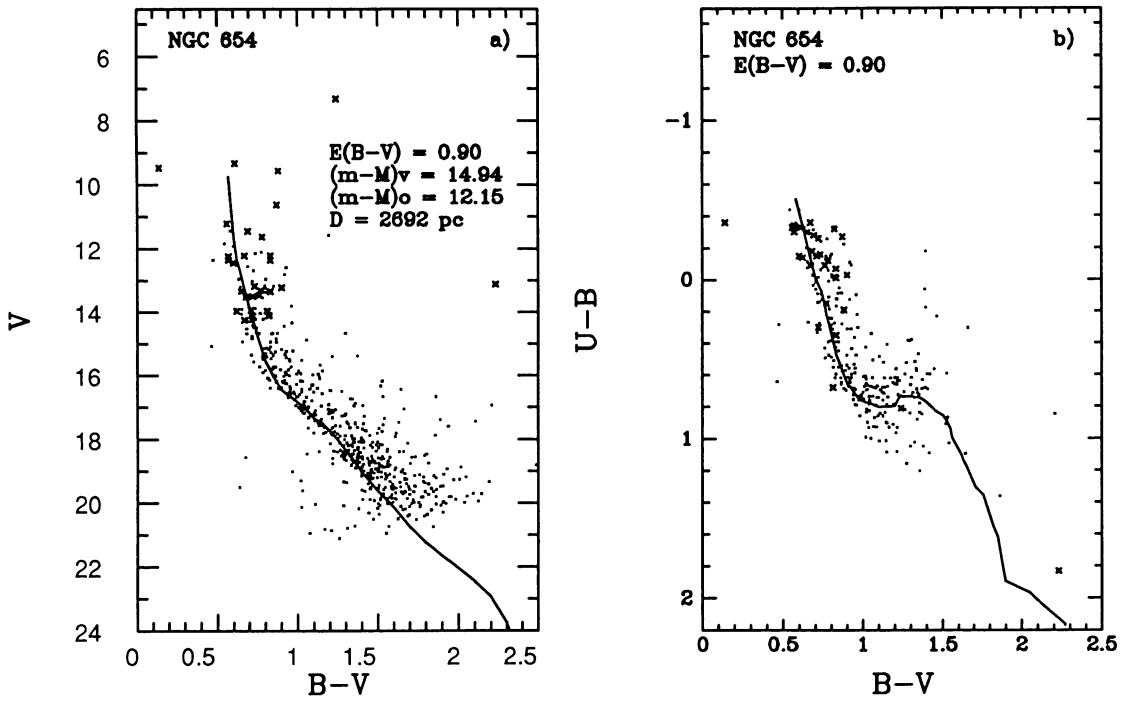

FIG. 23.—(*a*) Fit of the Schmidt-Kaler (1982) ZAMS to NGC 654. (*b*) Fit of the Schmidt-Kaler (1982) main-sequence two-color curve to NGC 654. Crosses represent stars whose photometry is taken from Joshi & Sagar (1983).

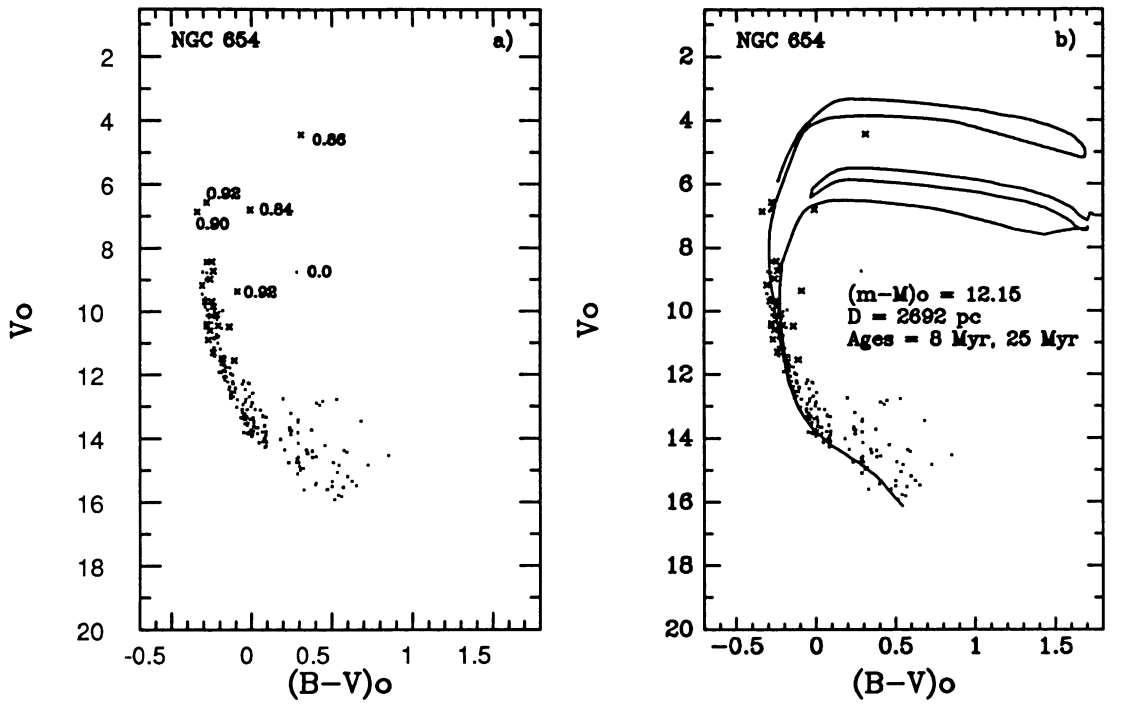

FIG. 24.—(*a*) Reddening-corrected CMD for NGC 654. (*b*) Fit of the 8 and 25 Myr isochrones of Maeder & Meynet (1991) to the reddening-corrected CMD of NGC 654. Crosses represent stars whose photometry is taken from Joshi & Sagar (1983).

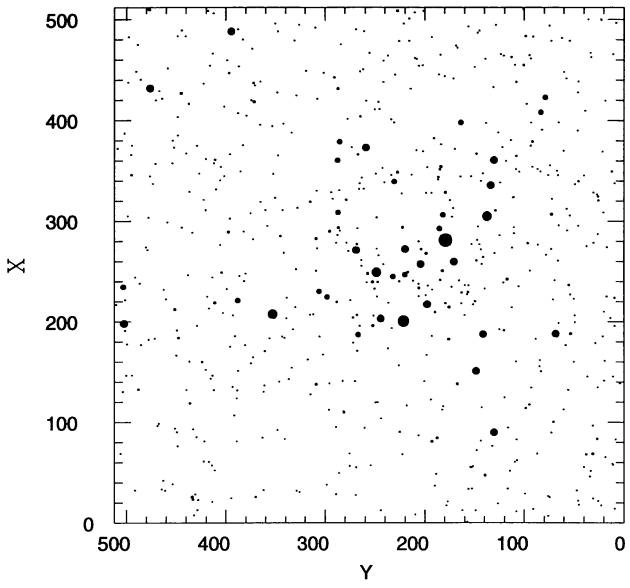

FIG. 25.—Map of NGC 637 generated from the list of stars appearing in the CMD. The scale is 0.″77 pixel^{-1}, giving a field of view of 6.′6. North is up, and east is to the left.

corrected CMD is shown in Figure 24*a*, with membership probabilities (Stone 1977) for selected stars indicated. Even after restricting the sample to stars with high membership probabilities, the CMD cannot be fitted by a single isochrone. Figure 24*b* shows isochrones of 8 and 25 Myr. It thus appears that the time spread of star formation in NGC 654 is at least ~20 Myr, and possibly longer if one were to include the star with a membership probability of 0.92 (star 5 in Joshi & Sagar 1983 with $V_0 = 9.368$, $(B - V)_0 = -0.090$).

5.5. *NGC 637*

NGC 637 was observed by Grubissich (1975) in the *RGU* system, and by Huestamendia, del Rio, & Mermilliod (1991) in the *UBV* system (Table 5).

Diagrams for NGC 637 are shown in Figures 25–27. The photometric values of Huestamendia et al. (1991) for the stars which were saturated on our CCD frames (their stars numbered 1, 3, 4, 6, 7, 73, and 74) were used after applying the offsets listed in Table 6 to put them onto our system. The differences in V and $(B - V)$ are small, but a much larger offset in $(U - B)$ is found which is unexplained.

As pointed out by Huestamendia et al. (1991), there is a noticeable gap in the main sequence in the range $11 < V < 12$ (Fig. 26*a*). The fit of the SK82 MSTCC gives a reddening of $E(B - V) = 0.65$ (Fig. 27*b*), while the fit of the SK82 ZAMS gives $(m - M)_v = 14.32$, corresponding to $(m - M)_0 = 12.30$, or a distance of 2884 pc (Fig. 27*a*). Our derived distance is larger than the distance determined by Huestamendia et al. (1991), most likely because they were only able to fit the more nearly vertical portion of the CMD. The isochrones best match the cluster for an age of ~4 Myr (Fig. 27*a*), a considerably younger age than Huestamendia et al. (1991) found, but consistent with the MSTCC fit in the two-color diagram, and in general agreement with the earliest main-sequence spectral type of B0 as given by Becker (1971). We find a nearly identical cluster reddening to that found by Huestamendia et al.

In the CMD of Figure 26*a* there is no apparent binary sequence, although the contrast between the cluster and the field is less in this cluster compared with some of the other clusters,

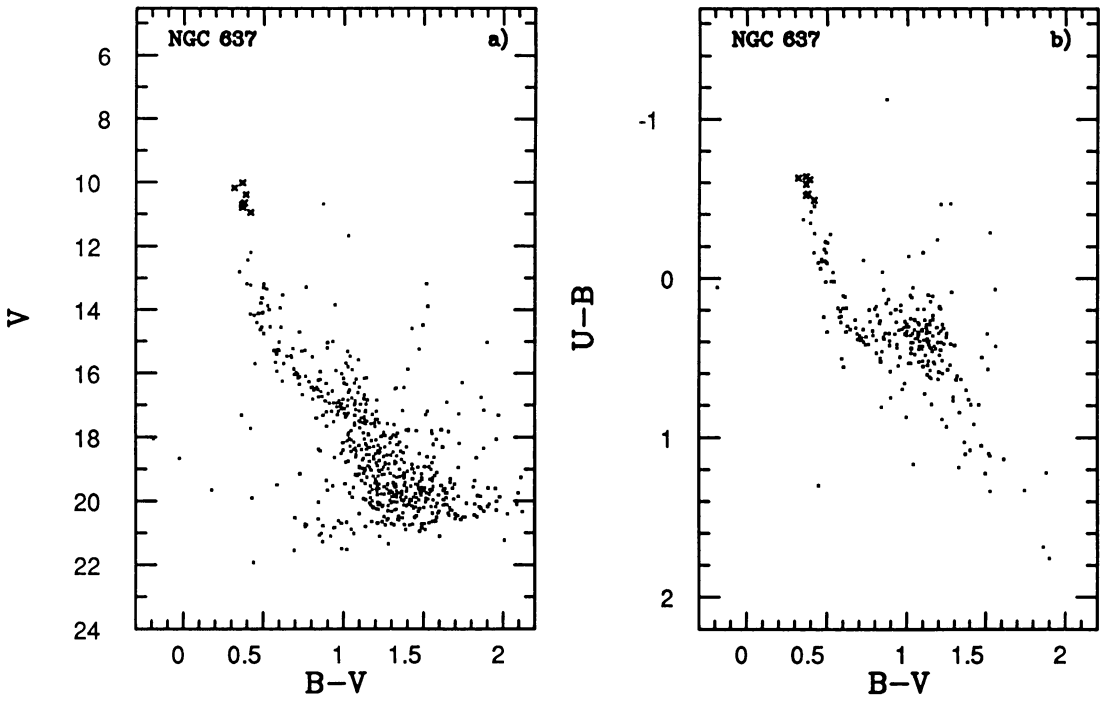

FIG. 26.—(*a*) Color-magnitude diagram for NGC 637. (*b*) Two-color diagram for NGC 637.

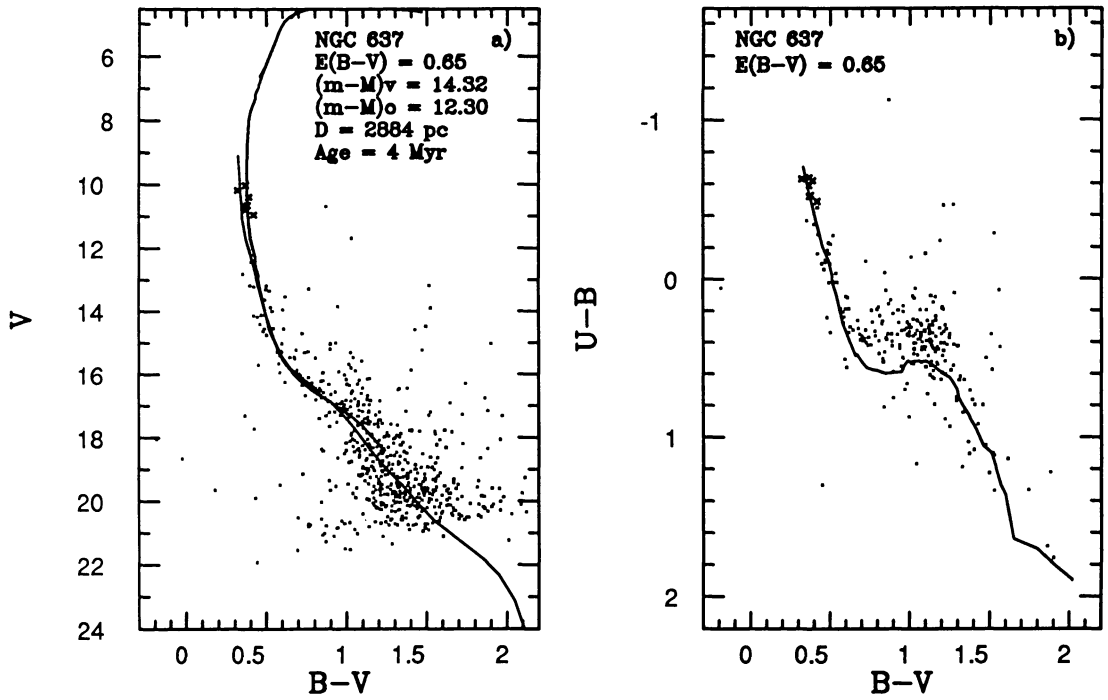

FIG. 27.—(*a*) Fit of the Schmidt-Kaler (1982) ZAMS and 4 Myr isochrone of Maeder & Meynet (1991) to NGC 637. (*b*) Fit of the Schmidt-Kaler (1982) main-sequence two-color curve to NGC 637.

making a determination of the binary content difficult. A main sequence is clearly visible to a V-magnitude of 18, with little trace continuing into the field star distribution.

5.6. *Trumpler 1*

McCuskey & Houk (1964) included Trumpler 1 (Tr 1) in their photographic study of several clusters in Cassiopeia; Steppe (1974) obtained *RGU* photometry of the cluster along with NGC 581 and NGC 659; Oja (1966) did a proper-motion study of the cluster; and Joshi & Sagar (1977) conducted a photoelectric study of the cluster (Table 5). Despite the differences between our data set and that of McCuskey & Houk (1964) and Joshi & Sagar (1977) (Table 6), our data set is likely to be the closest to the *UBV* system. Photometry of NGC 581 (see below), obtained just before Tr 1, on the same night, showed no significant differences relative to previous photometry by Hoag et al. (1961), indicating that the night was photometric. No change in the sky was noted during the night. The close agreement of our photometry for NGC 581 with Hoag et al. (1961) suggests that there is no compelling reason to doubt the accuracy of the Tr 1 photometry. In order to add the brightest stars, which were saturated in the CCD images, stars 1143 and 1158 in the list of Joshi & Sagar (1977) were included after correcting for the offsets between our data and those of Joshi & Sagar (1977).

Our derived diagrams for Tr 1 are found in Figures 28–30. The CMD of Figure 29*a* shows a distinct main sequence down to $V \sim 18$ before it merges with the field star distribution. At fainter magnitudes there remains a trace of the main sequence, indicating that Tr 1 contains lower mass stars. There is no obvious binary sequence in the cluster, although the main-sequence width may be due to binary stars or simply due to reddening effects.

The fit of the SK82 MSTCC gives a reddening of $E(B-V) = 0.61$ (Fig. 30*b*), while a fit of the SK82 ZAMS gives $(m-M)_v = 13.99$, corresponding to $(m-M)_0 = 12.10$, or a distance of 2630 pc (Fig. 30*a*). An age of 27 Myr is found (Fig.

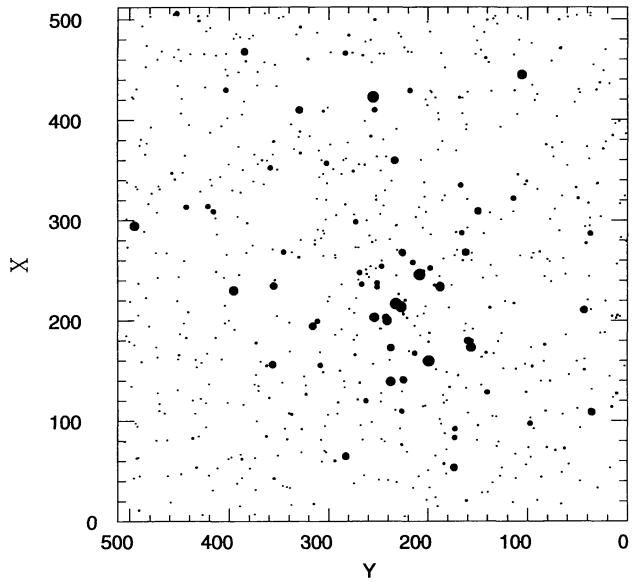

FIG. 28.—Map of Tr 1 generated from the list of stars appearing in the CMD. The scale is 0.″77 pixel^{-1}, giving a field of view of 6.′6. North is up, and east is to the left.

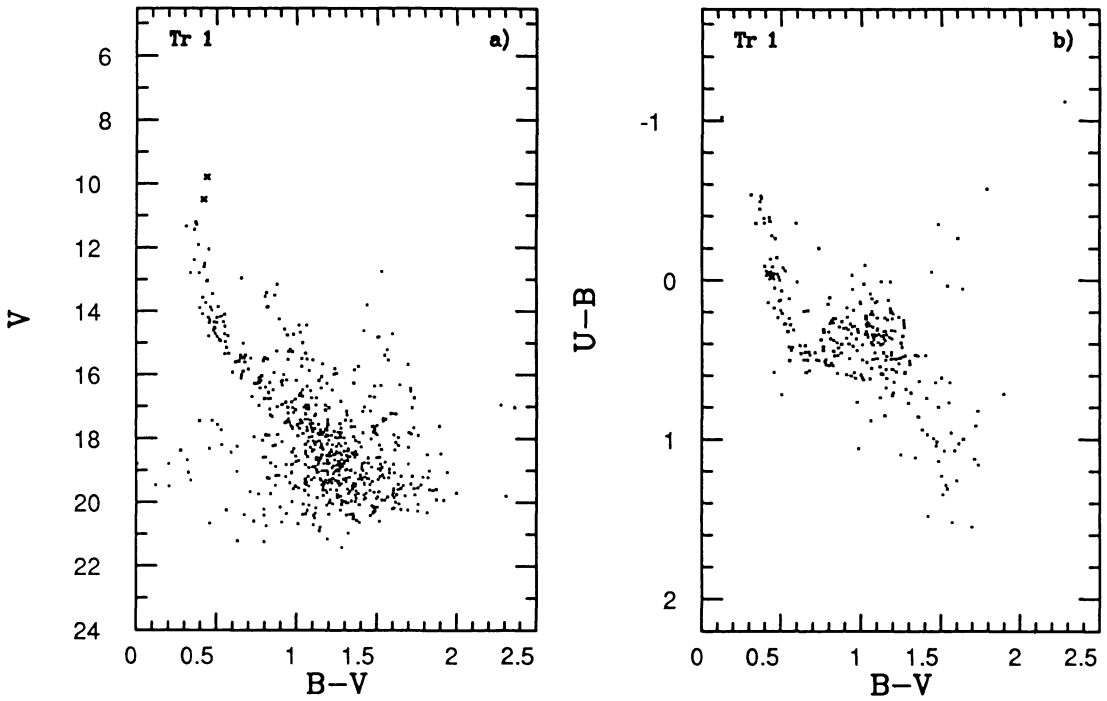

FIG. 29.—(*a*) Color-magnitude diagram for Tr 1. (*b*) Two-color diagram for NGC Tr 1. Crosses represent stars taken from Joshi & Sagar (1977).

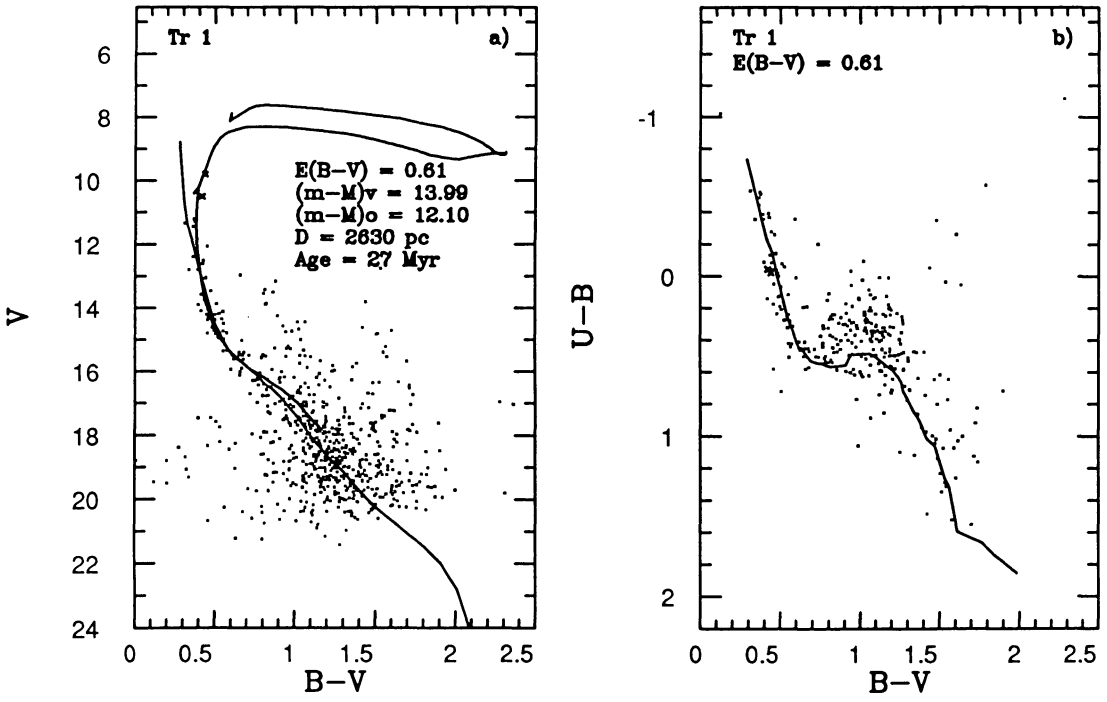

FIG. 30.—(*a*) Fit of the Schmidt-Kaler (1982) ZAMS and 27 Myr isochrone of Maeder & Meynet (1991) to Tr 1. (*b*) Fit of the Schmidt-Kaler (1982) main-sequence two-color curve to Tr 1. Crosses represent stars taken from Joshi & Sagar (1977).

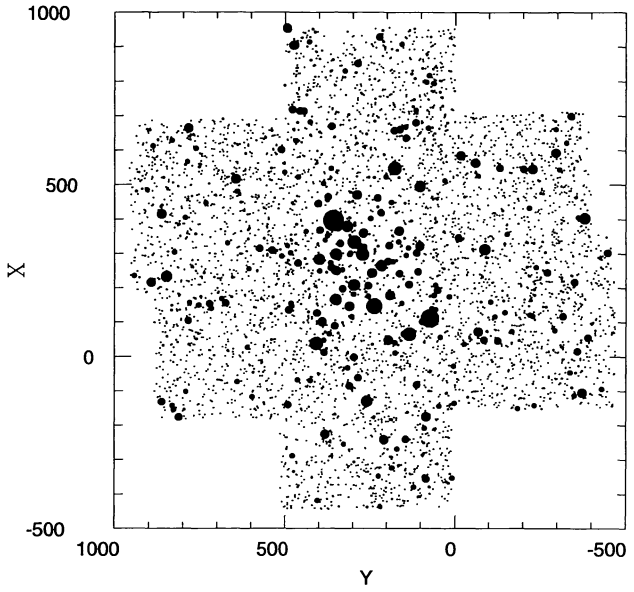

FIG. 31.—Map of NGC 581 generated from the list of stars appearing in the CMD. The map is composed of a mosaic of seven CCD frames. The scale is 0.″77 pixel^{-1}, giving a field of view of 19.′3. North is up, and east is to the left.

30*a*), in good agreement with the age determined by Joshi & Sagar (1977).

5.7. *NGC 581*

Previous studies of NGC 581 (Messier 103) include the photographic *UBV* studies of Hoag et al. (1961), McCuskey & Houk (1964), Moffat (1972), and Osman et al. (1984), and an *RGU* study by Steppe (1974) (Table 5).

Our preliminary results for NGC 581 have been reported in Phelps & Janes (1991b). Those results are expanded upon here, with the derived diagrams shown in Figures 31–33.

A mosaic of seven 512 × 512 CCD frames was used to observe the cluster. The photometric values from Hoag et al. (1961) were used, with the small corrections listed in Table 6 for the six brightest stars which were saturated in our CCD images. One red star, classified as spectral type M0.5 Ib by Keenan & Pitts (1985), was observed by McCuskey & Houk (1964) (star 27) but not by Hoag et al. (1961). The McCuskey & Houk (1964) photometry for this star was put onto the system of this study with the offsets listed in Table 6, and its position is indicated by an open box in Figures 32 and 33.

Our CCD photometry shows NGC 581 to have a mean reddening of $E(B-V) = 0.44$ (Fig. 33*b*), $(m-M)_v = 13.51$, $(m-M)_0 = 12.51$, or a distance of 2692 pc (Fig. 33*a*). While the 10 Myr isochrone fits the distribution of stars in the CMD quite well (Fig. 33*a*), several stars which would be expected to have evolved off of the main sequence at an age of 10 Myr remain on the ZAMS. The M0.5 Ib star can be fitted with an isochrone of ~22 Myr. NGC 581, therefore, appears to have a spread in formation times of its stars of at least ~10 Myr. MM91 have used NGC 581 in a study of the role of convective overshooting in stellar isochrone models. For NGC 581 they find $E(B-V) = 0.40$, $(m-M)_v = 13.40$, $(m-M)_0 = 12.16$ (2704 pc), and an age of 22 Myr, in excellent agreement with the current results.

Our photometry of the central field of NGC 581 suffers from incompleteness because of the shorter exposures needed due to the presence of three 7th to 9th magnitude stars in that region.

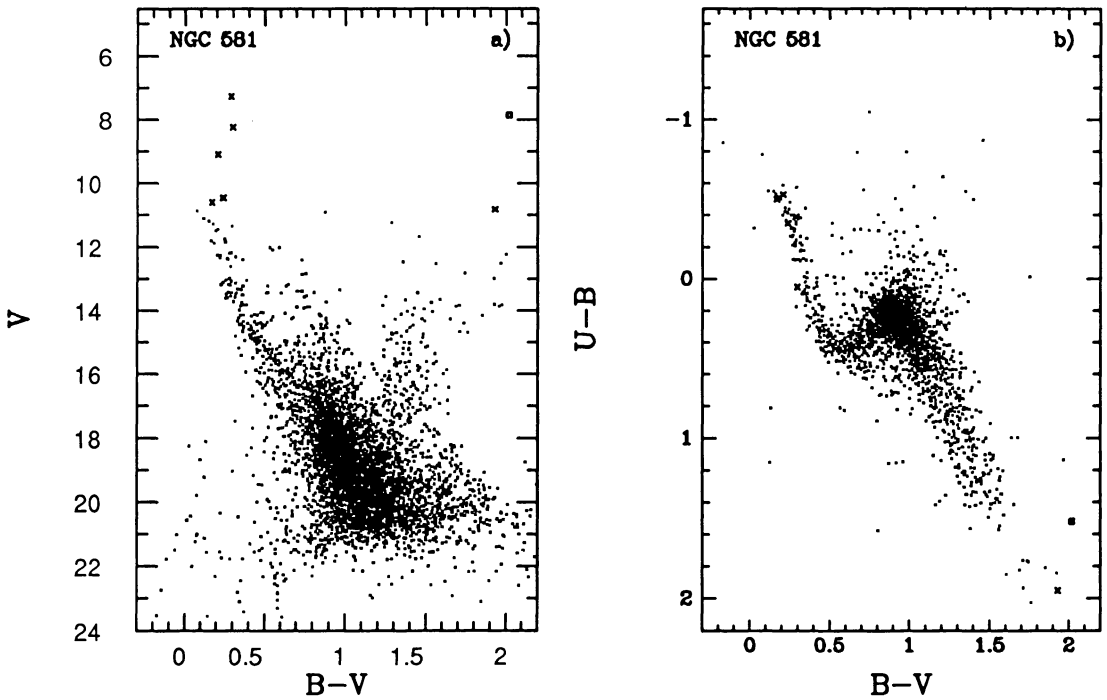

FIG. 32.—(*a*) Color-magnitude diagram for NGC 581. (*b*) Two-color diagram for NGC 581. Crosses represent stars taken from Hoag et al. (1961). The open square is star 27 in the list of McCuskey & Houk (1964).

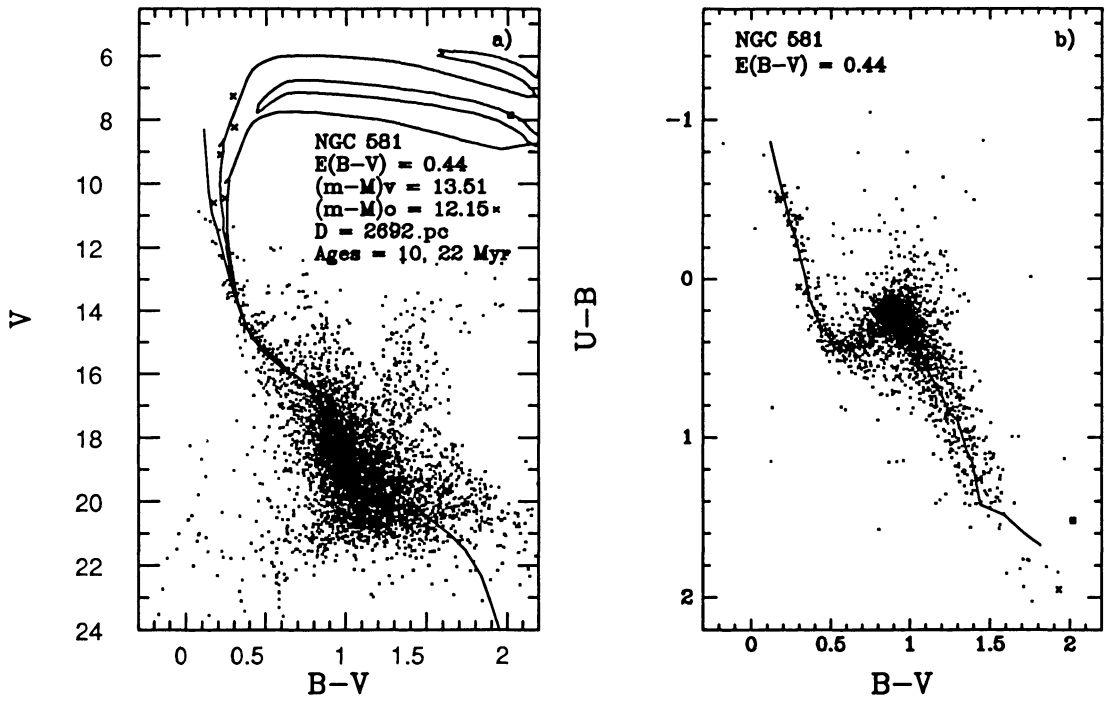

FIG. 33.—(*a*) Fit of the Schmidt-Kaler (1982) ZAMS and 10 and 22 Myr isochrones of Maeder & Meynet (1991) to NGC 581. (*b*) Fit of the Schmidt-Kaler (1982) main-sequence two-color curve to NGC 581. Crosses represent stars taken from Hoag et al. (1961). The open square is star 27 in the list of McCuskey & Houk (1964).

It was not, therefore, possible to obtain the half-width at half-maximum (HWHM) radius, $R_{\rm HWHM}$ (Table 4).

The main sequence of NGC 581 continues into the field star distribution, indicating that NGC 581 contains numerous lower mass stars. Another striking aspect of the CMD is the tightness of the main sequence for $15 < V < 17$ ($1.5 < M_v < 3.5$), just below the portion of the CMD where evolution off of the main sequence results in a spread. There is no obvious binary sequence in this range, in contrast to NGC 457 and NGC 436, where obvious binary sequences are observed.

5.8. *NGC 457*

NGC 457 is a bright cluster that has been the subject of numerous photometric studies (e.g., Pesch 1959; Jones & Hoag 1968; Hoag et al. 1961; Moffat 1972; Baade 1983; see Table 5).

Our diagrams for NGC 457 are shown in Figures 34–36. CCD photometry is difficult because of the 5th magnitude star ϕ Cas at the edge of the cluster. The CCD photometry of this study consists of a mosaic of eight 6'.6 frames with the TEK 1 512 × 512 chip (Fig. 34). The mosaic avoided the region surrounding ϕ Cas for practical reasons and therefore missed a portion of the cluster.

Photometric values from the Hoag et al. (1961) study for the brightest stars which were outside the CCD mosaic, as well as the stars in the images that were saturated, were included in our study of the cluster after applying the offsets listed in Table 6. Additionally, a red supergiant has been included (Boden 25) from the study of the cluster by Boden (1946). A distinct main sequence, along with a very pronounced binary sequence ~0.75 mag above the main sequence, is evident in the CMD (Fig. 35). The fit of the SK82 MSTCC gives $E(B-V) = 0.49$ (Fig. 36*b*), while the SK82 ZAMS fit gives $(m-M)_v = 13.92$, or $(m-M)_0 = 12.40$ (3020 pc) as seen in Figure 36*a*. The brightest stars in the NGC 457 CMD can be fitted quite well by an isochrome of 7 Myr (Fig. 36*a*). The distribution of stars in the CMD in the range $10 < V < 14$, however, is too nearly

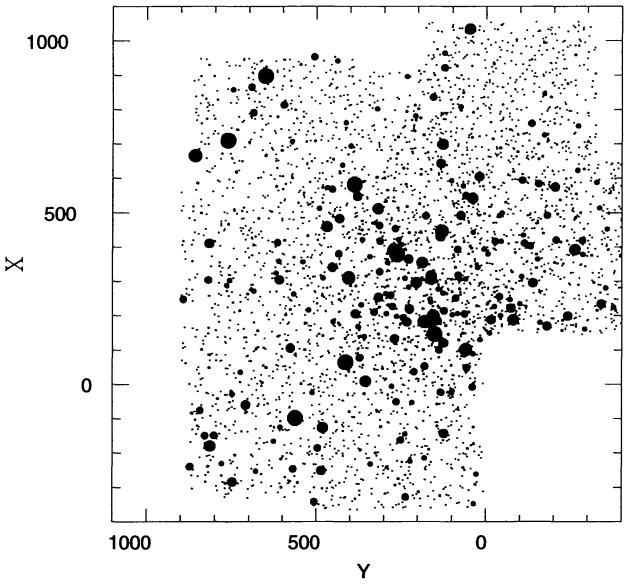

FIG. 34.—Map of NGC 457 generated from the list of stars appearing in the CMD. The map is composed of a mosaic of eight CCD frames. The scale is 0".77 pixel^{-1}, giving a field of view of 20'.5. North is up, and east is to the left.

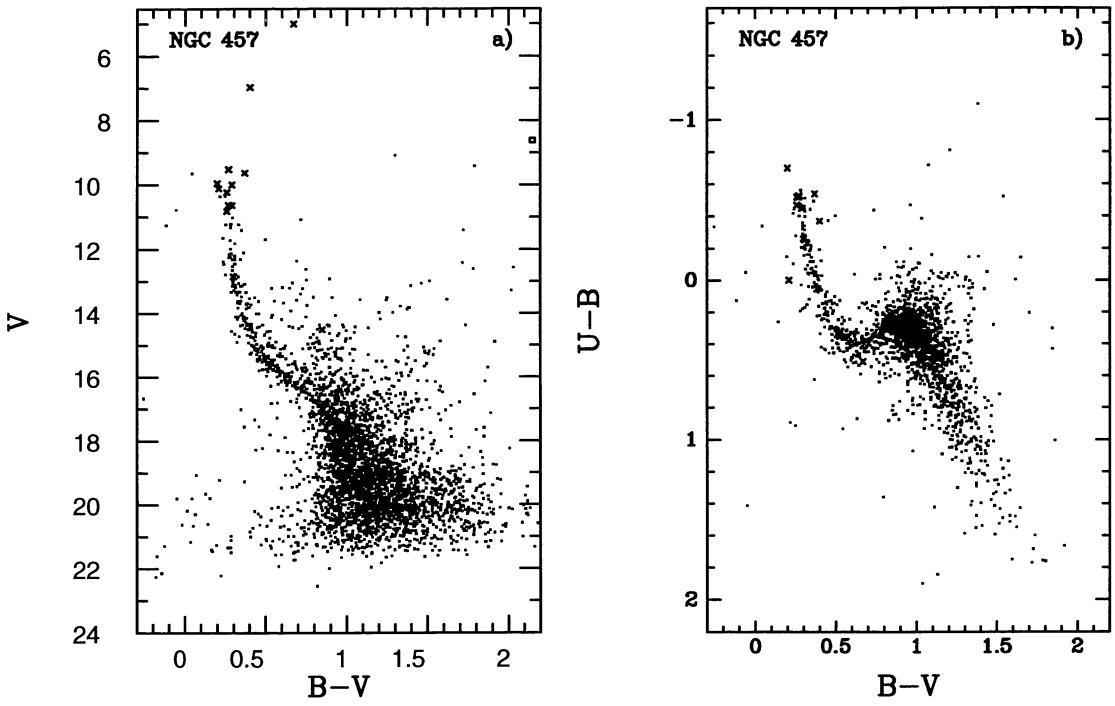

FIG. 35.—(*a*) Color-magnitude diagram for NGC 457. (*b*) Two-color diagram for NGC 457. Crosses represent stars taken from Hoag et al. (1961). The open square is the star Boden 25, with measurements taken from Boden (1946).

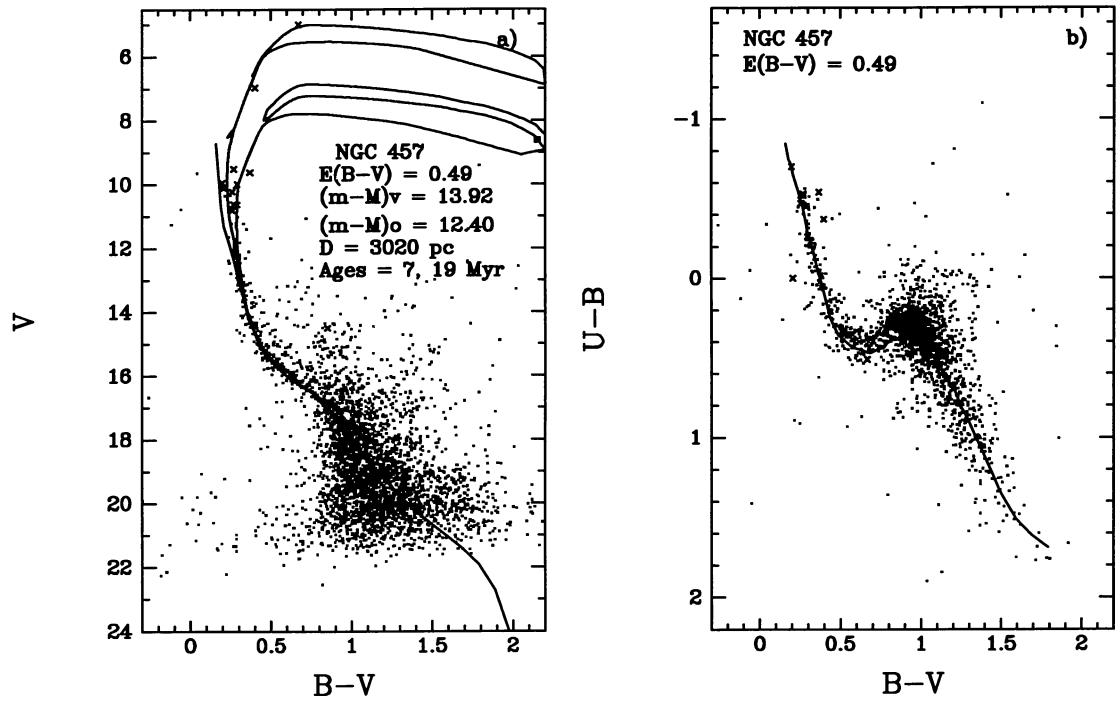

FIG. 36.—(*a*) Fit of the Schmidt-Kaler (1982) ZAMS and 7 and 19 Myr isochrones of Maeder & Meynet (1991) to NGC 457. (*b*) Fit of the Schmidt-Kaler (1982) main-sequence two-color curve to NGC 457. Crosses represent stars taken from Hoag et al. (1961). The open square is the star Boden 25, with measurements taken from Boden (1946).

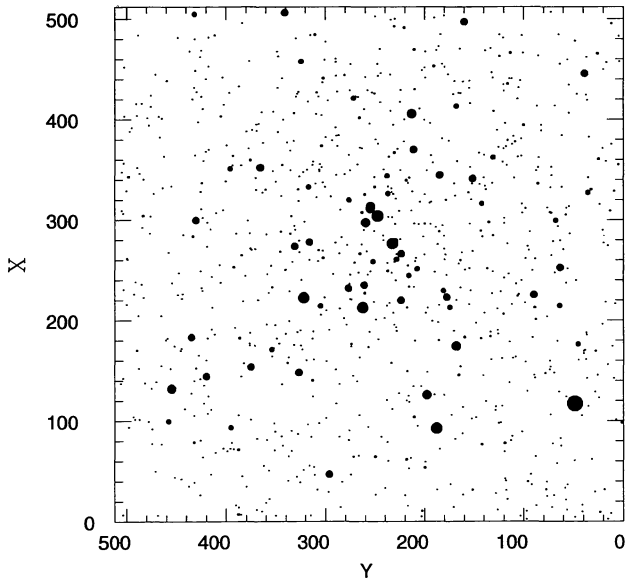

FIG. 37.—Map of NGC 436 generated from the list of stars appearing in the CMD. The scale is 0.″77 pixel^{-1}, giving a field of view of 6.′6. North is up, and east is to the left.

vertical to be satisfactorily fitted by such a young isochrone. A more reasonable fit to these stars is found with the 19 Myr isochrone (Fig. 36*a*). It is possible, therefore, to infer an age spread of ~12 Myr for the stars in NGC 457.

5.9. *NGC 436*

NGC 436 has recently been observed photoelectrically (*UBV*) by Huestamendia et al. (1991) (Table 5). A comparison of our photometry and that of Huestamendia et al. (1991) is given in Table 6. Earlier observations include photographic work by Alter (1944) and by Boden (1950). Becker & Stock (1958) studied the cluster in the *RGU* system.

The diagrams for NGC 436 are shown in Figures 37–39. A well-defined main sequence is observed in the cluster CMD (Fig. 38), extending far into the field star distribution, indicating that a large number of lower mass stars are present in the cluster. A very distinct binary sequence of stars is also visible. The fit of the SK82 MSTCC gives $E(B-V) = 0.50$ (Fig. 39*b*), in good agreement with that found by Huestamendia et al. (1991). The fit of the SK82 ZAMS gives $(m-M)_v = 14.10$ and $(m-M)_0 = 12.55$, corresponding to a distance of 3236 pc (Fig. 39*a*), considerably larger than that found by Huestamendia et al. (1991) (Table 5). Our CCD photometry reaches fainter magnitudes, and thus the fit of the ZAMS is more tightly constrained compared to the Huestamendia et al. fit to the more vertical portion of the ZAMS. Our derived age of 42 Myr (Fig. 39*a*) is also younger than the 63 Myr value found by Huestamendia et al. (1991).

5.10. *NGC 433*

NGC 433 has generally been ignored since the study by Alter (1944), who found the cluster to be at a distance of 4500 pc. This current study, and a recent investigation by Battinelli, Capuzzo-Dolceta, & Nesci (1992) (Table 5), provide a more reliable determination of the cluster distance and age, placing it much closer to the Sun.

The derived diagrams for NGC 433 are presented in Figures 40–45. The CMD (Fig. 41*a*) of the cluster is dominated by field stars, with little trace of a cluster. There are, however, two apparent sequences of late B-type stars in the two-color diagram of Figure 41*b*, reddened by two distinct amounts. To test

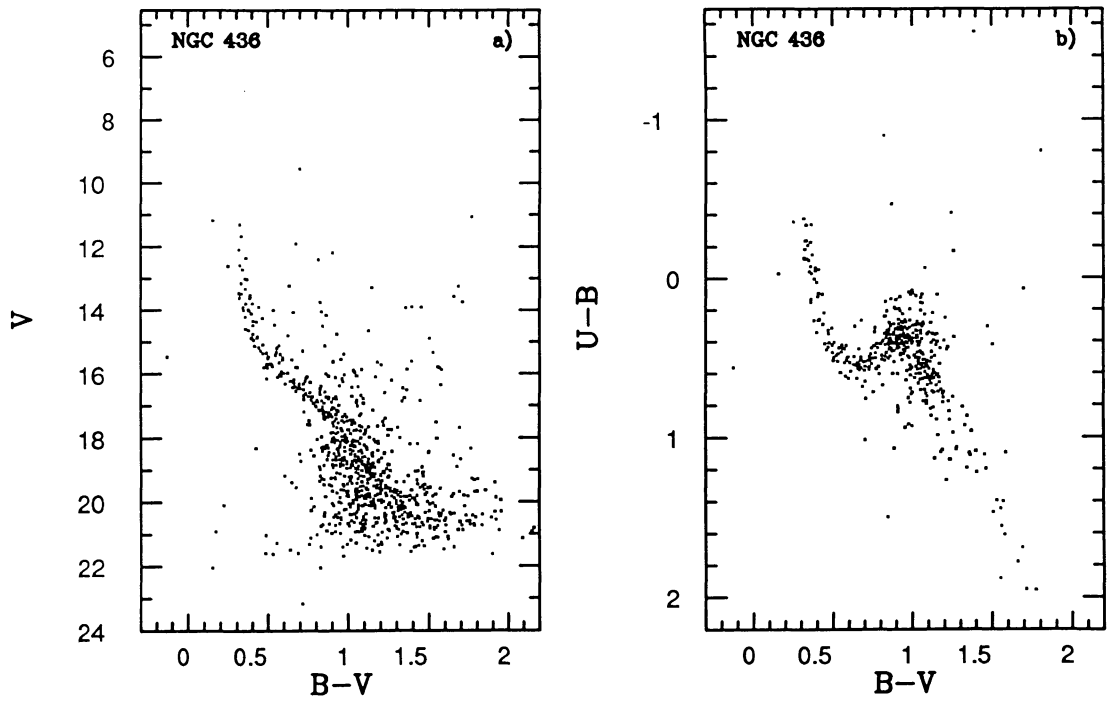

FIG. 38.—(*a*) Color-magnitude diagram for NGC 436. (*b*) Two-color diagram for NGC 436.

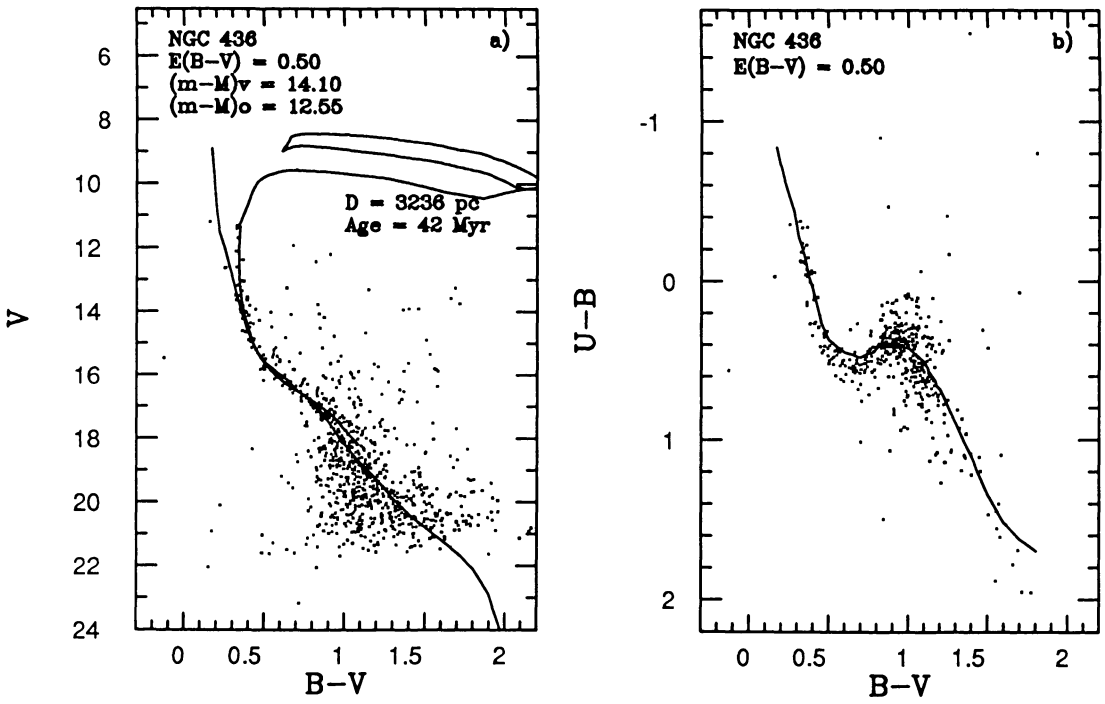

FIG. 39.—(*a*) Fit of the Schmidt-Kaler (1982) ZAMS and 42 Myr isochrone of Maeder & Meynet (1991) to NGC 436. (*b*) Fit of the Schmidt-Kaler (1982) main-sequence two-color curve to NGC 436.

this conclusion, an individual dereddening analysis of the stars within the enclosed region of Figure 42*a* was performed.

The results of the individual dereddening analysis are shown in the histogram of Figure 42*b*. The distribution is bimodal, with peaks at $E(B-V) = 0.64$ and $E(B-V) = 0.86$. The locations of those stars with $E(B-V) > 0.75$ are plotted in Figure 43*a*, while Figure 43*b* shows the locations of stars with $E(B-V) < 0.75$. The reddening across the region is highly nonuniform, with the higher reddening occurring to the north. Leisawitz et al. (1989) observed NGC 433 in ^{12}CO and found molecular clouds along the line of sight to NGC 433, with the molecular clouds located toward the north of the cluster and extending to the cluster center (see their Fig. 44). This is entirely consistent with Figure 43, showing patchy reddening across the smaller observed field, with the majority of the higher obscuration occurring toward the north.

A definite clustering of stars is seen in Figure 43*a;* since the clustering occurs in the region where the highest obscuration is found, it must be genuine and not the result of higher extinction elsewhere in the field. The reddening to NGC 433 was estimated by Battinelli et al. (1992), on the basis of spectra and low-precision BV photometry to be $E(B-V) = 0.82$. The stars in Figure 43*a* have reddening values that peak at $E(B-V) = 0.86$ (Fig. 42*b*), in good agreement with the value found by Battinelli et al. (1992).

The reddening-free CMD for those stars with $E(B-V) > 0.75$ is shown in Figure 44*a*. The locations of most of the stars in this CMD are consistent with being members of the cluster, although highly reddened by the intervening cloud. The stars indicated by a cross are likely field stars, at a greater distance, which are also reddened by the intervening cloud. The 79 Myr MM91 isochrone (Fig. 44*b*) shifted by $(m-M)_0 = 11.83$ ($D =$ 2323 pc) fits the distribution of stars quite well and also fits the distribution of stars in the full CMD of Figure 45. Battinelli et al. (1992) find a maximum age of 170 Myr based upon the presence of a B5 main-sequence star at the turnoff point and a distance of 2100 pc ± 100 pc, both of which are consistent with this study.

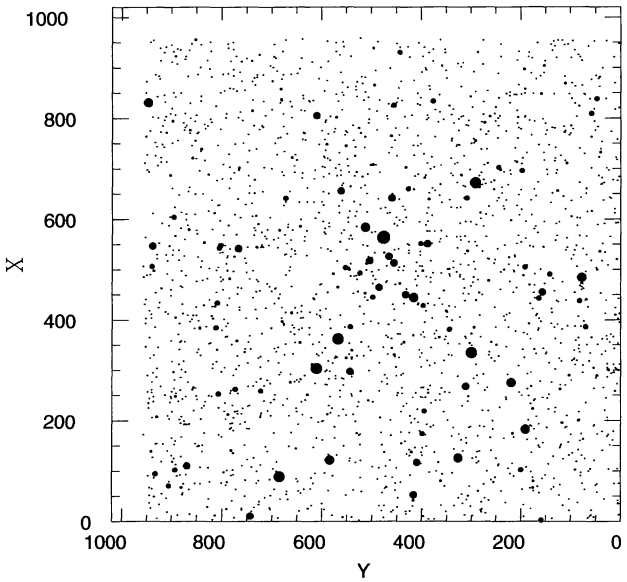

FIG. 40.—Map of NGC 433 generated from the list of stars appearing in the CMD. The scale is 0.″68 pixel^{-1}, giving a field of view of 11.′6. North is up, and east is to the left.

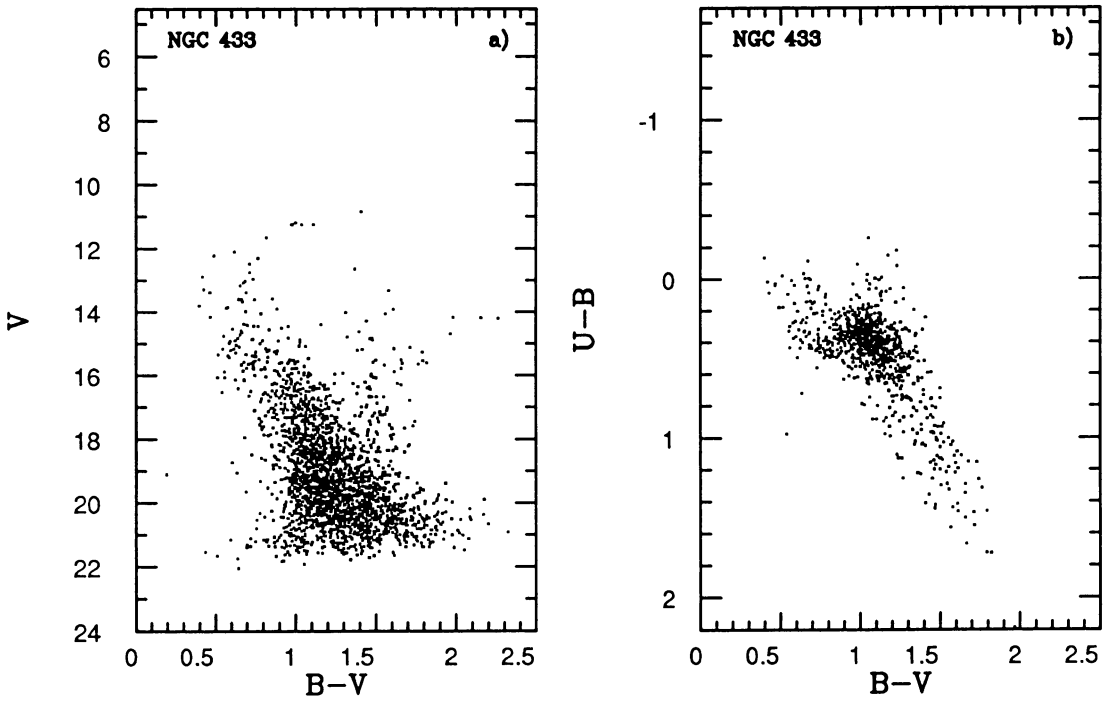

FIG. 41.—(*a*) Color-magnitude diagram for NGC 433. (*b*) Two-color diagram for NGC 433.

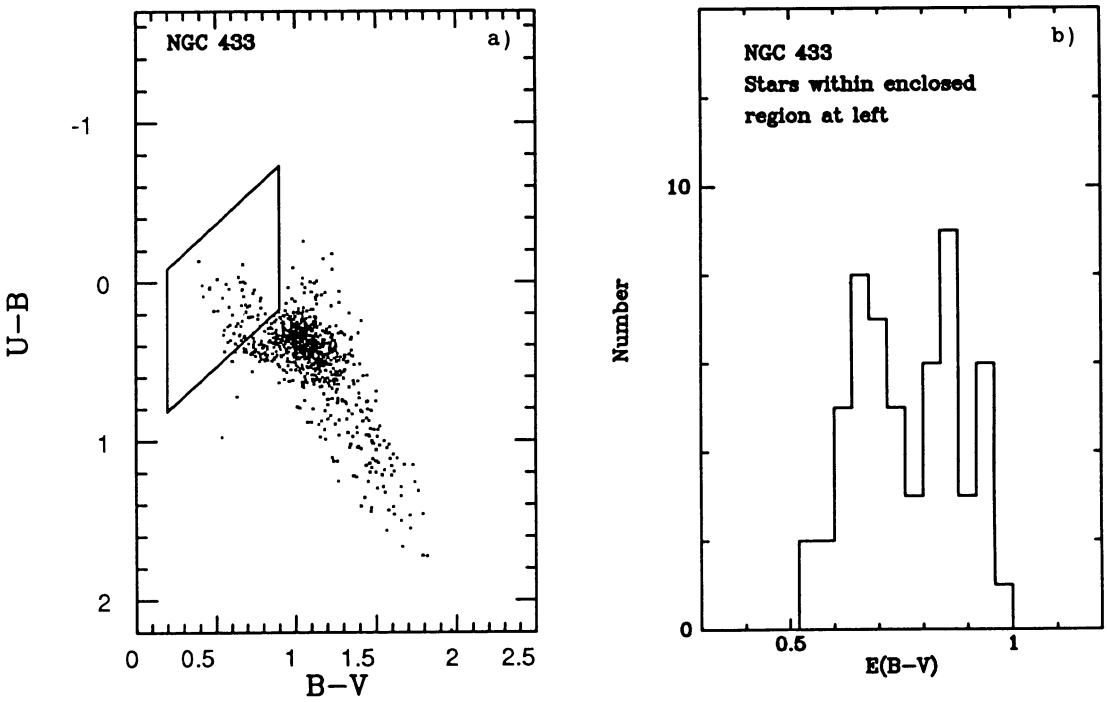

FIG. 42.—(*a*) Subset of stars used in the analysis of NGC 433. (*b*) Histogram of individual reddening values from the subset shown in (*a*). A bimodal distribution of reddening is apparent.

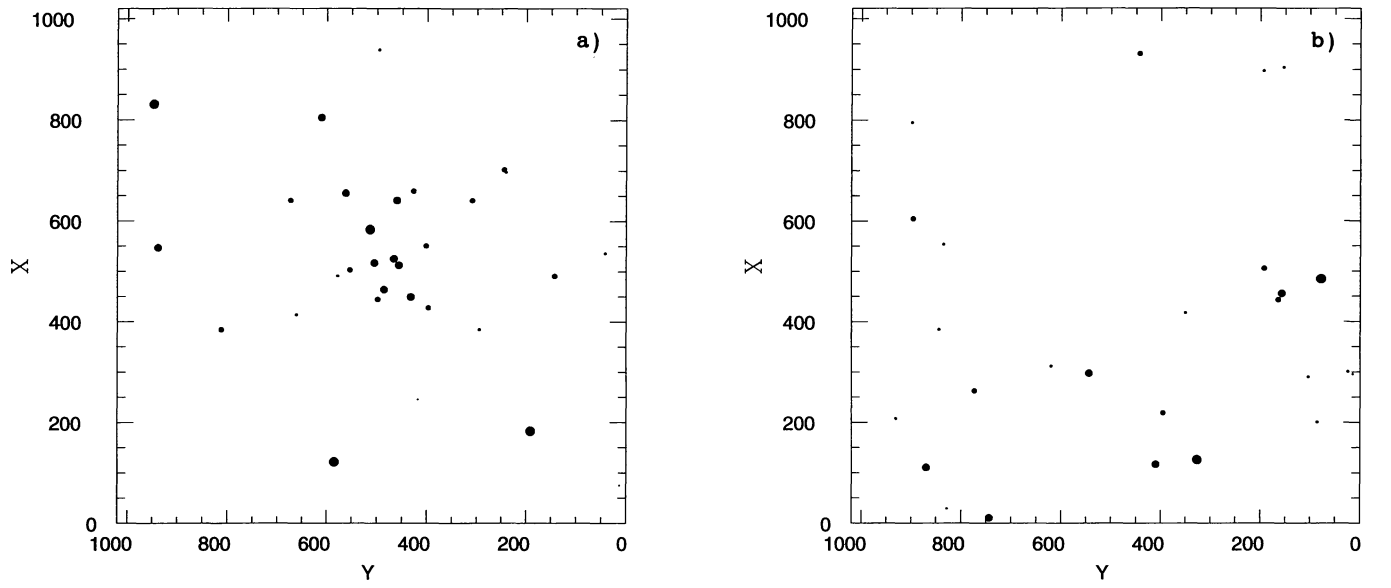

FIG. 43.—(*a*) Spatial positions of stars within the region of Fig. 42*a* with $E(B-V) > 0.75$. (*b*) Spatial positions of stars within the region of Fig. 42*a* with $E(B-V) < 0.75$.

The derived radii and net number of cluster stars (Table 4) are surely affected by the patchy reddening. Alter (1944) found a full radius of 3'.4, while Battinelli et al. (1992) found a radius of 1'.8. From the cumulative distribution the net number of cluster stars is estimated to be 82 ± 9. The large reddening in the region of the cluster means that the number of cluster stars is likely to be greater than this number, since many of the cluster stars will be more obscured. This result contrasts with that of Battinelli et al. (1992), who inferred that the cluster contained few stars.

5.11. *NGC 381*

Crinklaw & Talbert (1988) have studied NGC 381 in the *UBV* system (Table 5). A comparison of their photometry with ours is shown in Table 6. Our derived diagrams for the cluster are shown in Figures 46–49.

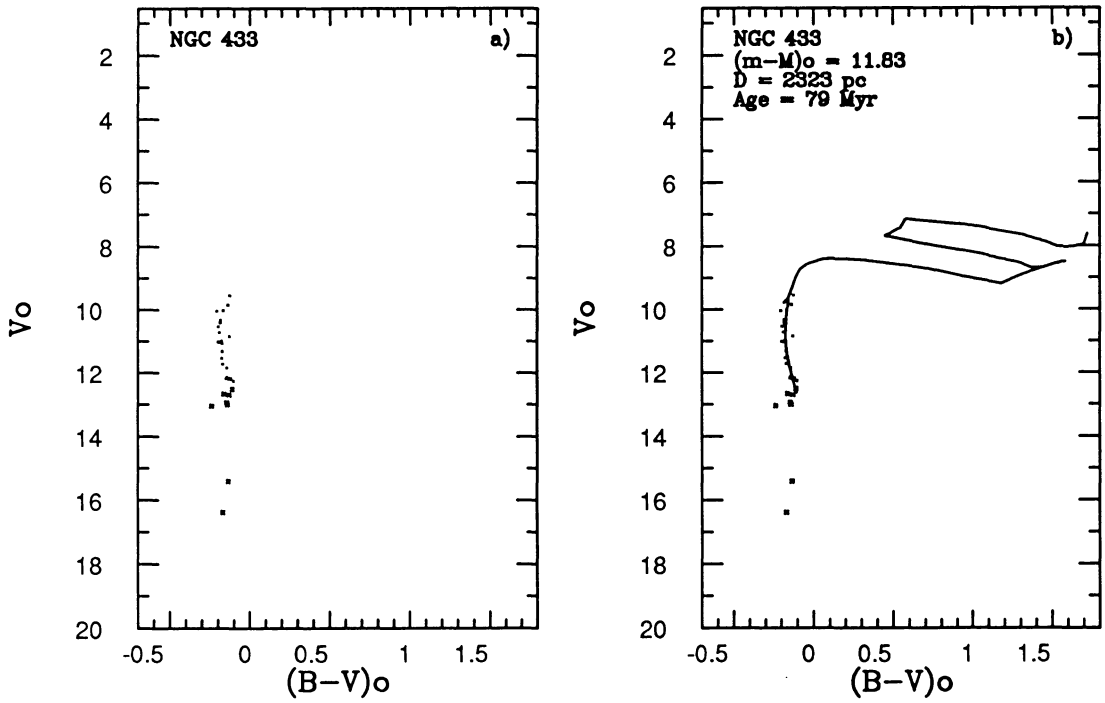

FIG. 44.—(*a*) Reddening-corrected CMD of stars in Fig. 43*a* with $E(B-V) > 0.75$. (*b*) Fit of the 79 Myr isochrone to the reddening-corrected CMD. Crosses indicate stars which are not likely cluster members.

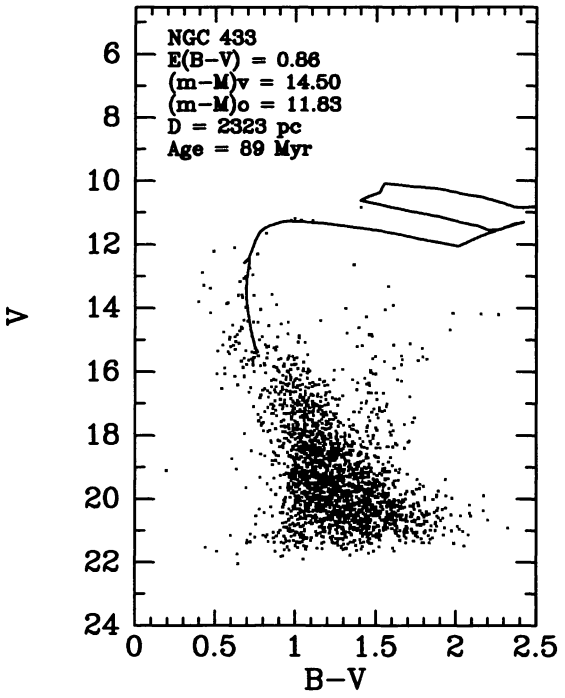

FIG. 45.—Fit of the 89 Myr Maeder & Meynet (1991) isochrone to the full CMD of NGC 433.

The CMD of Figure 47*a* reveals a sequence of stars at brighter magnitudes which presumably represents the cluster. Stars in this group with $V < 16$ and $(B - V) < 1$ have been isolated to determine the reddening. A clear cluster sequence is seen in the two-color diagram of Figure 48*a*. A fit of the SK82 MSTCC to these stars gives a reddening of $E(B - V) = 0.36$ (Fig. 48*b*), in good agreement with the value of 0.35 determined by Crinklaw & Talbert (1988).

Using $E(B - V) = 0.36$, distance moduli of $(m - M)_v = 11.25$ and $(m - M)_0 = 10.13$ (1062 pc) are found for the cluster (Fig. 49), in good agreement with the value of 950 pc determined by Crinklaw & Talbert (1988). A fit of the 1.1 Gyr MM91 isochrone is also shown in Figure 49. While membership of the stars for which the evolved part of the isochrone is fitted is uncertain, the apparent turnoff and the fact that the earliest type star in the two-color diagram of Figure 48*b* is roughly A0 are consistent with this age determination.

These results support the Crinklaw & Talbert (1988) determination of a closer distance of NGC 381 to the Sun than the other clusters in this study. This cluster, therefore, is not likely associated with the complex of young clusters in the Perseus arm.

5.12. *NGC 366*

To the best of our knowledge, this is the first photometric study of NGC 366. A map of the cluster region is shown in Figure 50 and shows a compact grouping of stars. However, the resulting CMD and two-color diagram for the cluster (Figs. 51*a* and 51*b*, respectively) show large scatter about both of the principal sequences.

In order to better determine the cluster radius, only those stars with $V < 19$ and $(B - V) < 1.3$ were selected. The spatial distribution of these stars is shown in Figure 52. A definite clustering is evident, indicating that the majority of them are likely associated with the cluster.

Since a considerable variation in the reddening is present, stars out to 2'.38 from the cluster center were individually dereddened, with a resulting mean $E(B - V)$ of 1.37 ($\sigma_{E(B-V)} = 0.18$). The reddening-corrected CMD is shown in Figure 53*a*, along with the SK82 ZAMS shifted to $(m - M)_0 = 12.50$, or a distance of 3163 pc (Fig. 53*b*). The 6 Myr MM91 isochrone is also shown, indicating that NGC 366 is quite young. The cluster is likely still associated with the molecular material from which it formed, since the reddening is so large and variable.

5.13. *Berkeley 62*

Berkeley 62 (Be 62) has previously been studied by Forbes (1981), using photoelectric *UBV* photometry of 14 stars (Table 5). Forbes's age estimate of 10 Myr was based upon an earliest spectral type of B1 in the cluster. A comparison of the Forbes (1981) and our photometry is given in Table 6. For those stars which were saturated in the CCD frames, the values of Forbes (1981) were used, corrected by the amounts given in Table 6.

Figures 54–56 present our derived diagrams for Be 62. A distinct lower edge to the main sequence is visible in the CMD (Fig. 55*a*), indicating that the overall reddening to the cluster is relatively uniform, despite the scatter in the upper end of the CMD. A fit of the SK82 MSTCC (Fig. 56*b*) indicates a reddening to the cluster of $E(B - V) = 0.82$. The reddening is consistent with that found by Forbes (1981) (Table 5) and with the fit in the CMD of Figure 56*a*. The distance moduli are found to be $(m - M)_v = 14.70$ and $(m - M)_0 = 12.16$ (2704 pc), considerably larger than the distance, based upon observations of only 14 stars, as determined by Forbes (1981). The derived

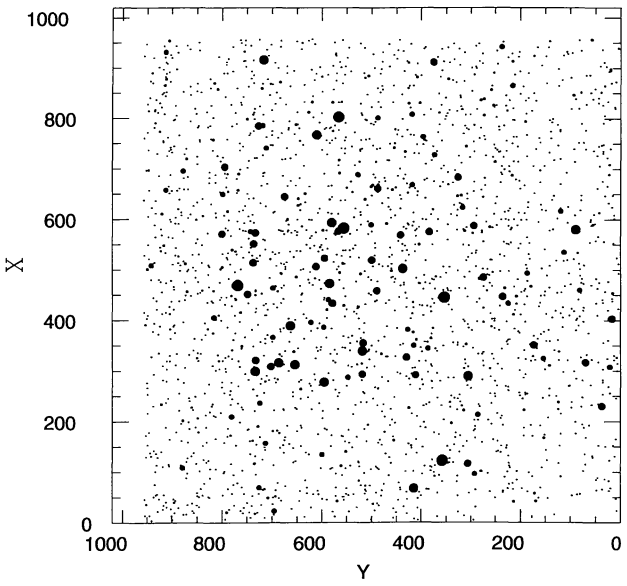

FIG. 46.—Map of NGC 381 generated from the list of stars appearing in the CMD. The scale is 0".68 pixel^{-1}, giving a field of view of 11'.6. North is up, and east is to the left.

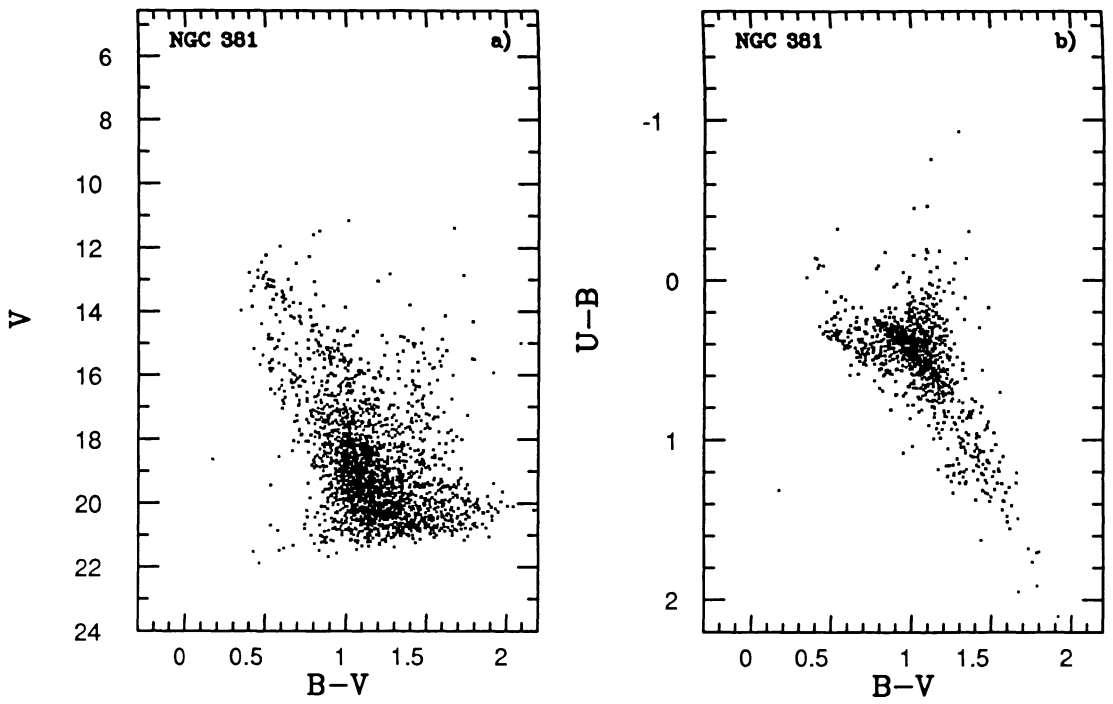

FIG. 47.—(*a*) Color-magnitude diagram for NGC 381. (*b*) Two-color diagram for NGC 381.

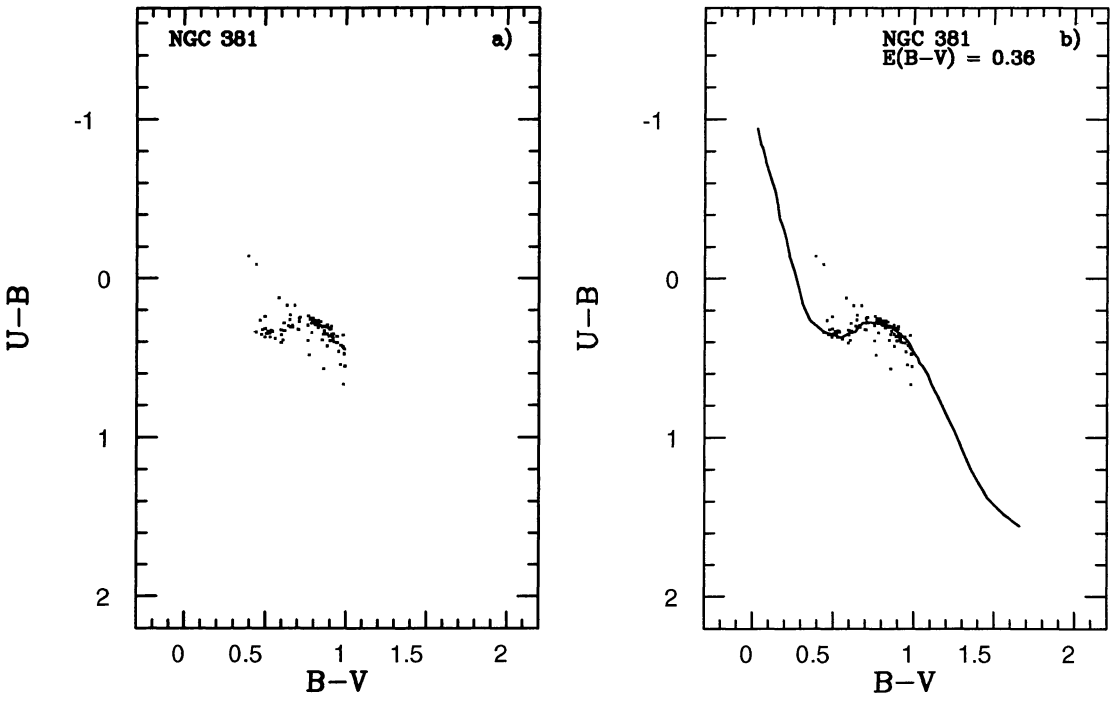

FIG. 48.—(*a*) Two-color diagram for stars in NGC 381 with $V < 16$ and $(B - V) < 1$. (*b*) Fit of the Schmidt-Kaler (1982) main-sequence two-color curve to the stars in (*a*).

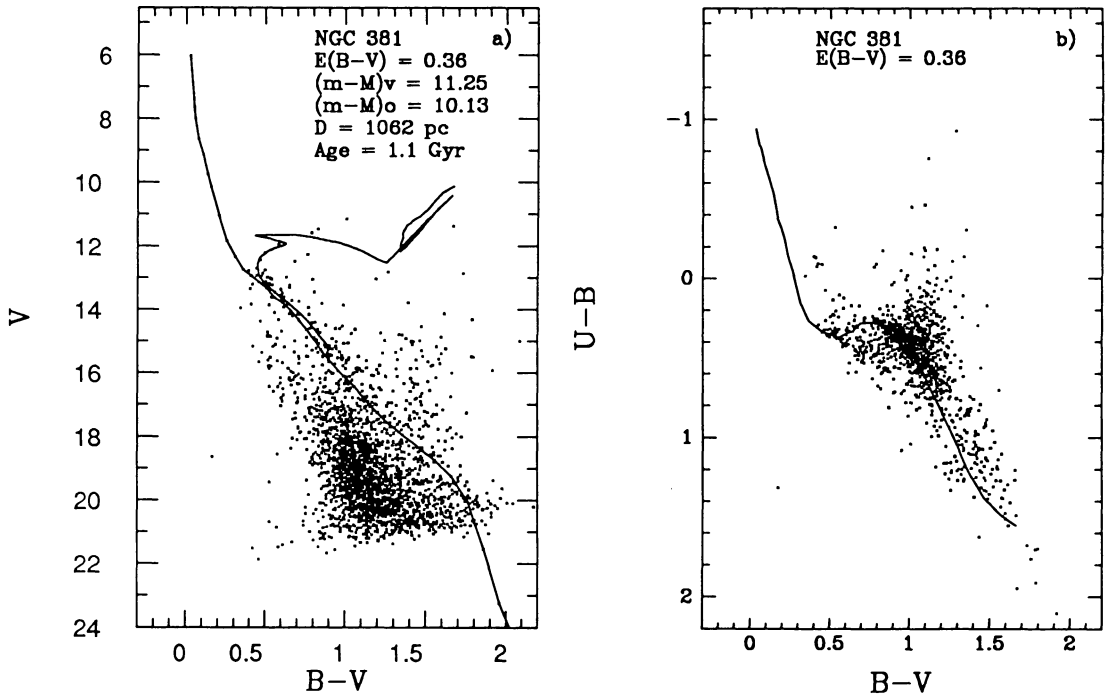

FIG. 49.—Fit of the Schmidt-Kaler (1982) ZAMS and 1.1 Gyr isochrone of Maeder & Meynet (1991) to the complete sample of stars for NGC 381.

age for Be 62 of 10 Myr (Fig. 56*a*) is the same as that found by Forbes (1981).

5.14. *Cz 2*

The approach of twilight limited the observations of the region cataloged as Cz 2 to *B* and *V* images. The map of the region observed, based upon the photometry, is shown in Figure 57, while the CMD is shown in Figure 58. Stars with $V < 13$ were omitted from the CMD due to saturation of the CCD. While several of these bright stars are missing from the CMD, the remaining stars do not suggest a distinct cluster. The assignment of a cluster in the region is doubtful, and therefore Cz 2 is excluded from further consideration as a cluster.

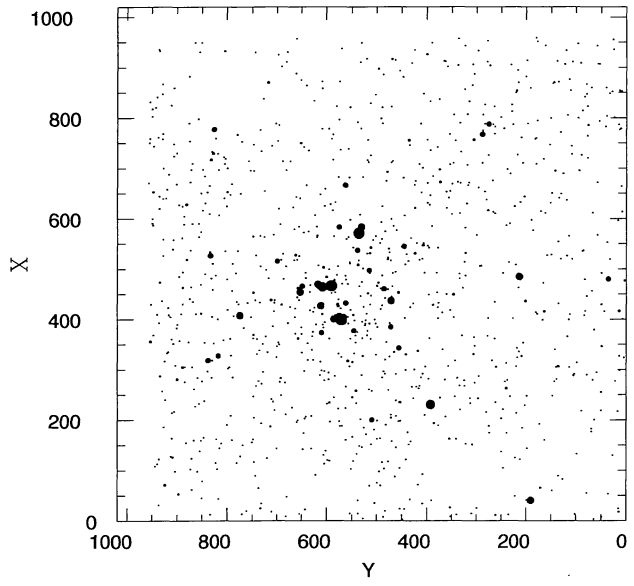

FIG. 50.—Map of NGC 366 generated from the list of stars appearing in the CMD. The scale is 0.″68 pixel^{-1}, giving a field of view of 11.′6. North is up, and east is to the left.

5.15. *Stock 24*

Balasz (1961) obtained *RGU* photometry for Stock 24 (St 24). As in the case of Cz 2, we obtained only *B* and *V* frames for this cluster, in the region shown in Figure 59. The CMD is shown in Figure 60, where a reasonably well-defined main sequence is apparent, but with scatter in the brighter portion of the CMD.

Since no determination of the reddening that *U*-band photometry would have provided was available, only those stars within $R_{\rm full}$ (Table 4) were selected for further analysis to minimize contamination from field stars. The CMD for this subset of stars is shown in Figure 61*a*. Because the photometry reaches the bend in the main sequence, and because there is a well-defined lower edge to the apparent main sequence, the fit to the ZAMS is quite constrained, and a reasonable estimate of the reddening is possible, despite the lack of *U*-band photometry. The SK82 ZAMS can be shifted in both axes until a satisfactory fit to the shape of the observed main sequence is found, provided that the cluster is young enough that stellar evolution has not altered the shape substantially. As can be seen in Figure 61*b*, the estimated reddening is $E(B-V) = 0.50$, although the estimate is uncertain because the cluster appears to be moderately old (120 Myr) based upon the fit of the MM91 isochrone (Fig. 61*b*). The fit to the SK82 ZAMS results in $(m-M)_v = 13.80$ and $(m-M)_0 = 12.25$ (2818 pc).

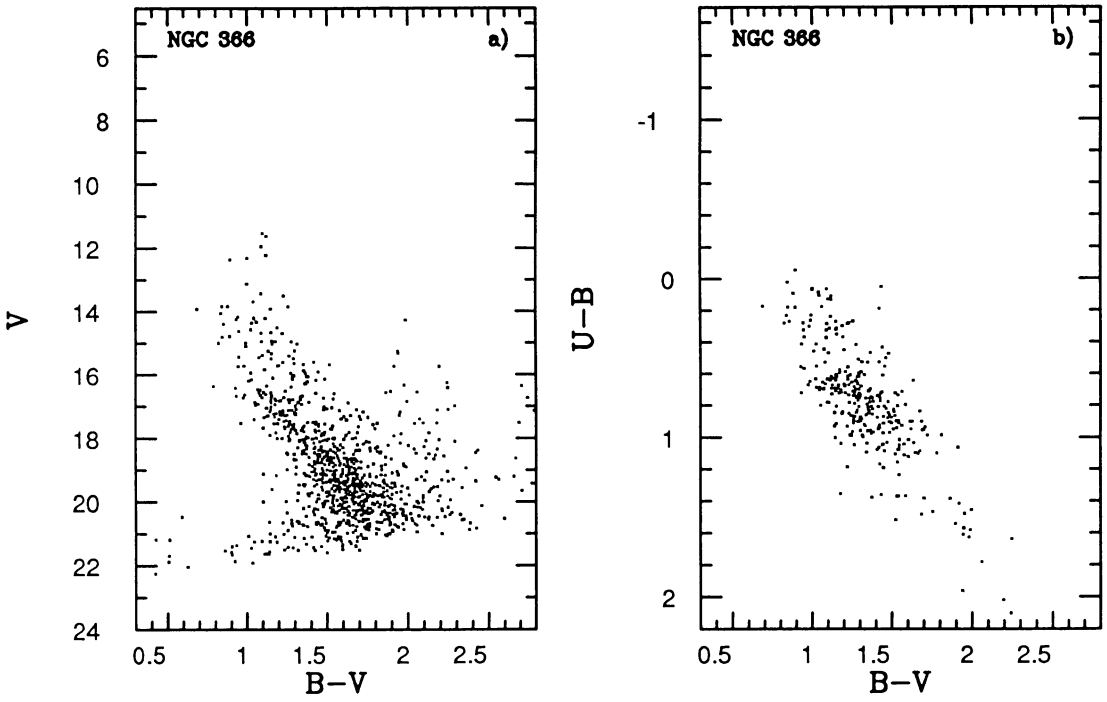

FIG. 51.—(*a*) Color-magnitude diagram for NGC 366. (*b*) Two-color diagram for NGC 366.

5.16. *NGC 146*

Previous studies of NGC 146 include the *RGU* study by Hardorp (1960) and the *UBV* photographic study by Jasevicius (1964). NGC 146 was observed during photometric conditions, on the same night as Be 60, Be 58, and Be 1 (see below). Exposure times for these clusters were shorter than for other program clusters in order to increase the number of clusters for an investigation of the large-scale sequence of cluster formation. The photometry, therefore, does not reach as faint as for other program clusters.

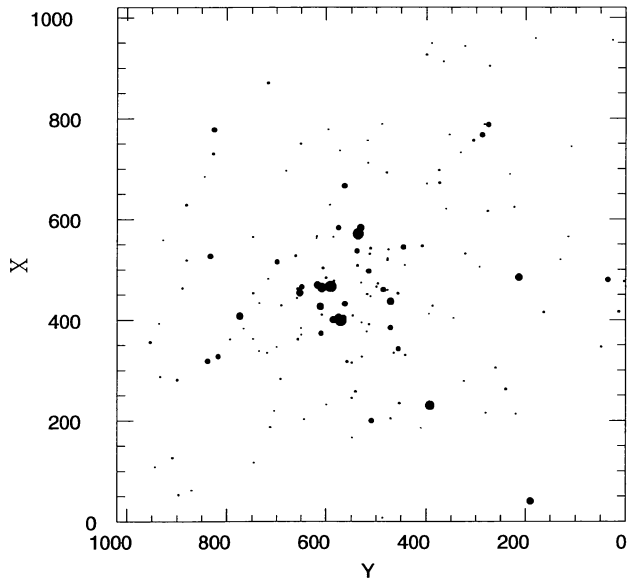

FIG. 52.—Spatial locations for stars in NGC 366 with $V < 19$ and $(B - V) < 1.3$.

Figure 62 shows the observed field of NGC 146. The CMD and two-color diagrams (Fig. 63) reveal a populous cluster with a main sequence widened by variable reddening. An individual dereddening analysis was therefore conducted for stars with $(B - V) < 0.70$. A mean reddening of $E(B - V) = 0.70$ was found. The reddening-corrected CMD is shown in Figure 64*a*. A fit to the SK82 ZAMS gives $(m - M)_0 = 13.40$, or a distance of 4786 pc (Fig. 64*b*). This is substantially larger than the 3370 pc distance attributed to the cluster by Kimeswenger & Weinberger (1989), but it reinforces their assertion that there is a spiral arm beyond the Perseus arm. The 10 Myr MM91 isochrone is also shown, indicating that NGC 146 is less than 10 Myr old. At the top of the main sequence is a star whose $(B - V)_0$ color is that of O7–O8 stars, which have main-sequence lifetimes of 3–6 Myr (Maeder & Meynet 1988).

5.17. *King 15*

To our knowledge, no published photometric studies of King 15 exist. A map of the observed field, based upon the CCD photometry, is shown in Figure 65, and the CMD for King 15 is shown in Figure 66*a*. There is a strikingly sharp lower edge to the stellar distribution in the CMD, suggesting that the overall reddening toward the cluster is uniform. The substantial scatter in the upper portion of the CMD may indicate variable reddening, or may simply be caused by field stars contaminating the diagram. Since the CMDs of other clusters in this region have a similar appearance, the scatter in the upper end of the CMD is probably the result of a population of moderately young stars within the Perseus spiral arm.

U-band photometry was not obtained, so it is necessary to

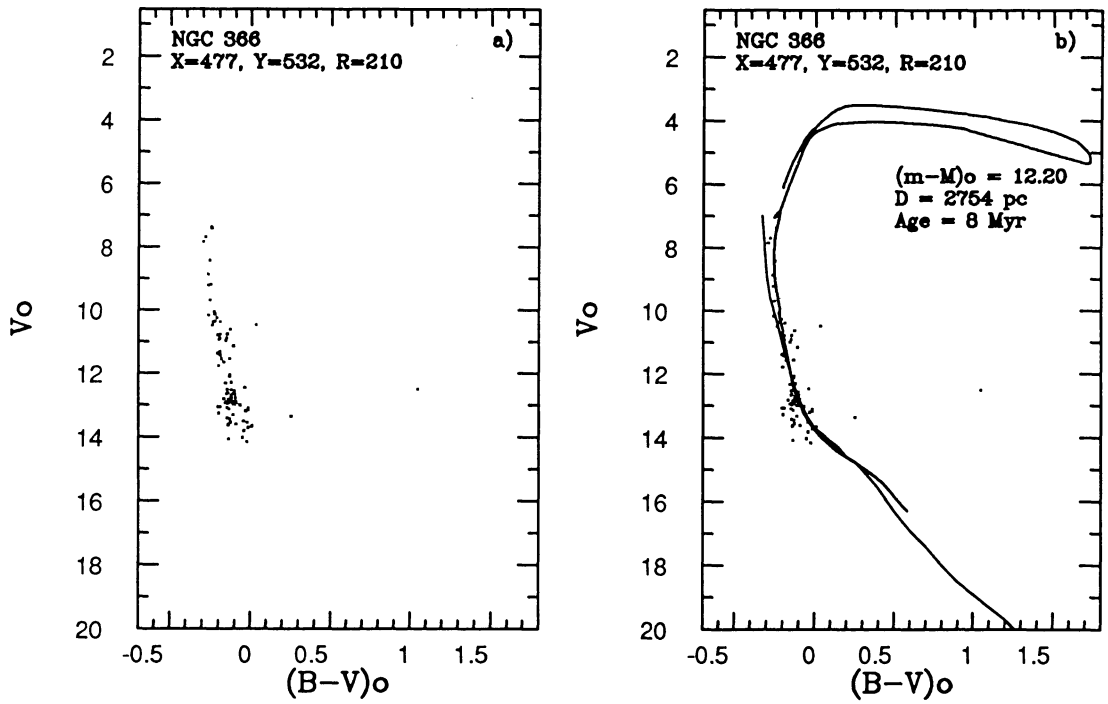

FIG. 53.—(*a*) Reddening-corrected CMD for stars in Fig. 52. (*b*) Fit of the Schmidt-Kaler (1982) ZAMS and 6 Myr isochrone of Maeder & Meynet (1991) to reddening-corrected CMD.

rely on a fit of the ZAMS to the CMD for an estimate of the reddening. The SK82 ZAMS (Fig. 66*b*) was matched to the sharp lower edge of the stellar distribution, rather than the stars at the upper mass end of the CMD. This results in derived values of $E(B-V) = 0.46$, $(m-M)_v = 13.72$, and $(m-M)_0 = 12.29$, or a distance of 2871 pc. The age is ambiguous because of the uncertainty in cluster membership at the higher mass end of the CMD, but with the chosen fit of the ZAMS it appears that the cluster is considerably older than the other clusters in this survey. The earliest spectral type star on the shifted ZAMS has $V \sim 16$ and $(B-V) \sim 0.65$, corresponding to $M_v = 2.3$ and $(B-V)_0 = 0.19$. Based upon the SK82 colors, this corresponds to an A7 star with a mass of $\sim 1.5\ M_\odot$ and a main-sequence lifetime of ~ 3 Gyr (Fig. 1 of Maeder & Meynet 1988). A more accurate age determination is difficult because of the confusion at the upper end of the main sequence.

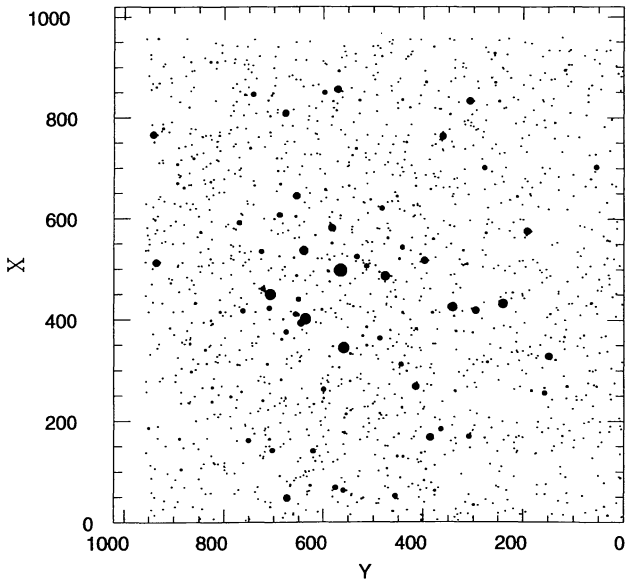

FIG. 54.—Map of Be 62 generated from the list of stars appearing in the CMD. The scale is 0.″68 pixel^{-1}, giving a field of view of 11.′6. North is up, and east is to the left.

5.18. *NGC 129*

NGC 129 is an important cluster because it contains the Cepheid variable DL Cas. Among the *UBV* studies are those of Arp, Sandage, & Stephens (1959), Turner, Forbes, & Pedreros (1992), and a four-color and Hβ study by Schmidt (1980) (Table 5). Schmidt (1980) compared the photometric values of Hoag et al. (1961) and Arp et al. (1959) and found that the Hoag et al. color excesses are larger than the Arp et al. values by 0.04 mag. Using the Crawford (1975) relation between $E(b-y)$ and $E(B-V)$, Schmidt finds that his color excesses are 0.08 mag larger than the Arp et al. values and 0.03 mag larger than the Hoag et al. values. The Turner et al. (1992) photometry agrees quite well with the Hoag et al. (1961) values, showing only a 0.01 mag difference in V, but shows a somewhat larger 0.03 mag difference with the $(B-V)$ values of Arp et al., with no difference in V.

Our CCD observations of NGC 129 were obtained during nonphotometric conditions and thus require the use of local standards for calibration. Because of the suggestion by

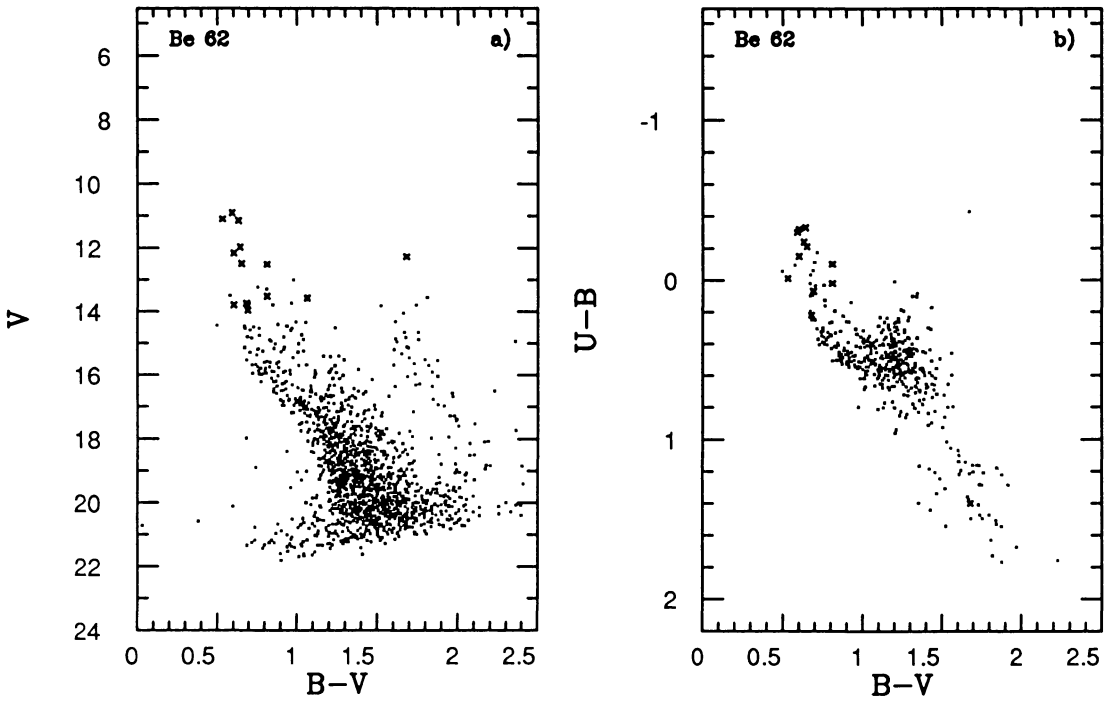

FIG. 55.—(*a*) Color-magnitude diagram for Be 62. (*b*) Two-color diagram for Be 62.

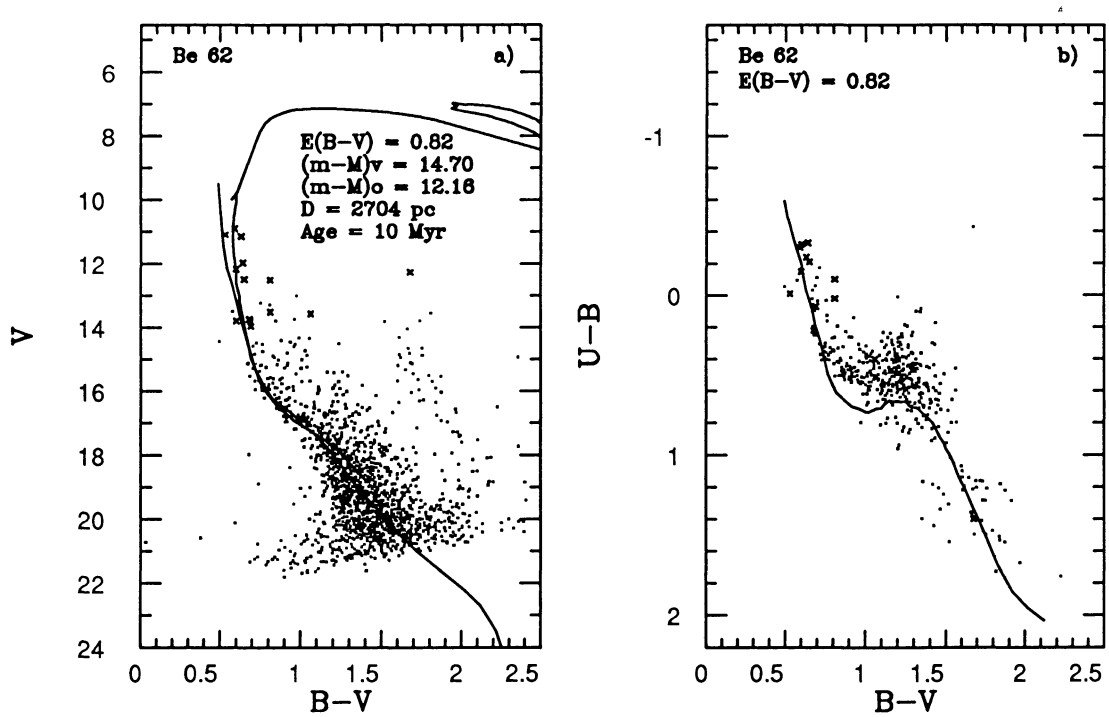

FIG. 56.—(*a*) Fit of the Schmidt-Kaler (1982) ZAMS and 10 Myr isochrone of Maeder & Meynet (1991) to Be 62. (*b*) Fit of the Schmidt-Kaler (1982) main-sequence two-color curve to Be 62.

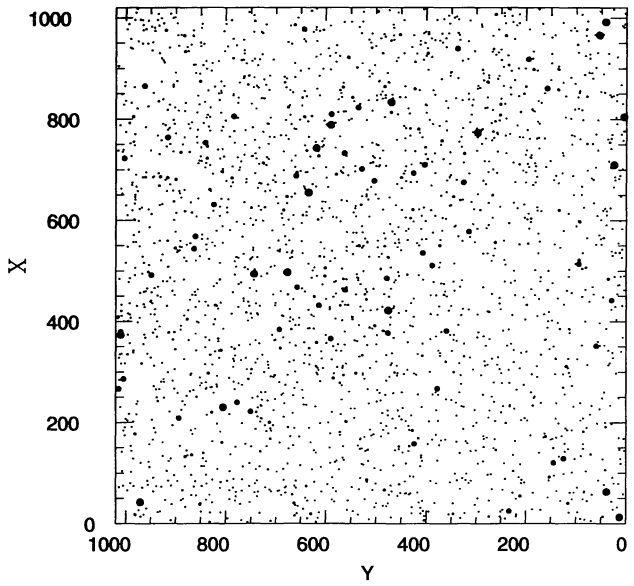

FIG. 57.—Map of Cz 2 generated from the list of stars appearing in the CMD. The scale is 0".68 pixel^{-1}, giving a field of view of 11'.6. North is up, and east is to the left.

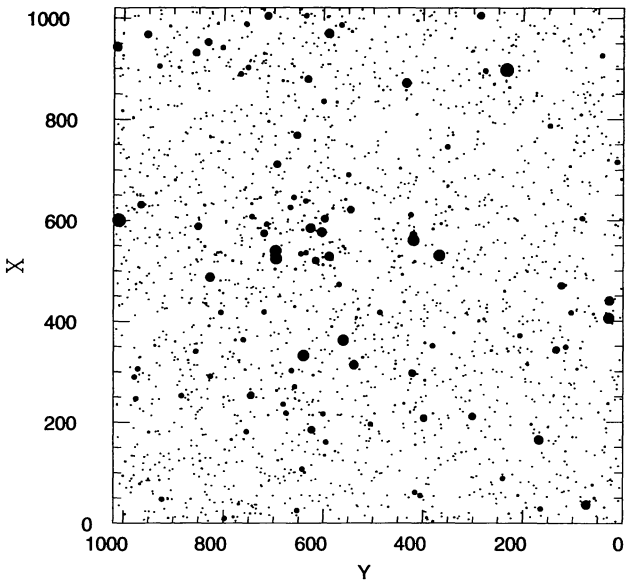

FIG. 59.—Map of St 24 generated from the list of stars appearing in the CMD. The scale is 0".68 pixel^{-1}, giving a field of view of 11'.6. North is up, and east is to the left.

Schmidt (1980) that the Hoag et al. values for U, B, and V are closer to the UBV system than those of Arp et al., the Hoag et al. photoelectric values were used as local standards. The subsequent study by Turner et al. (1992) agrees quite well with the Hoag et al. photometry, indicating that the photometry is reliable. The residuals from the fit to the Hoag et al. local standards were 0.03 mag in V and $(B-V)$ and 0.04 mag in $(U-B)$ and are shown in Figure 67.

The observed cluster field is shown in the map of Figure 68, and the CMD and two-color diagram are shown in Figure 69. The brightest stars ($V<11$) were saturated in the CCD frames, so the Hoag et al. (1961) values were used for them. For the classical Cepheid DL Cas, the mean photometric values $[\langle V\rangle = 8.97, \langle (B-V)\rangle = 1.24, \langle (U-B)\rangle = 0.87]$ of Arp et al. (1959) were used. The position of DL Cas in Figure 69 is indicated by the open square.

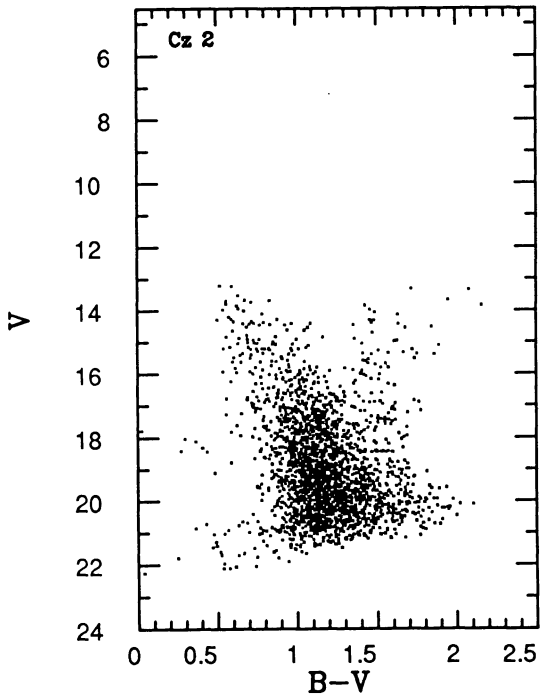

FIG. 58.— Color-magnitude diagram for Cz 2

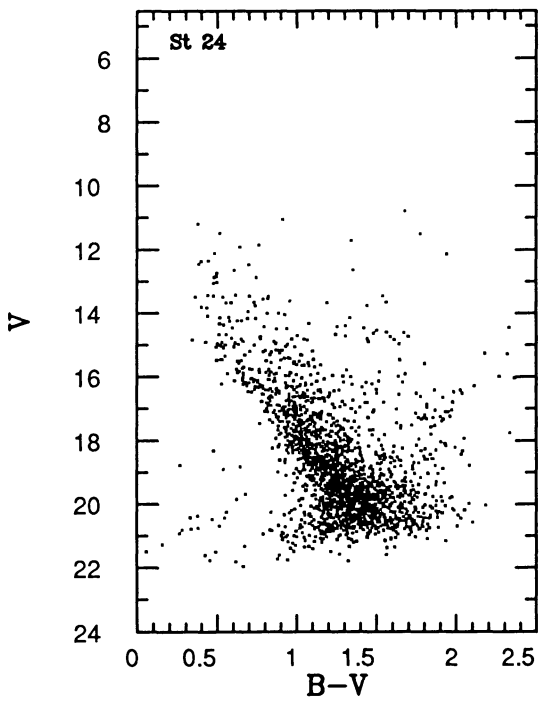

FIG. 60.—Color-magnitude diagram for St 24

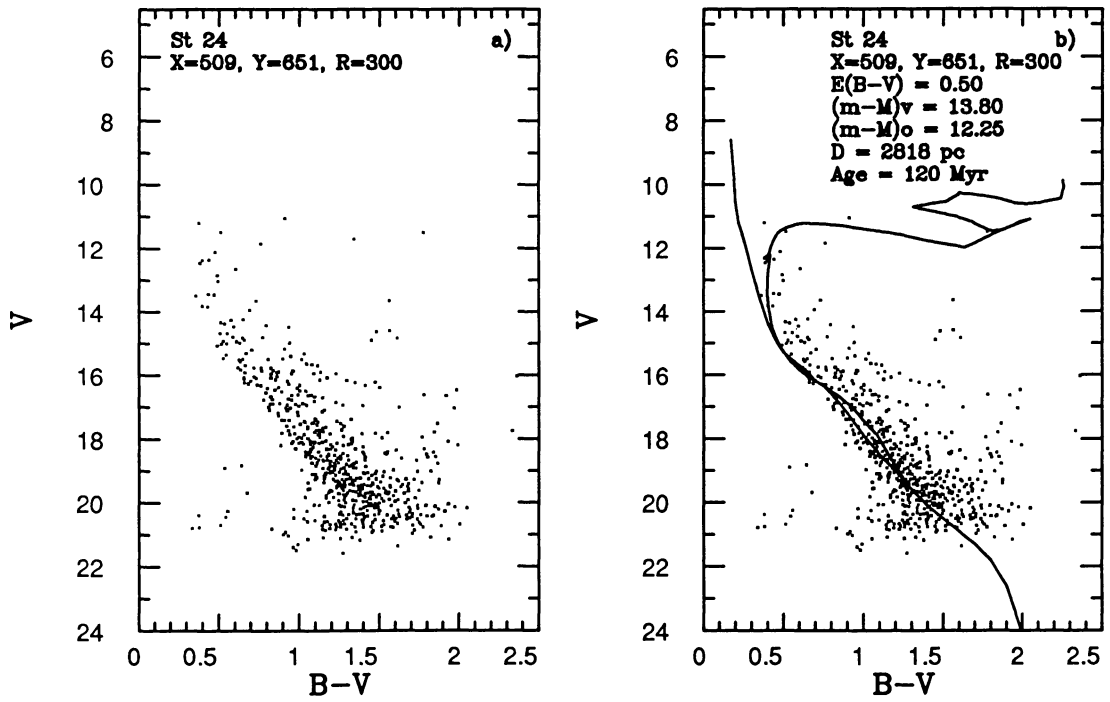

FIG. 61.—(*a*) Color-magnitude diagram for stars within R_{full} of the center of St 24. (*b*) Fit of the Schmidt-Kaler (1982) ZAMS and 120 Myr isochrone of Maeder & Meynet (1991) to St 24.

An individual dereddening analysis on the stars with $(B - V) < 0.70$ was used to define the reddening to the cluster, and a mean reddening of $E(B - V) = 0.57$ was found. A fit of the SK82 ZAMS to the reddening-corrected CMD is shown in Figure 70, giving $(m - M)_v = 12.97$ and $(m - M)_0 = 11.20$, or a distance of 1738 pc for the cluster. The fit of the MM91 isochrone for 50 Myr is also shown. Figure 71 shows the fit of the ZAMS, MSTCC, and isochrone to the full set of data. The 50 Myr isochrone indicates that the Cepheid is on the first crossing track, rather than at the end of the blue loop where it spends a greater time in its evolution. The older isochrone, of ~74 Myr, which would place the Cepheid at the end of the blue loop, is unable to fit satisfactorily the stars near $V \sim 9$, $(B - V) \sim 0.45$. We have elected to use the 50 Myr age estimate, although an age of ~74 Myr cannot be ruled out without further information on the membership of the brighter stars near the main-sequence turnoff.

Based upon radial velocity data, Mermilliod, Mayor, & Burki (1987) concluded that DL Cas is a probable member of NGC 129, a fact which our photometric distance and age determination for NGC 129 tends to support. Star 2 of Hoag et al. (1961) [$V \sim 8.6$, $(B - V) \sim 2.0$] is listed as a nonmember by Mermilliod et al. (1987).

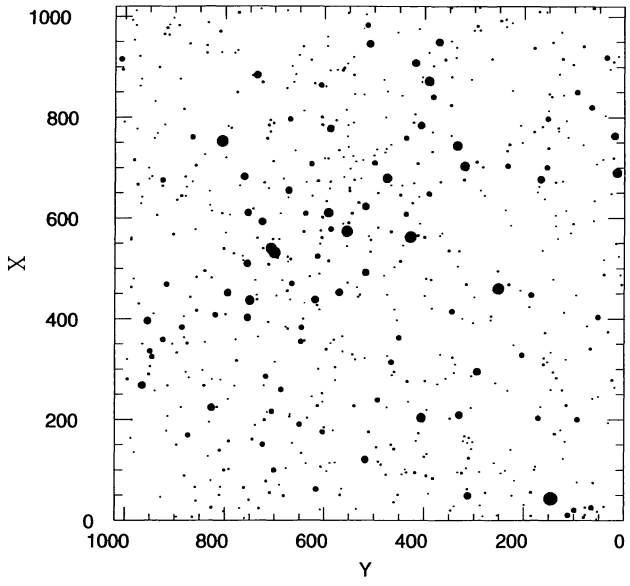

FIG. 62.—Map of NGC 146 generated from the list of stars appearing in the CMD. The scale is 0.″68 pixel^{-1}, giving a field of view of 11.′6. North is up, and east is to the left.

5.19. *NGC 103*

NGC 103 has been studied photometrically only once, by Hardorp (1960) (Table 5). The region observed in this study is shown in Figure 72, while the CMD and two-color diagram are shown in Figure 73. These diagrams indicate that NGC 103 is a populous cluster, with a well-defined main sequence.

Since the CCD frame covers the cluster as defined by R_{full}, only those stars within R_{full} (Table 4) were used to determine the cluster parameters, thus minimizing contamination from field stars. The CMD and two-color diagram for these stars are shown in Figure 74. The CMD and two-color diagram highlight the definition of the main sequence and the lack of an observed binary sequence.

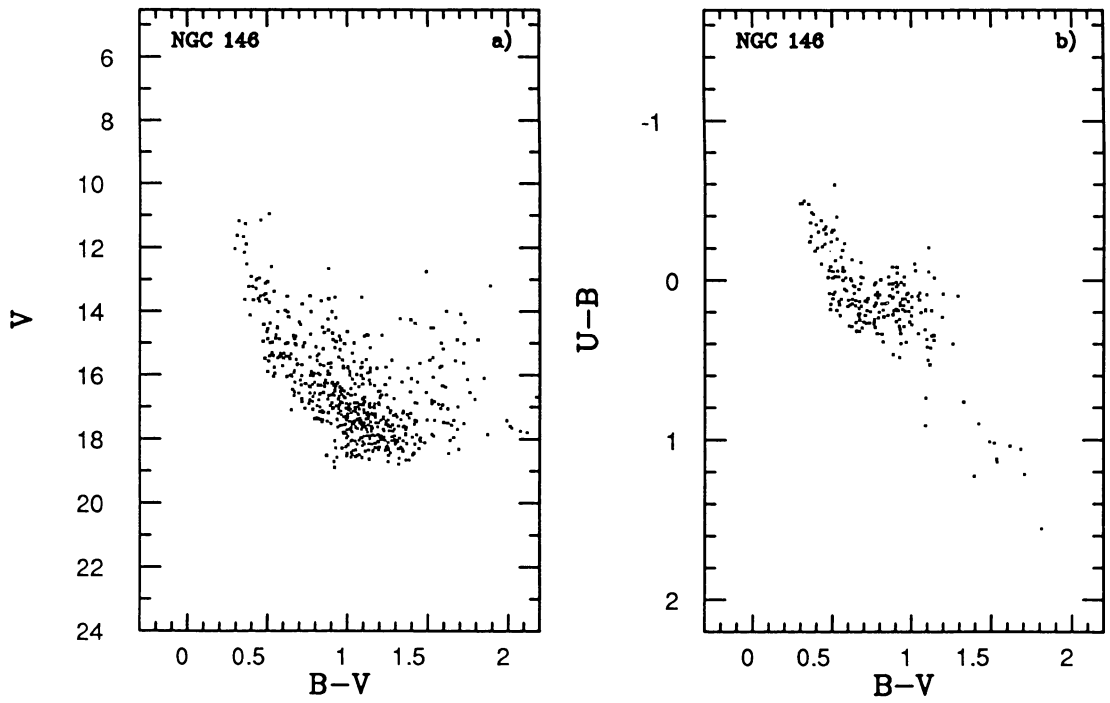

FIG. 63.—(*a*) Color-magnitude diagram for NGC 146. (*b*) Two-color diagram for NGC 146.

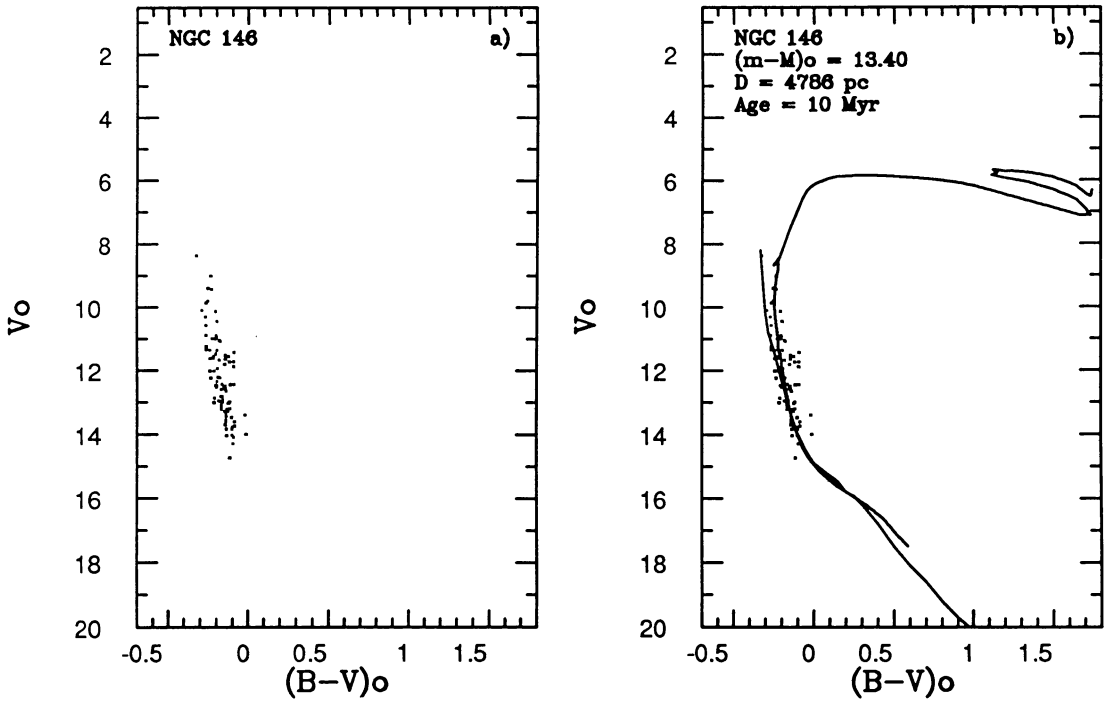

FIG. 64.—(*a*) Reddening-corrected CMD for stars in Fig. 63 with $(B - V) < 0.70$. (*b*) Fit of the Schmidt-Kaler (1982) ZAMS and 10 Myr isochrone of Maeder & Meynet (1991) to the reddening-corrected CMD.

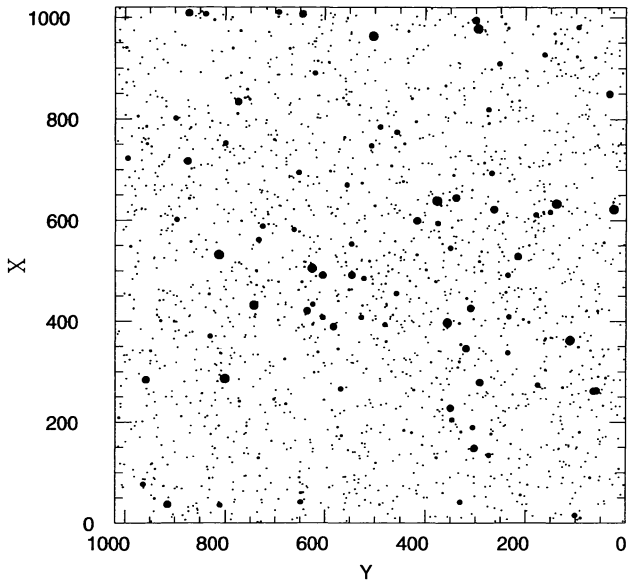

FIG. 65.—Map of King 15 generated from the list of stars appearing in the CMD. The scale is 0.″68 pixel^{-1}, giving a field of view of 11.′6. North is up, and east is to the left.

A fit of the SK82 MSTCC to the higher mass stars of Figure 75*b* results in a reddening estimate of $E(B-V) = 0.55$. A fit of the ZAMS to the CMD of Figure 75*a* is also consistent with this reddening estimate and results in a determination of $(m - M)_v = 14.61$ and $(m - M)_0 = 12.90$, or a distance of 3802 pc. This distance is considerably larger than that found by Hardorp (1960), but he observed far fewer stars, used a lower reddening, and fitted the middle of his observed main sequence, which itself had a large amount of scatter. It is interesting to note that the bend in his shifted ZAMS is located at $V \sim 15$ rather than at $V > 16$ as is found in Figure 75*a*. It is impossible to match the shape of the SK82 ZAMS using his reddening and distance. The 20 Myr MM91 isochrone is also shown in Figure 75*a,* indicating that NGC 103 is a moderately young cluster.

5.20. *Berkeley 60*

Because of time limitations, only short exposures were obtained for Berkeley 60 (Be 60). The map of the observed region, based upon the photometry, is shown in Figure 76, while the CMD and two-color diagram are shown in Figures 77*a* and 77*b,* respectively. Despite the short exposures, the photometry reaches $V \sim 18$, with no obvious cluster present in either the CMD or the two-color diagram. With identical exposures for another cluster, Be 58 (see below), a distinct cluster is visible. It is therefore doubtful that a cluster exists in the location cataloged as Be 60, and this location is excluded from further consideration.

5.21. *Berkeley 1*

As in the case of Be 60, only short integration times were obtained for Be 1. The resulting photometric map is shown in Figure 78, and the CMD and two-color diagram are shown in Figures 79*a* and 79*b,* respectively. As in Be 60, there is no obvious cluster present, although the two-color diagram does suggest the presence of several mid- to late-type B stars in the field. Be 1, like Be 60, is another doubtful or very poor cluster and is excluded from further consideration.

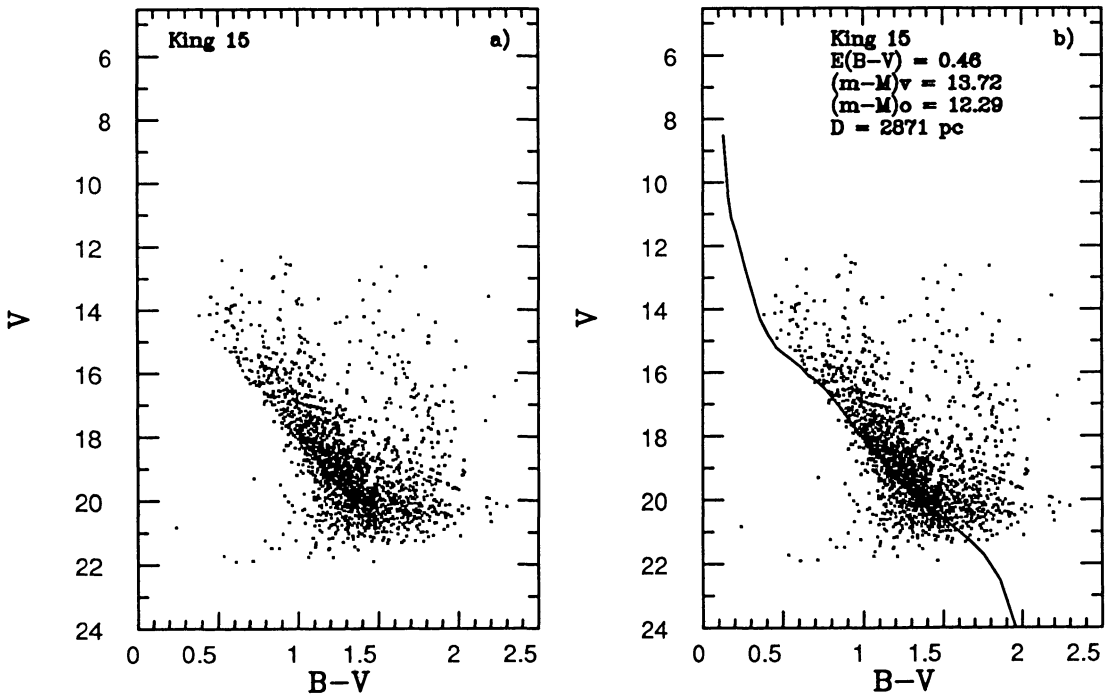

FIG. 66.—(*a*) Color-magnitude diagram for King 15. (*b*) Fit of the Schmidt-Kaler (1982) ZAMS to King 15.

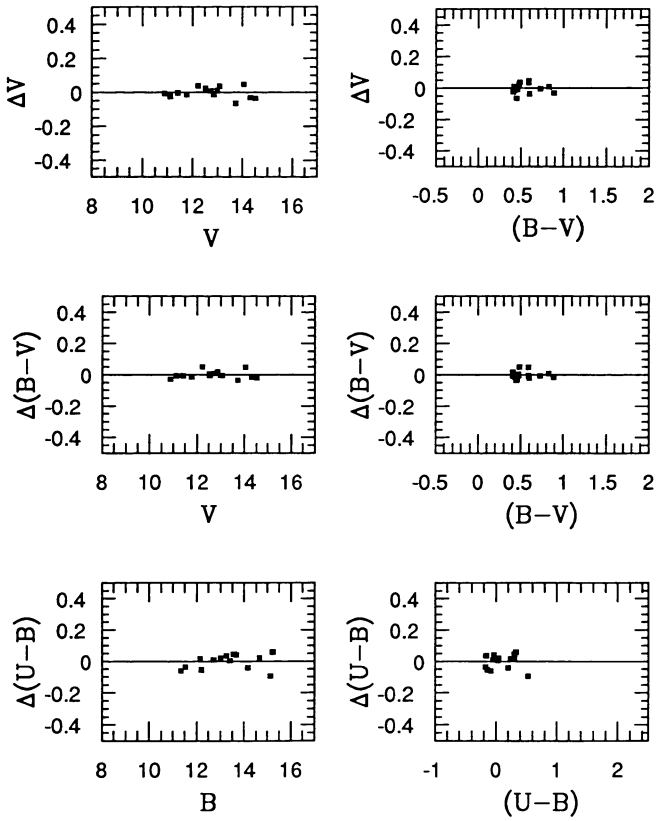

FIG. 67.—Residuals of the fit of the NGC 129 stars of Hoag et al. (1961), used as local standard stars.

5.22. *Berkeley 58*

Berkeley 58 (Be 58) is a little-studied cluster that lies in the general direction of the Cepheid variable CG Cas (Tsvetkov 1989; Frolov 1974). Approaching cloud cover allowed only short exposures of the cluster to be made, and the photometric quality of the observations may be suspect. A map of the cluster region is shown in Figure 80. As in the case of Be 1 and Be 60, the photometry reaches only $V \sim 18$, but a sequence of stars is clearly visible in the CMD and two-color diagram of Be 58, where none is visible in the other two clusters (Fig. 81*a*). The cross in Figure 81 indicates the position of the Cepheid variable CG Cas, from the mean photometric values of Fernie & Hube (1968).

The selection of stars within $R_{\rm full}$ (Table 4) minimizes contamination from field stars in the determination of the cluster parameters. A distinct sequence of stars is visible in the two-color diagram (Fig. 82*a*). A fit of the SK82 MSTCC to this smaller sample of stars (Fig. 82*b*) results in a determination of $E(B-V) = 0.55$ for the cluster. A fit of the SK82 ZAMS to the cluster CMD is shown for the same sample of stars in Figure 83*a*, where $(m-M)_v = 14.55$ and $(m-M)_0 = 12.95$, or a distance of 3715 pc is found. Using these values of reddening and distance, an old age is inferred for the cluster from the shape of the observed CMD. The fit of the MM91 isochrone for 251 Myr is also shown in Figure 83*a*. This age is consistent with the two-color diagram where the earliest star on the reddened SK82 MSTCC is a B8–B9, with a main-sequence lifetime of ~200–300 Myr from Figure 1 of Maeder & Meynet (1988).

The location of CG Cas in the CMD and two-color diagram is also shown in Figure 83. Based upon the derived parameters for Be 58, it appears that CG Cas is not associated with Be 58—a result supported by the proper-motion analysis of Frolov (1974), who also shows that CG Cas is not associated with the cluster. The questionable photometric nature of the observations makes these results tentative, and follow-up studies of this cluster are warranted.

5.23. *NGC 7790*

NGC 7790 is a well-studied cluster because of its association with three known Cepheid variables, CE Cas A, CE Cas B, and CF Cas. Romeo et al. (1989) obtained *BVRI* CCD photometry of a 4.'7 × 4.'7 area of the cluster and found $E(B-V) = 0.54 \pm 0.04$, based on a conversion of $E(V-I)$ to $E(B-V)$ and a ZAMS fit in the CMD, and $(m-M)_0 = 12.65 \pm 0.15$ (3388 pc), based upon the Pleiades sequence of Turner (1976), who assumes a distance modulus for the Pleiades of 5.57 (Feast & Walker 1987). From stellar models without overshooting, Romeo et al. find an age of 50 Myr, while from models which use convective overshooting they determine an age of 100 Myr. Using the theoretical period-age relation for Cepheids determined by Kippenhahn & Smith (1969), Romeo et al. (1989) find that the Cepheids imply a minimum age of 80 Myr for cluster.

Earlier studies of NGC 7790 include photometry by Sandage (1958), Pedreros, Madore, & Freeman (1984), and Alcala & Arellano Ferro (1988). NGC 7790 was also used by the KPNO video camera/CCD standards consortium as a cluster for standard star measurements (Christian et al. 1985).

The photometry of NGC 7790 in this study was obtained on a nonphotometric night and necessitated the use of local stan-

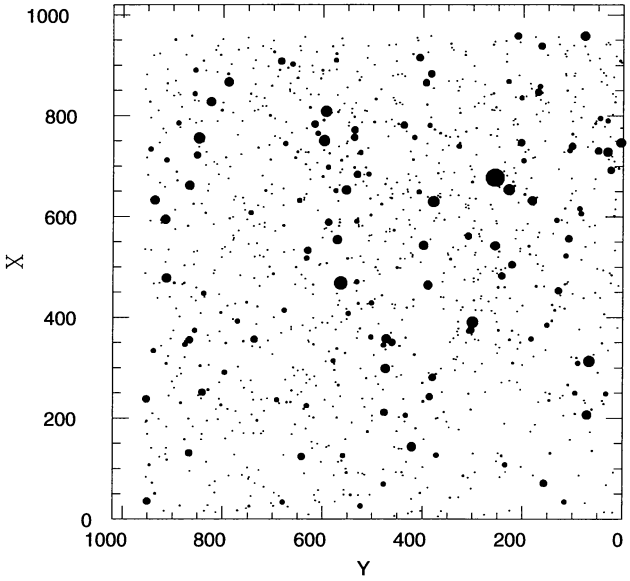

FIG. 68.—Map of NGC 129 generated from the list of stars appearing in the CMD. The scale is 0.″68 pixel^{-1}, giving a field of view of 11.'6. North is up, and east is to the left.

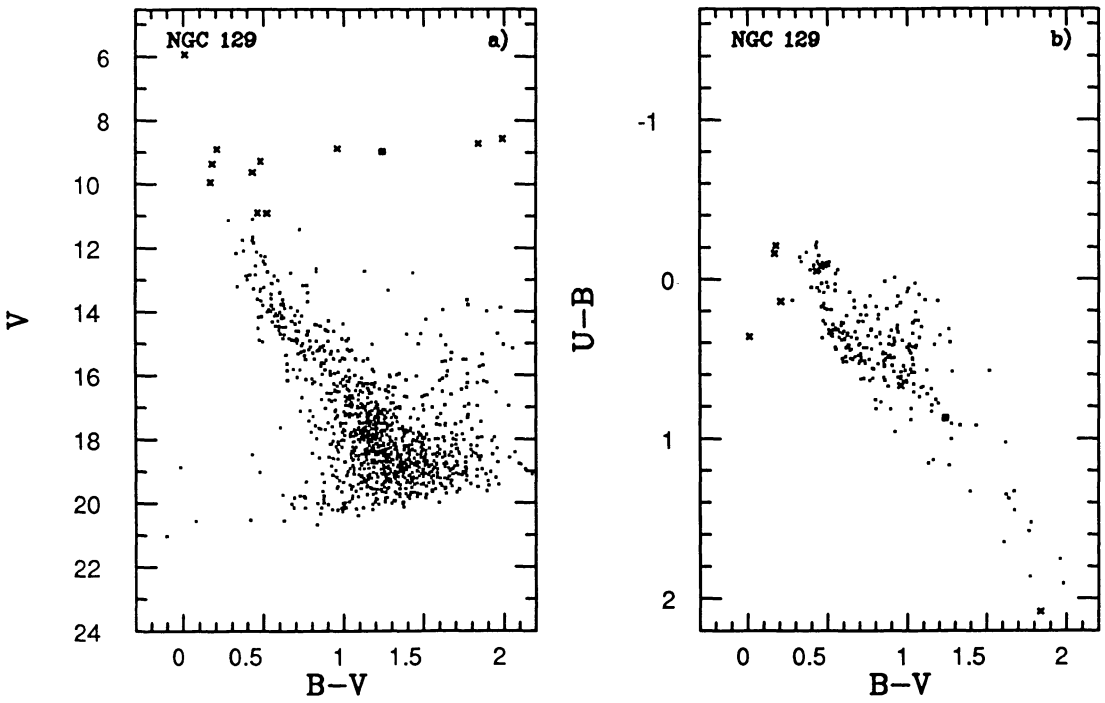

FIG. 69.—(*a*) Color-magnitude diagram for NGC 129. (*b*) Two-color diagram for NGC 129. Crosses represent stars whose photometry is taken from Hoag et al. (1961). The mean magnitude and color of DL Cas from Arp et al. (1959) are indicated by the open square.

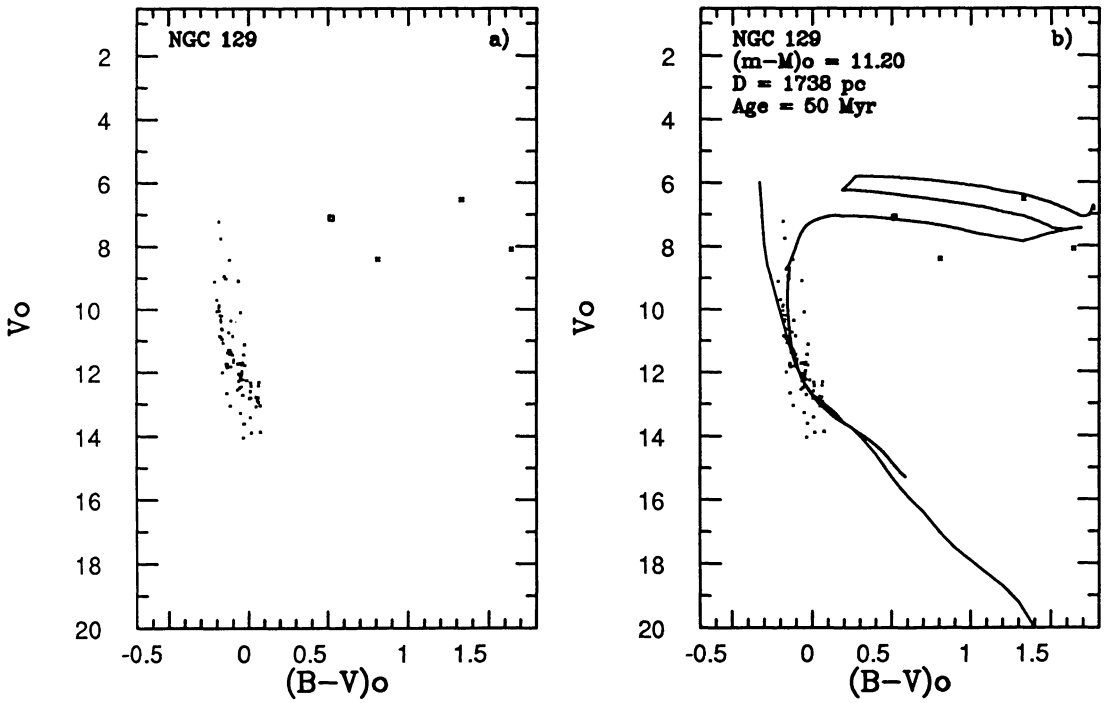

FIG. 70.—(*a*) Reddening-corrected CMD for NGC 129. (*b*) Fit of the 50 Myr isochrone of Maeder & Meynet (1991) to the reddening-corrected CMD of NGC 129. Symbols are the same as those in Fig. 69.

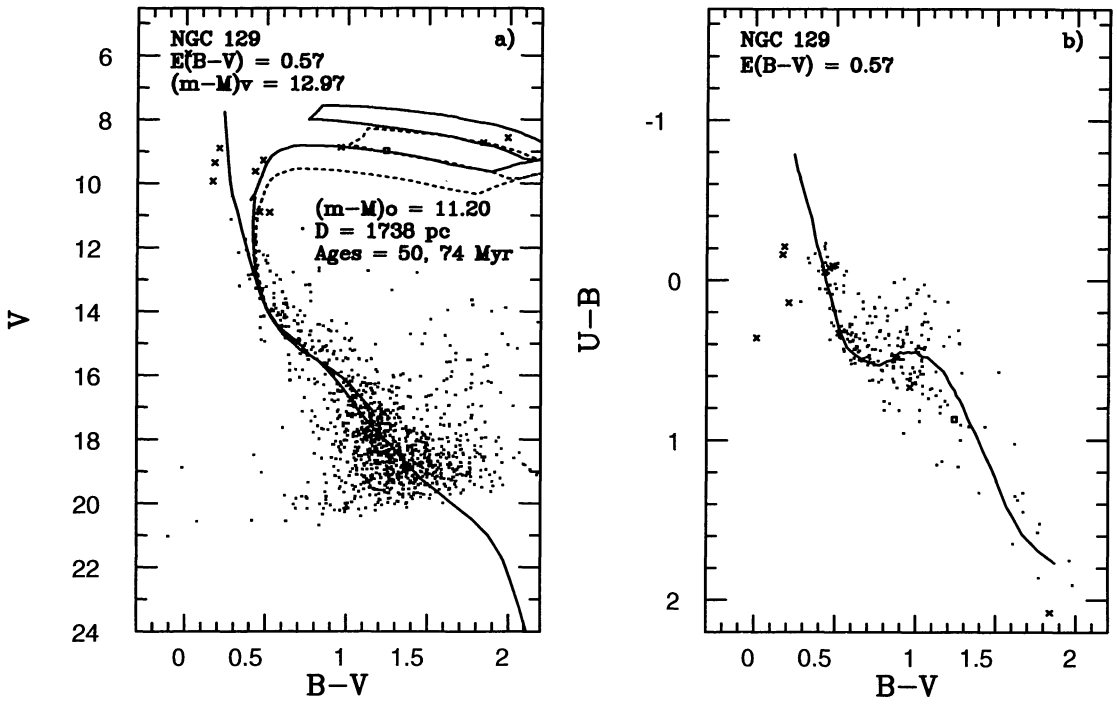

FIG. 71.—(*a*) Fit of the Schmidt-Kaler (1982) ZAMS and Maeder & Meynet (1991) isochrones to the CMD of NGC 129. (*b*) Fit of the Schmidt-Kaler (1982) main-sequence two-color curve to the two-color diagram of NGC 129. Symbols are the same as those in Fig. 69.

dards from observations by other authors. Neither the Christian et al. (1985) nor the Romeo et al. (1989) studies included U photometry, so they were not used. Instead the photometric values in Table 1 of Pedreros et al. (1984) were as local standards. These are values from Sandage (1958) corrected by $\Delta(U-B) = 0.075$ mag, which is the offset found by Pedreros et al. (1984) after a comparison of Sandage's photometry with their own U-band photometry for 16 stars in common with Sandage. The residuals of our fit to the Pedreros et al. (1984) local standard stars were ~0.05 mag in V, $(B-V)$ and $(U-B)$ and are shown in Figure 84.

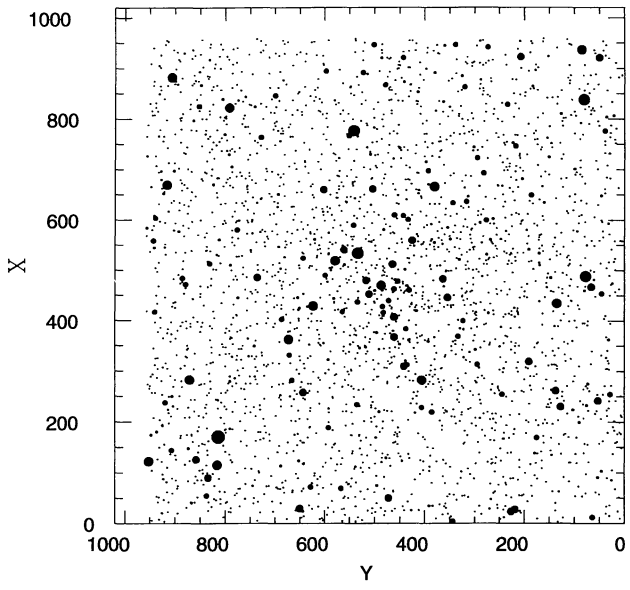

FIG. 72.—Map of NGC 103 generated from the list of stars appearing in the CMD. The scale is 0".68 pixel^{-1}, giving a field of view of 11'.6. North is up, and east is to the left.

A map of the observed field is shown in Figure 85, and the CMD and two-color diagram are shown in Figure 86. The crosses indicate the positions of the Cepheid variables CE Cas a, CE Cas b, and CF Cas. The values for CE Cas a [$\langle V\rangle$ = 10.90, $\langle(B-V)\rangle$ = 1.15] and CE Cas b [$\langle V\rangle$ = 11.04, $\langle(B-V)\rangle$ = 1.07] are from Opal et al. (1988), while those for CF Cas [$\langle V\rangle$ = 11.14, $\langle(B-V)\rangle$ = 1.24, $\langle(U-B)\rangle$ = 0.87] are from Sandage (1958). The open square indicates the position of the variable star QX Cas in the NGC 7790 field (Sandage 1958).

A fit of the SK82 MSTCC is shown in Figure 87*b*, where $E(B-V) = 0.55$ is found. A fit of the SK82 ZAMS in Figure 87*a* gives $(m-M)_v = 14.56$, which corresponds to $(m-M)_0 = 12.75$, or a distance of 3548 pc. The age of NGC 7790 is constrained by the turnoff of the main sequence as well as the mean location of the Cepheids, and is well fitted by the MM91 71 Myr isochrone (Fig. 87*a*). This isochrone, however, places the Cepheids on the first crossing track, rather than the end of the blue loop where they are more likely to be found. The 100 Myr isochrone places the Cepheids at the end of this loop but does not fit the main-sequence turnoff as well. We therefore use the 71 Myr age, although we cannot rule out an age as high as 100 Myr.

6. DISCUSSION

The total number of stars which appear in the CMDs in the preceding pages is 35,788, with only 9.7% of them being cluster

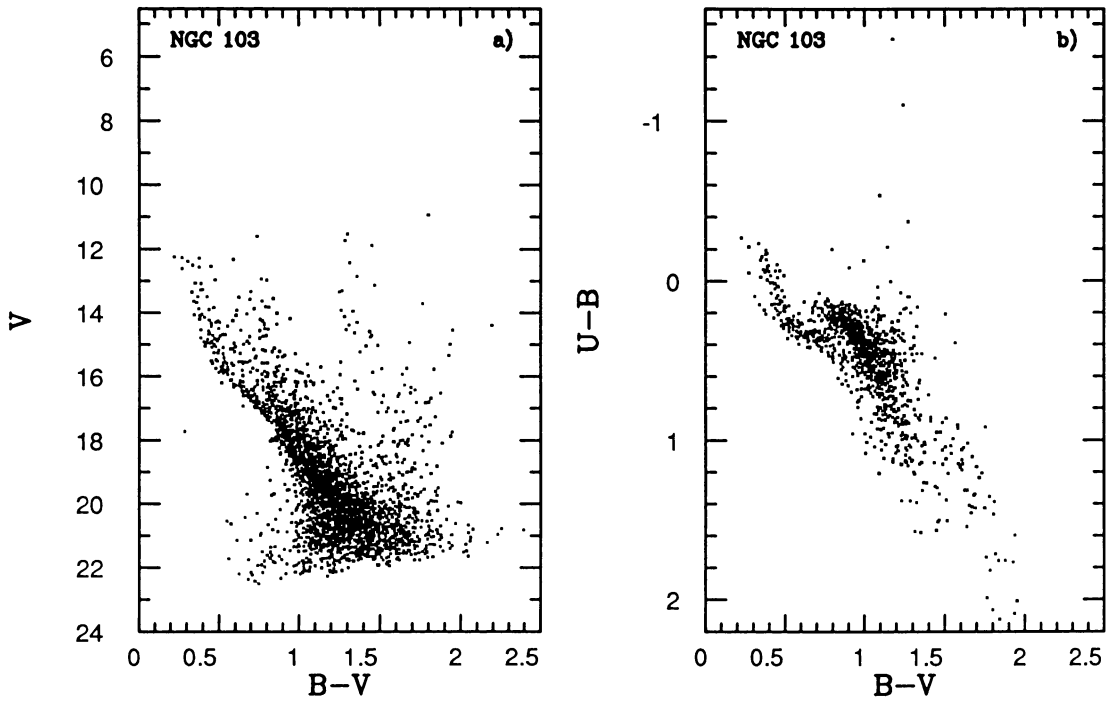

FIG. 73.—(*a*) Color-magnitude diagram for NGC 103. (*b*) Two-color diagram for NGC 103.

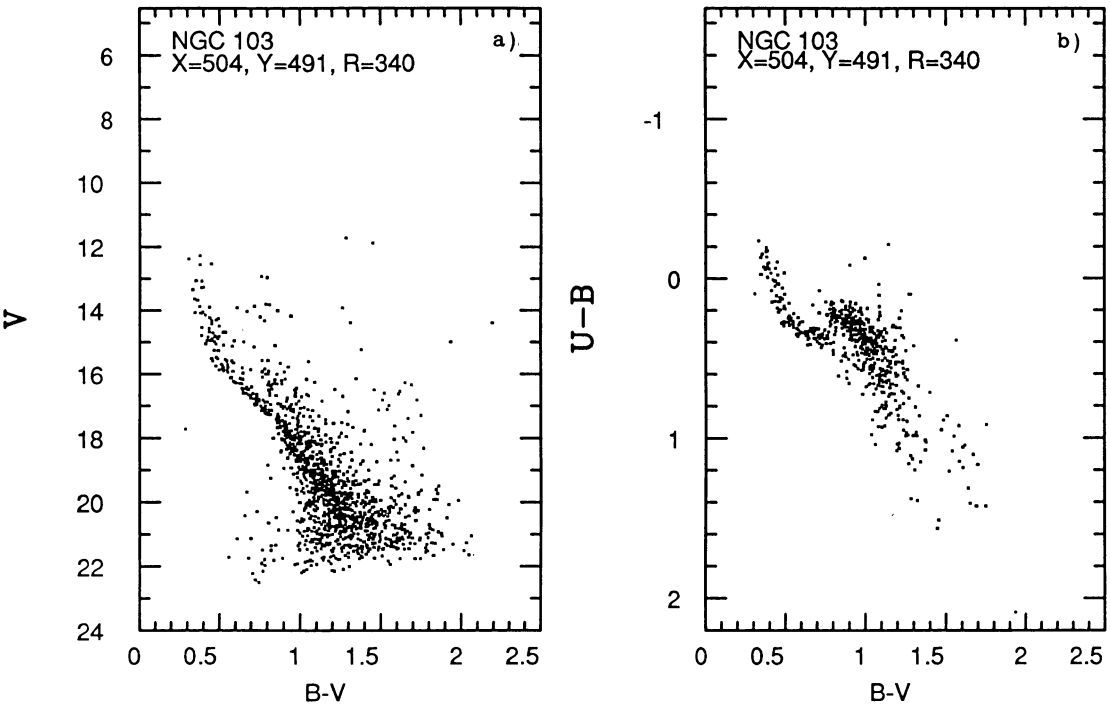

FIG. 74.—(*a*) Color-magnitude diagram for stars within $R_{\rm full}$ of the center of NGC 103. (*b*) Two-color diagram for stars within $R_{\rm full}$ of the center of NGC 103.

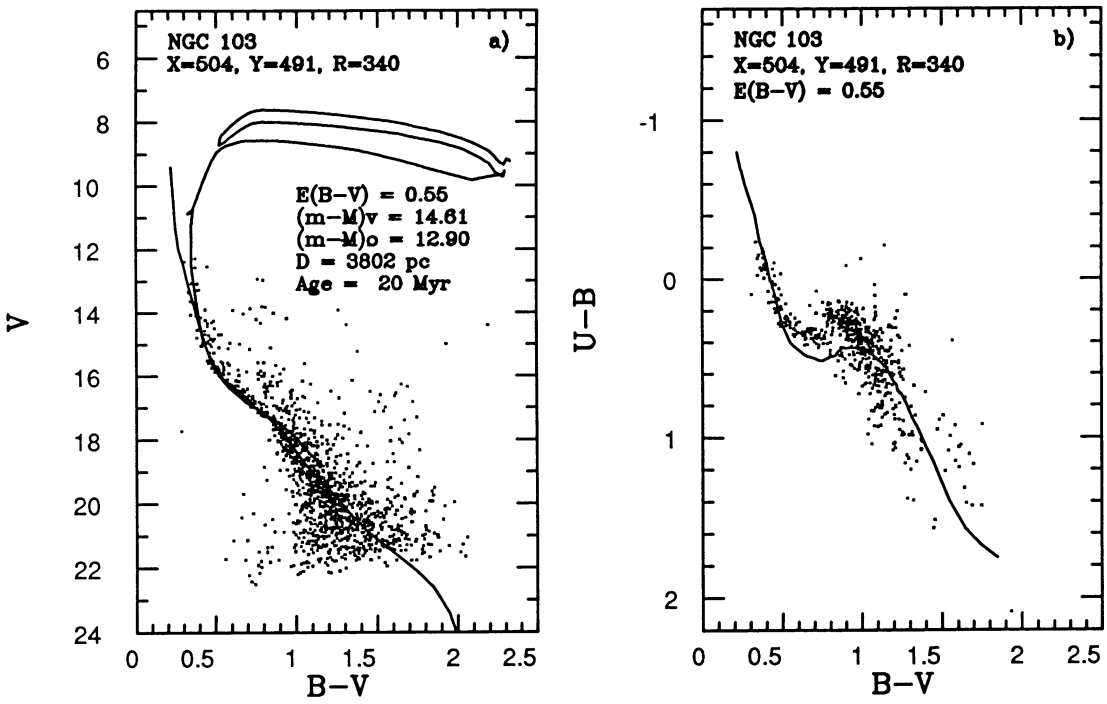

FIG. 75.—(*a*) Fit of the Schmidt-Kaler (1982) ZAMS and 20 Myr isochrone of Maeder & Meynet (1991) to NGC 103. (*b*) Fit of the Schmidt-Kaler (1982) main-sequence two-color curve to NGC 103.

stars, based on the cumulative distributions (Table 4). The parameters for the individual clusters, as determined in the previous section, are summarized in Tables 3 and 4. In Table 3, columns (2)–(7) give the cluster name, Galactic longitude, Galactic latitude, $E(B-V)$, $(m-M)_0$, and distance in parsecs, respectively. Columns (8)–(10) list the X, Y, and Z components of the cluster distances relative to the Sun, with X directed along $l = 90°$, Y directed along $l = 180°$, and Z the distance above (+) or below (−) the plane. Column (11) lists the derived ages of the clusters. In Table 4, columns (3)–(8) list $R_{\rm full}$ in arcminutes, $R_{\rm full}$ in parsecs, $R_{\rm HWHM}$ in arcminutes, $R_{\rm HWHM}$ in parsecs, the net number of cluster stars ($V < 20$–21) from the cumulative distribution ($N_{\rm cluster}$), and the total number of stars ($V < 20$–21) in the CMDs of the clusters under study ($N_{\rm observed}$). These two tables provide the basic information on the observed open clusters which will be discussed in forthcoming papers.

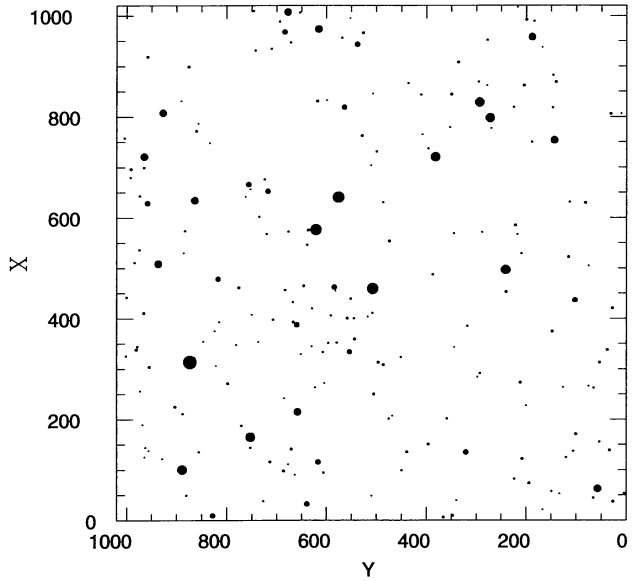

FIG. 76.—Map of Be 60 generated from the list of stars appearing in the CMD. The scale is 0.″68 pixel^{-1}, giving a field of view of 11.′6. North is up, and east is to the left.

Among the results of this survey are the following:

1. *Spatial distribution of clusters.*—Figure 88 shows the spatial distribution of the 20 open clusters for which distances were obtained. The numbers correspond to those of column (1) in Tables 3 and 4. With the exceptions of NGC 381 (11), NGC 129 (18), and NGC 146 (16), the clusters form a complex, ~1000 pc in length, as seen from the Sun, suggesting that the width of the Perseus spiral arm is of this order. The isolation of NGC 103 (19), Be 58 (22), and NGC 7790 (23) from the other clusters in the complex is due to incomplete sampling of clusters toward lower Galactic longitudes.

The average displacement of clusters from the Galactic plane, defined by $b = 0°$, is −56 pc with a dispersion of 76 pc. Using the data from Fich & Blitz (1984), the optical H II regions in the range $100° < l < 180°$, within 1.5–4 kpc from the Sun, have a mean displacement of −7 pc from the plane, with a similar dispersion (89 pc), indicating that the open clusters observed in this survey tend to be systematically farther below the plane than the H II regions, although at least one H II region (S184) is more than 200 pc below the plane. The nearby young

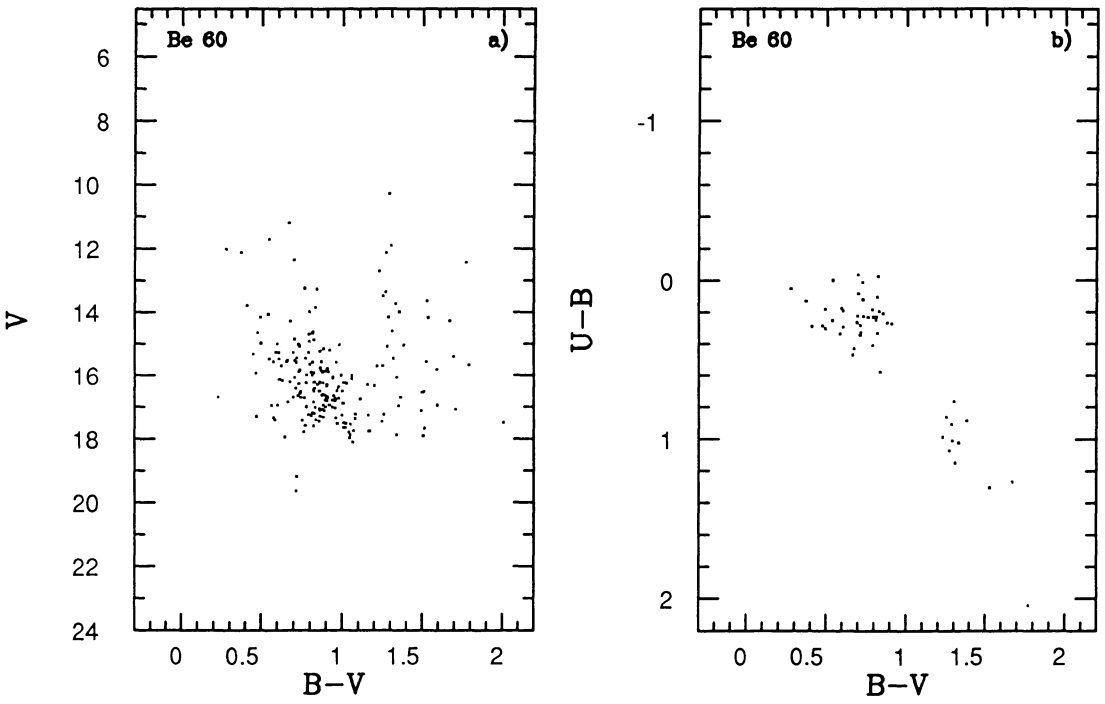

FIG. 77.—(*a*) Color-magnitude diagram for Be 60. (*b*) Two-color diagram for Be 60.

clusters h and χ Per, not observed in this survey, are also located more than 200 pc below the plane.

Several old clusters (NGC 381 and King 15) were observed, and, with the 1.6 Gyr cluster IC 166 (Lyngå 1987), indicate that a small number of old clusters are present throughout the region. There are, however, no moderate-age (~100 Myr) clusters located in the nearly completely sampled latitude range $126° < l < 130°$, although such clusters are seen toward lower longitudes. No obvious correlation of age with distance from the plane is apparent.

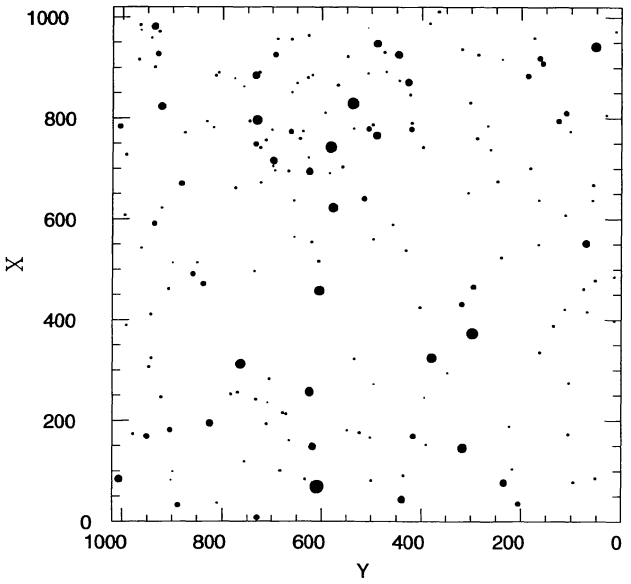

FIG. 78.—Map of Be 1 generated from the list of stars appearing in the CMD. The scale is 0.″68 pixel^{-1}, giving a field of view of 11.′6. North is up, and east is to the left.

2. *Cluster distances.*—Large differences in distances, relative to other studies, are found for several clusters, including Be 62 and NGC 436. The discrepancies in distances arise primarily from the brighter limiting magnitudes of the previous studies, resulting in poorly constrained fits of the data to the ZAMS. This highlights the need for deep photometry of clusters if their spatial distribution is to be reliably determined.

3. *Cluster richness.*—The median number of stars identified as cluster members, taken to be a measure of the cluster richness (Table 4), is ~100. In general, this refers to the number of stars with masses greater than 1–1.5 $M_\odot$, with the actual mass limit depending on the limiting magnitude of the photometry, the reddening, and the distance of each cluster. The actual cluster membership must be substantially larger than this value. No obvious correlation between cluster richness and cluster age was found.

4. *Cluster radii.*—The average cluster radius ($R_{\rm HWHM}$), from Table 4, is 1.6 pc with a dispersion of 0.70 pc. This is consistent with the Janes, Tilley, & Lyngå (1988) result that the majority of young clusters have diameters less than 5 pc. No obvious correlation of cluster radius with age is seen.

5. *Cluster ages.*—Several clusters (Be 7, NGC 663, NGC 654, NGC 637, NGC 581, and NGC 457) show evidence of a spread in ages of the high-mass stars, with the mean age spread being 10 Myr. The age spreads are determined from the high-mass stars, rather than from a comparison between low-mass PMS contraction ages and high-mass turnoff ages. The smallest clusters (Be 7 and NGC 637), with radii less than 2–2.5 pc,

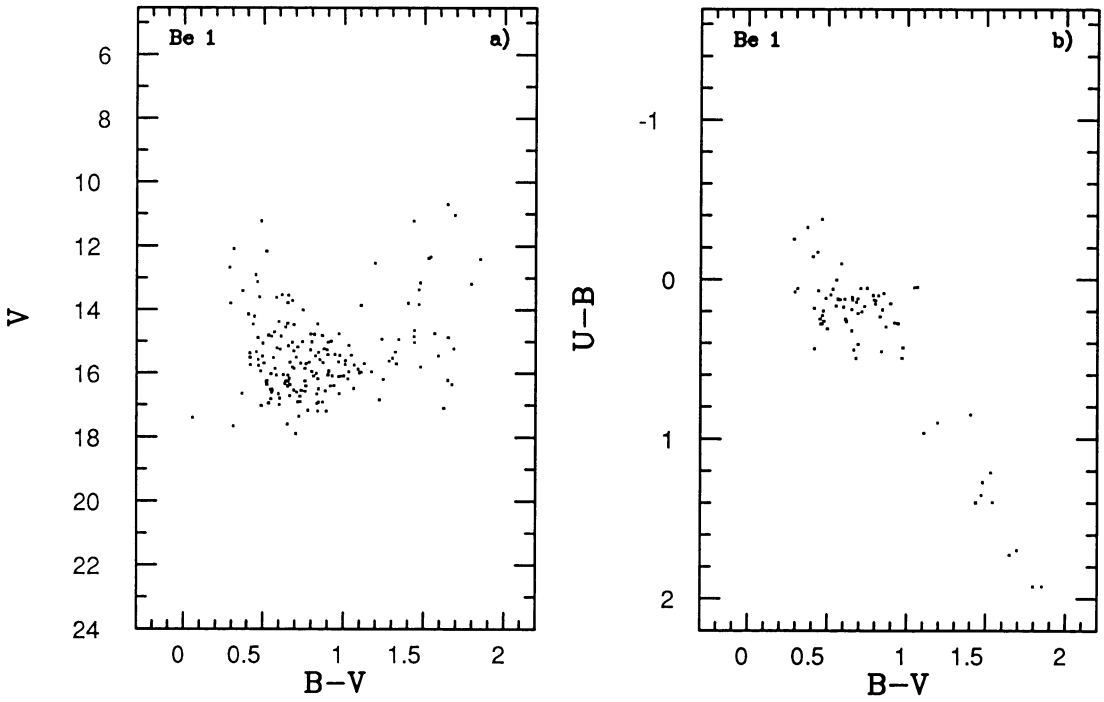

FIG. 79.—(*a*) Color-magnitude diagram for Be 1. (*b*) Two-color diagram for Be 1.

have the smallest age spread (4 Myr), while the larger clusters (NGC 663, NGC 654, NGC 581, and NGC 457), have inferred age spreads of more than 10 Myr.

6. *Reddening.*—There is no strong correlation of reddening with cluster age, although the oldest clusters do have slightly lower reddening than the very youngest ones. The dominant correlation of reddening is with the cluster distance from the Galactic plane, with lower reddenings measured for clusters located farther from the plane. A contribution of $E(B-V) = 0.45$–0.50 to the observed reddenings appears to be due to the intervening material between the Sun and the Perseus arm itself.

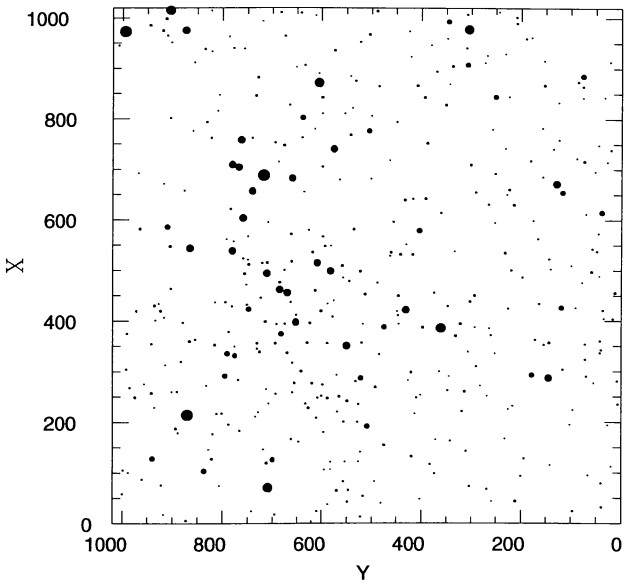

FIG. 80.—Map of Be 58 generated from the list of stars appearing in the CMD. The scale is 0.″68 pixel^{-1}, giving a field of view of 11.′6. North is up, and east is to the left.

7. *Cluster age versus gas content.*—Standard ideas of star formation lead to the expectation that the gas around a cluster will be rapidly dispersed after the cluster forms. Recent investigations of the CO toward several of the program clusters have tested this hypothesis. Liu et al. (1988) established a gas-cluster association for NGC 654 and NGC 637 (see their Table VI) but not for NGC 581. They were unable, however, to establish a correlation of gas content with cluster age, using an age of 218 Myr (Janes et al. 1988) for NGC 637. This study has shown NGC 637 to be 0–4 Myr old, however. Leisawitz et al. (1989) investigated the gas-cluster association using a much larger sample, including many of the clusters studied in this survey. They concluded that the molecular material around clusters is disrupted within $\sim$10 Myr of a cluster's formation, and that clouds that exist are receding at $\sim$10 km s^{-1} from the clusters.

This study provides an opportunity to reevaluate the Liu et al. (1988) and Leisawitz et al. (1989) results, with improved ages for the clusters and improved kinematic velocities which result from the new distances. New radial velocity measurements for several of the clusters (Liu, Janes, & Bania 1989) are also available. Table 7 presents the results of this investigation, with the clusters listed in order of increasing age. Column (2) lists the adopted ages of the clusters, in units of 10^6 yr. Because of uncertainties in the adopted ages, column (3) lists the adopted age group, in 10 Myr intervals, with H II regions represented by 0, clusters with ages 1–10 Myr represented by 1, and

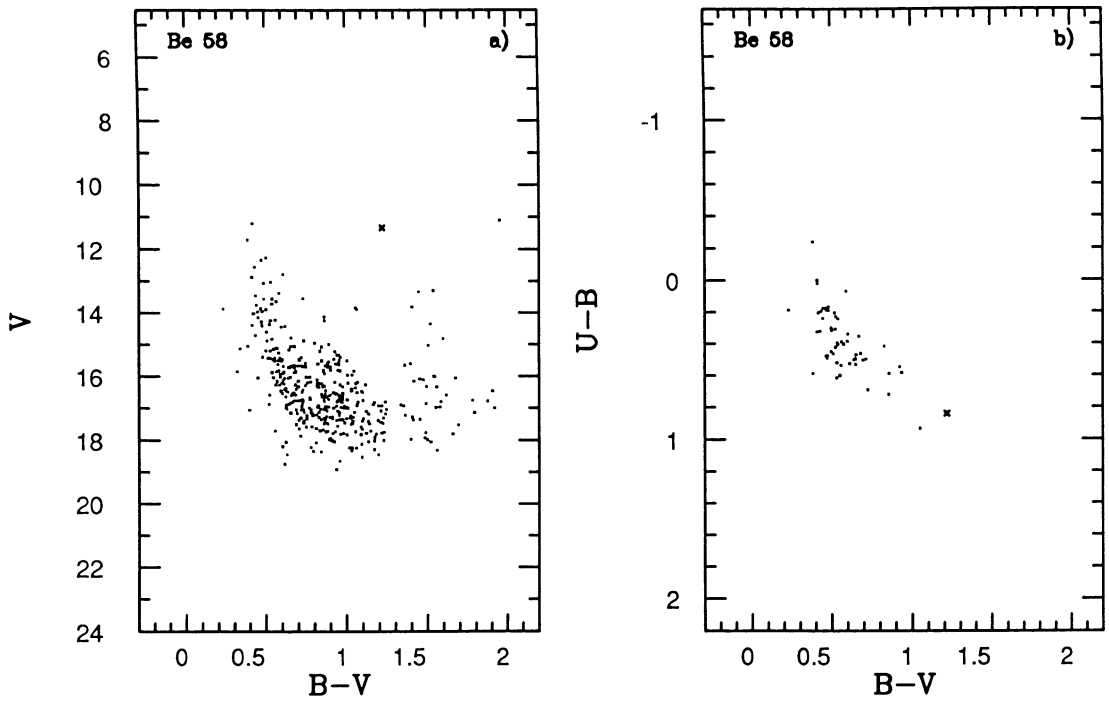

FIG. 81.—(*a*) Color-magnitude diagram for Be 58. (*b*) Two-color diagram for Be 58. The cross represents the mean photometric values of CG Cas, from Fernie & Hube (1968).

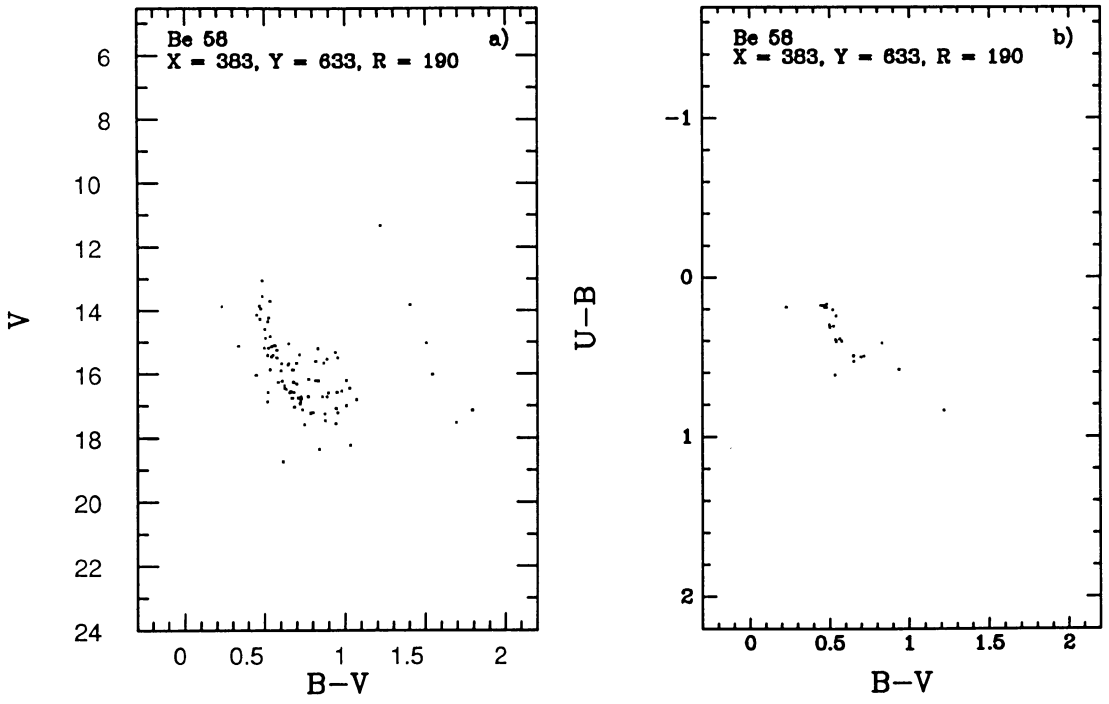

FIG. 82.—(*a*) Color-magnitude diagram for stars within R_{full} of the center of Be 58. (*b*) Two-color diagram for stars within R_{full} of the center of Be 58. The cross represents the mean photometric values of CG Cas, from Fernie & Hube (1968).

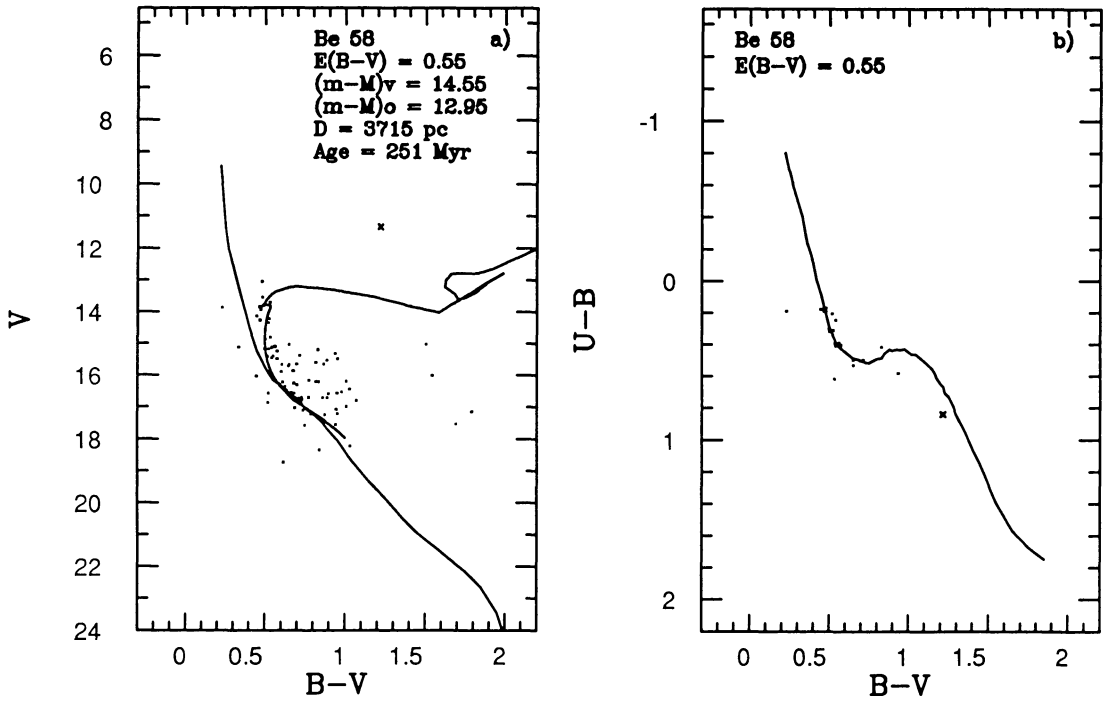

FIG. 83.—(*a*) Fit of the Schmidt-Kaler (1982) ZAMS and 251 Myr isochrone of Maeder & Meynet (1991) to Be 58. (*b*) Fit of the Schmidt-Kaler (1982) main-sequence two-color curve to Be 58. The cross represents the mean photometric values of CG Cas, from Fernie & Hube (1968).

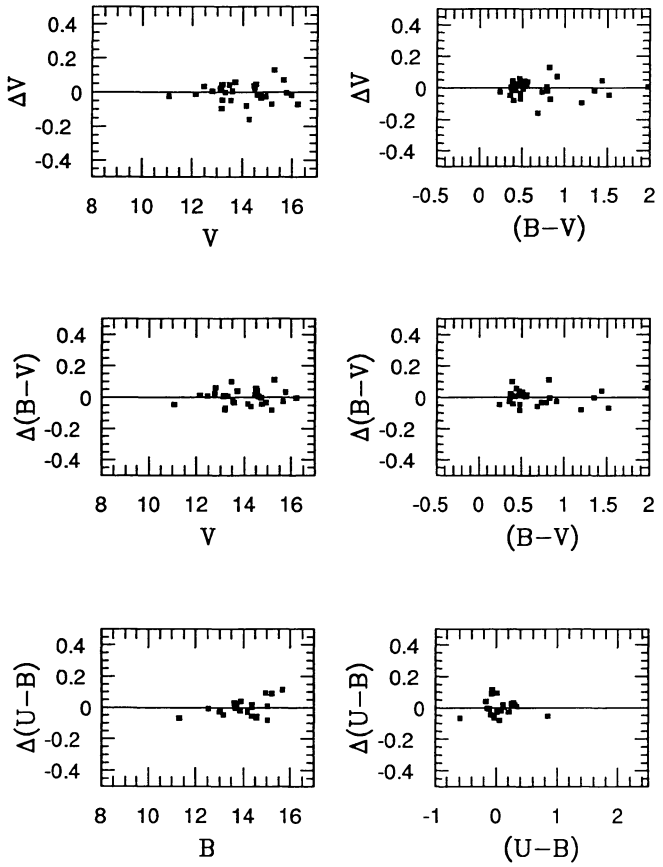

FIG. 84.—Residuals of the fit to the Pedreros et al. (1984) photometry of NGC 7790 stars used as local standards.

so on. Because some clusters exhibit a range in ages, the youngest and oldest derived ages are listed in both columns. Column (4) lists the adopted LSR velocity of the cluster, in kilometers per second, with the source of the velocity listed in column (9). The velocities are from direct measurements, taken from Liu et al. (1989) (LJB), when available, or kinematic velocities (Kin), using the new distances and the Clemens (1985)

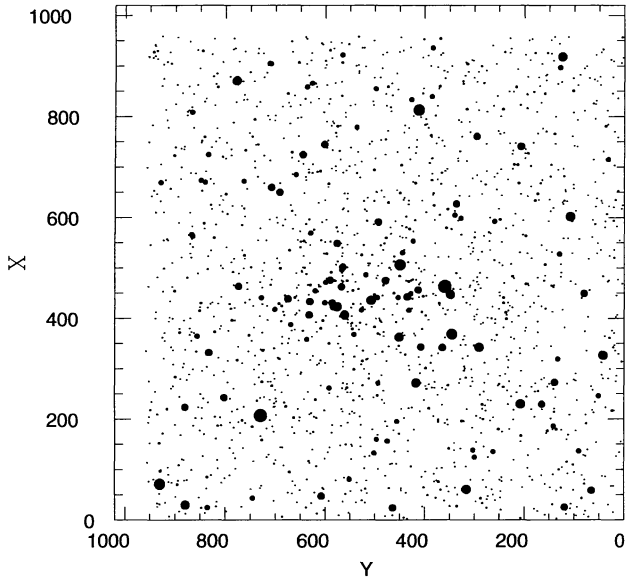

FIG. 85.—Map of NGC 7790 generated from the list of stars appearing in the CMD. The scale is 0.″68 pixel^{-1}, giving a field of view of 11.′6. North is up, and east is to the left.

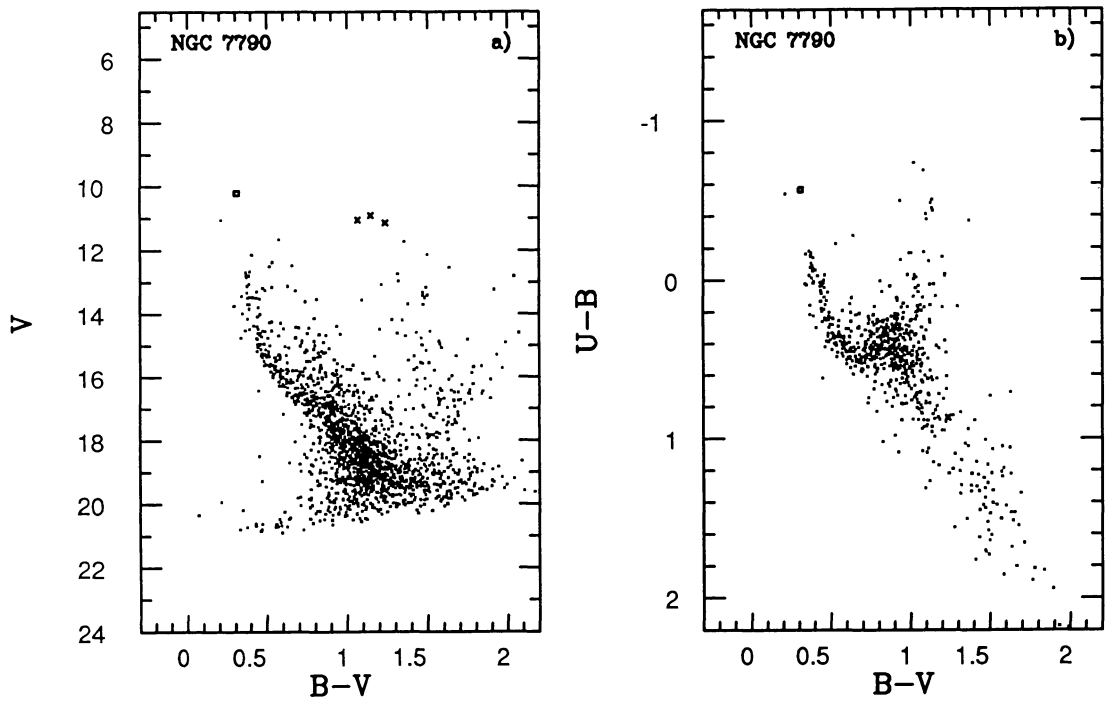

FIG. 86.—(*a*) Color-magnitude diagram for NGC 7790. (*b*) Two-color diagram for NGC 7790. Crosses indicate the mean positions of the Cepheid variables CE Cas a, CE Cas b, and CF Cas (Opal et al. 1988; Sandage 1958). The open square indicates the position of a variable star in the NGC 7790 field (Sandage 1958).

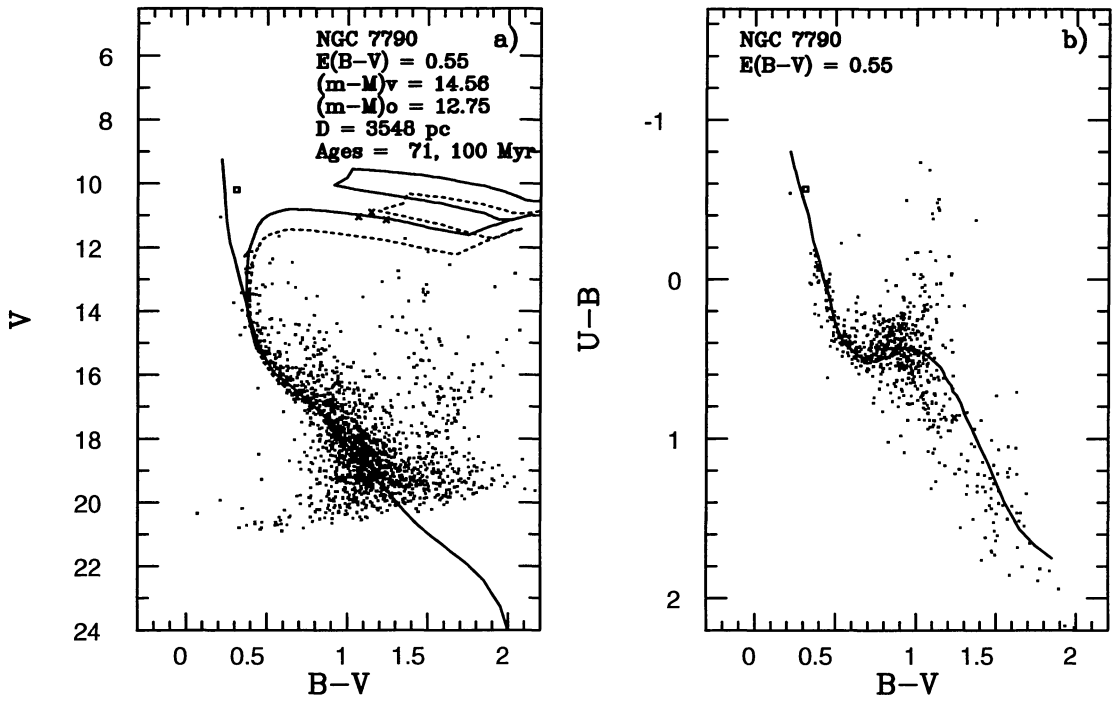

FIG. 87.—(*a*) Fit of the Schmidt-Kaler (1982) ZAMS and Maeder & Meynet (1991) isochrones to the CMD of NGC 7790. (*b*) Fit of the Schmidt-Kaler (1982) main-sequence two-color curve to the two-color diagram of NGC 7790. Symbols are the same as those in Fig. 86.

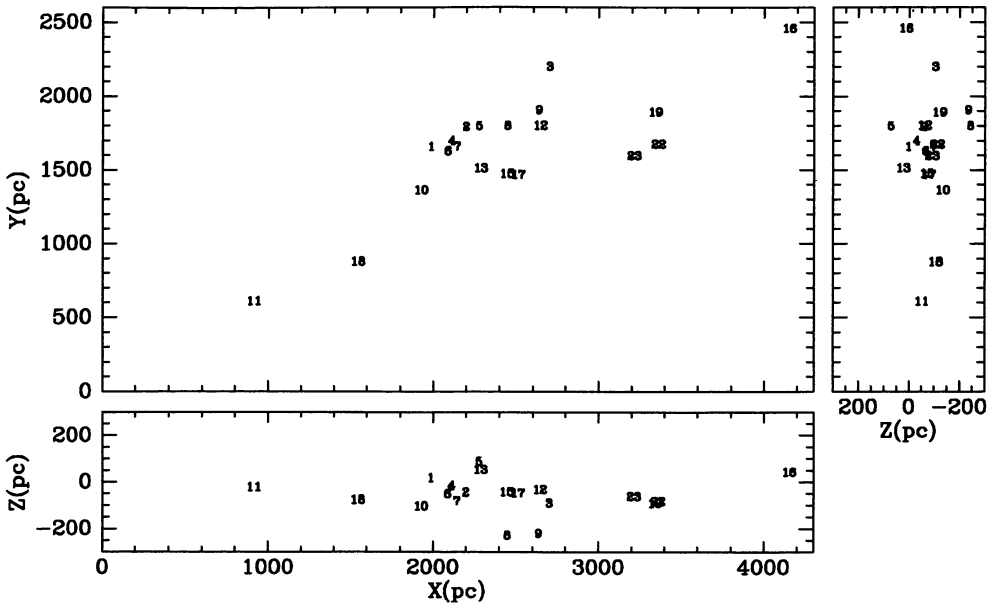

FIG. 88.—Spatial distribution of the program clusters. Numbers correspond to those in col. (1) of Tables 3 and 4.

rotation curve. An "x" in either of columns (5) and (6) indicates that CO gas was detected within 0–10 or 10–20 km s^{-1}, respectively, with the velocities of the CO near the clusters taken from Liu et al. (1988) (LJBP) or Leisawitz et al. (1989) (LBT).

Column (7) is a qualitative assessment of the degree to which the CO and cluster velocities correlate, from a strong correlation to no correlation at all. If CO was detected within 10 km s^{-1} of the cluster velocity, it was described as having a strong correlation. For NGC 659, however, the detected CO is close to the 10 km s^{-1} limit, and a weak correlation was assigned for it.

The results of this reevaluation of the cluster-age/gas-content relation are consistent with the Leisawitz et al. (1989) conclusion that little or no molecular material remains in the vicinity of a cluster after ~10 Myr. The only strong correlation found for CO and a cluster with an age older than 10 Myr is for NGC 663, although there is also gas at a wide range of velocities in the region. Without a larger sample of clusters, with self-consistent age determinations and well-determined radial velocities, rather than kinematic velocities, it is unlikely that this age limit can be improved upon.

8. *Luminosity functions.*—The stellar content of the clusters can be investigated. Two clusters (NGC 663 and NGC 654) appear to lie in front of molecular clouds, minimizing field star contamination in the CMDs, and reveal a large number of low-mass stars. Further discussion of the stellar content of many of the clusters will be presented in Paper II of this series.

9. *Binary stars.*—Two clusters (NGC 457 and NGC 436) show striking binary sequences, while at least two other clusters with similar ages and reddening (NGC 581 and NGC 103)

TABLE 7

CLUSTER AGE VERSUS GAS CONTENT

Name (1)	Age (Myr) (2)	Age Group (3)	V_{cl} (km s^{-1}) (4)	$V_{CO(10)}$ (km s^{-1}) (5)	$V_{CO(20)}$ (km s^{-1}) (6)	Correlation (7)	Reference (V_{cl}) (8)	Reference (V_{CO}) (9)
IC 1848	0	0	−41	x		Strong	LJB	LBT
NGC 281	0	0	−32	x		Strong	Kin	LBT
NGC 637	0–4	1	−41	x	x	Strong	LJB	LJBP
Be 62	10	2	−39	x		Strong	Kin	LBT
NGC 654	8–25	1–3	−29		x	Weak	LJB	LJBP
NGC 581	10–22	1–3	−37			No	LJB	LJBP
NGC 457	7–19	1–2	−20			No	LJB	LBT
NGC 663	12–25	2–3	−28	x	x	Strong	LJB	LBT
NGC 659	22	3	−43	x		Weak	Kin	LBT
NGC 103	20	3	−47		x	Weak	Kin	LBT
NGC 436	42	5	−43			No	Kin	LBT
NGC 433	79	8	−35		x	Weak	Kin	LBT

show no obvious binary sequence. A more detailed discussion of the binary content of the clusters will be presented in a forthcoming paper.

10. *Cepheid variables in clusters.*—Three of the clusters in the survey (NGC 129, NGC 7790, and Be 58) have Cepheid variable stars within or near them. The zero point of the period-luminosity relation is calibrated by Cepheids within open clusters. The distances and ages of NGC 129 and NGC 7790 are consistent with Cepheid membership, although the current photometry indicates that the Cepheid near Be 58 (CG Cas) may not be a member.

Further results for individual clusters include the following:

NGC 637.—The Lyngå (1987) catalog lists the derived age of this cluster as 218 Myr, although this study finds it to be less than 4 Myr old. This cluster was surveyed for CO gas by Liu et al. (1988) to establish a gas–cluster-age relation. The marginal detection of CO gas within 10 km s^{-1} of the mean cluster velocity (Liu et al. 1988) is much easier to explain in a cluster of 4 Myr than in one of 218 Myr.

NGC 433.—This cluster had long been classified as an OB cluster at a distance of 4500 pc (Alter 1944). This study, and the recent study by Battinelli et al. (1992), indicate that it is much older (~80 Myr) and much closer (~2300 pc).

This research was part of R. L. P.'s Ph.D. thesis work at Boston University. R. L. P. would like to thank the members of his thesis committee, Kenneth A. Janes, Alan P. Marscher, Daniel P. Clemens, James M. Jackson, and Charles J. Lada, for their help in improving the quality of this work. We would also like to thank the referee, Jean-Claude Mermilliod, for valuable comments and suggestions which have greatly improved the quality of this paper. The authors would also like to thank A. Maeder and G. Meynet for providing the evolutionary models and the program to convert them into isochrones, which were used for the determination of cluster ages, and Peter J. Sultan for his translation, from Russian to English, of the Frolov (1974) article on the proper motions of CG Cas and Be 58. This research has made use of the Simbad database, operated at the Centre de Données Stellaires, Strasbourg, France.

REFERENCES

Alcala, J. M., & Arellano Ferro, A. 1988, Rev. Mexicana Astron. Af., 16, 81
Alfaro, E. J., Cabrera-Cano, J., & Delgado, A., J. 1991, ApJ, 378, 106
Alfaro, E. J., & Garcia-Pelayo, J. M. 1984, A&AS, 58, 121
Alter, G. 1944, MNRAS, 104, 179
Arp, H., Sandage, A., & Stephens, C. 1959, ApJ, 130, 80
Baade, D. 1983, A&AS, 51, 235
Balasz, B. 1961, Astron. Abh. Hamburg, Vol. 5, No. 10
Battinelli, P., Capuzzo-Dolceta, R., & Nesci, R. 1992, AJ, 103, 1596
Becker, W. 1971, A&AS, 4, 241
Becker, W., & Stock, J. 1958, Z. Astrophys., 45, 282
Bertout, C. 1988, in Formation and Evolution of Low Mass Stars, ed. A. K. Dupree & M. T. V. T. Lago (Dordrecht: Kluwer), 45
Bertout, C., & Basri, G. 1991, in The Physics of Star Formation and Early Stellar Evolution, ed. C. J. Lada & N. D. Kylafis (Dordrecht: Kluwer), 649
Bevington, P. R. 1969, Data Reduction and Analysis for the Physical Sciences (New York: McGraw-Hill)
Boden, E. 1946, Uppsala Astron. Obs. Ann., Vol. 2, No. 1
———. 1950, Uppsala Astron. Obs. Ann., Vol. 2, No. 7
Cameron, L. M. 1985a, A&A, 146, 59
———. 1985b, A&A, 147, 39
———. 1985c, A&A, 147, 47
Chiosi, C., Bertelli, G., & Bressan, A. 1992, ARA&A, 30, 235
Christian, C. A., Adams, M., Barnes, J. V., Hutcher, H., Hayes, D. S., Mould, J. R., & Siegel, M. 1985, PASP, 97, 963
Clariá, J. J., & Rosenzweig, P. 1978, AJ, 83, 278
Clemens, D. P. 1985, ApJ, 295, 422
Crawford, D. 1975, PASP, 87, 481
Crawford, D. L., & Mandwewala, N. 1976, PASP, 88, 917
Crinklaw, G., & Talbert, F. D. 1988, PASP, 100, 693
de Jager, C., Nieuwenhuijzen, H., & van der Hucht, K. A. 1988, A&AS, 72, 259
Feast, M. W., & Walker, A. R. 1987, ARA&A, 25, 345
Fernie, J. D., & Hube, J. O. 1968, AJ, 73, 492
Fich, M., & Blitz, L. 1984, ApJ, 279, 125
Forbes, D. 1981, PASP, 93, 441
Frolov, V. N. 1974, Astron. Tsirk., 848, 1
Golay, M. 1974, Introduction to Astronomical Photometry (Dordrecht: Reidel), 91
Grubissich, C. 1975, A&AS, 21, 99
Hardorp, J. 1960, Astron. Abh. Hamburg, 5, 215
Harris, W. E., FitzGerald, M. P., & Reed, B. C. 1981, PASP, 93, 507
Hoag, A. 1966, Vistas Astron., 8, 139
Hoag, A., Johnson, H. L., Iriarte, B., Mitchell, R. L., Hallam, K. L., & Sharpless, S. 1961, Publ. US Naval Obs., 17, 349
Huebner, W. F., Merts, A. L., Magee, N. H., & Argo, M. F. 1977, Astrophys. Opacity Library, UC-34b
Huestamendia, G., del Rio, G., & Mermilliod, J.-C. 1991, A&AS, 87, 153
Janes, K., & Heasley, J. 1993, PASP, 105, 527
Janes, K. A., & Phelps, R. L. 1994, in preparation
Janes, K. A., Tilley, C., & Lyngå, G. 1988, AJ, 95, 771
Jasevicius, V. 1964, Astron. Obs. Bull. Vilnius, 13, 1
Johnson, H. L. 1965, ApJ, 141, 923
Joner, M. D., & Taylor, B. J. 1990, PASP, 102, 1004
Jones, D., & Hoag, A. 1968, PASP, 80, 531
Joshi, U. C., & Sagar, R. 1977, Ap&SS, 48, 225
———. 1983, MNRAS, 202, 961
Keenan, P. C., & Pitts, R. E. 1985, PASP, 97, 297
Kimeswenger, S., & Weinberger, R. 1989, A&A, 209, 51
Kippenahn, R., & Smith, L. 1969, A&A, 1, 142
Landolt, A. 1973, AJ, 78, 959
———. 1983, AJ, 88, 439
Leisawitz, D. 1988, Catalog of Open Clusters and Associated Interstellar Matter (NASA RP-1202)
Leisawitz, D., Bash, F., & Thaddeus, P. 1989, ApJS, 70, 731
Leisawitz, D., & de Geus, E. J. 1991, ApJS, 75, 835
Liu, T., Janes, K. A., & Bania, T. M. 1989, AJ, 98, 626
Liu, T., Janes, K. A., Bania, T. M., & Phelps, R. L. 1988, AJ, 95, 1122
Lyngå, G. 1987, Catalog of Open Cluster Data (Observatoire de Strasbourg, Centre de Données Stellaires)
Maeder, A. 1990, A&A, 84, 139
Maeder, A., & Meynet, G. 1988, A&AS, 76, 411
———. 1989, A&A, 210, 155
———. 1991, A&AS, 89, 451
Maeder, A., & Peytremann, E. 1970, A&A, 7, 120
McCuskey, S. W., & Houk, N. 1964, AJ, 69, 412
Mermilliod, J. C., Mayor, M., & Burki, G. 1987, A&AS, 70, 389
Mihalas, D., & Binney, J. 1981, Galactic Astronomy (2d ed.; San Francisco: Freeman)
Moffat, A. F. J. 1972, A&AS, 7, 355
Montgomery, K., Marschall, L., & Janes, K. A. 1993, AJ, 106, 181
Oja, T. 1966, Ark. Astron., 4, 15
Opal, C. B., Krist, J. E., Barnes, T. G., III, & Moffett, T. J. 1988, AJ, 96, 1677
Osman, A., Khalil, A., Aiad, A., & Marie, M. 1984, in IAU Symp. 105, Observational Tests of the Stellar Evolution Theory, ed. A. Maeder & A. Renzini (Dordrecht: Reidel), 119

Pedreros, M. H., Madore, B. F., & Freeman, W. L. 1984, ApJ, 286, 563
Pesch, P. 1959, ApJ, 130, 764
———. 1960, ApJ, 132, 696
Phelps, R. L. 1992, Ph.D. thesis, Boston Univ.
Phelps, R. L., & Janes, K. 1991a, Mem. Soc. Astron. Italiana, 62, 921
———. 1991b, in Precision Photometry: Astrophysics of the Galaxy, ed. A. G. D. Philip (Schenectady: Davis), 331
Pilachowski, C., Landolt, A., Masey, P., & Montani, J. 1991, NOAO Newsletter, 28, 27
Romeo, G., Bonifazi, A., Fusi Pecci, F., & Tosi, M. 1989, MNRAS, 240, 459
Sagar, R., & Yu, Q. Z. 1989, MNRAS, 240, 551
———. 1990, ApJ, 353, 174
Samson, W. B. 1975, Ap&SS, 34, 363
Sandage, A. R. 1958, ApJ, 128, 150
Sanduleak, N. 1990, AJ, 100, 1239
Schild, R. E. 1983, PASP, 95, 1021
Schmidt, E. G. 1980, AJ, 85, 695
Schmidt-Kaler, T. 1982, in Landolt-Börnstein, Group VI, Vol. 2b, Stars and Star Clusters (Berlin: Springer-Verlag)
Schoening, B. 1988, The CCD Direct-imaging Camera, No. 1 0.9-Meter Telescope (Tucson: NOAO), 26
Stahler, S. W. 1983, ApJ, 274, 822
Steppe, H. 1974, A&AS, 15, 91
Stetson, P. 1987, PASP, 99, 191
Stone, R. C. 1977, A&A, 54, 803
———. 1980, PASP, 92, 426
Sweet, P. A., & Roy, A. E. 1953, MNRAS, 113, 701
Tapia, M., Costero, R., Eshevarria, J., & Roth, M. 1991, MNRAS, 253, 649
Tapia, M., Roth, M., Costero, R., & Navarro, S. 1984, Rev. Mexicana Astron. Af., 9, 65
Tsvetkov, TS., G. 1989, Ap&SS, 151, 47
Turner, D. G. 1976, AJ, 81, 97
Turner, D. G., Forbes, D., & Pedreros, M. 1992, AJ, 104, 1132
van den Bergh, S., & de Roux, J. 1978, AJ, 83, 1075
Whittet, D. C. B. 1989, in Dust in the Universe, ed. M. E. Bailey & D. A. Williams (Cambridge: Cambridge Univ. Press)